Czech Technical University in Prague
Faculty of Electrical Engineering
Department of Circuit Theory (K13131)

Zolotarev Polynomials Utilization in Spectral Analysis

Dissertation Thesis

Ing. Jan Kubák

Ph.D. prog.: Electrical Engineering and Information Technology (P 2612)
Branch of study: Electrical Engineering Theory (2602V013)
Supervisor: Sovka Pavel, Prof. Ing., CSc
Supervisor specialist: Prof. Dr. Miroslav Vlček

Prague, February 2021

Thesis supervisor:
Sovka Pavel, Prof. Ing., CSc
Department of Circuit Theory
Faculty of Electrical Engineering
Czech Technical University in Prague
Technická 2
160 00 Prague 6
Czech Republic

Thesis supervisor specialist:
Prof. Dr. Miroslav Vlček
Department of Applied Mathematics
Faculty of Transportation Sciences
Czech Technical University in Prague
Konviktská 20
110 00 Prague 1
Czech Republic

Abstract

This thesis is focused on selected problems of symmetrical Zolotarev polynomials and their use in spectral analysis. Basic properties of symmetrical Zolotarev polynomials including orthogonality are described. Also, the exploration of numerical properties of algorithms generating even Zolotarev polynomials is performed. As regards to the application of Zolotarev polynomials to spectral analysis the Approximated Discrete Zolotarev Transform is implemented so that it enables computing of zologram in real–time. Moreover, the Approximated Discrete Zolotarev Transform is modified to perform better in the analysis of damped exponential signals. And finally, a novel Discrete Zolotarev Transform implemented fully in the time domain is suggested. This transform also shows that some features observed using the Approximated Discrete Zolotarev Transform are a consequence of using Zolotarev polynomials.

Keywords: Approximated Discrete Zolotarev Transform, Discrete Zolotarev Transform, Chebyshev polynomials, Zolotarev polynomials, Damped Exponential Signals.

Anotace

Tato práce je zaměřena na vybrané problémy Zolotarevových polynomů a jejich využití ke spektrální analýze. Pokud jde o Zolotarevovy polynomy, jsou popsány základní vlastnosti symetrických Zolotarevových polynomů včetně ortogonality. Rovněž se provádí prozkoumání numerických vlastností algoritmů generujících dokonce Zolotarevovy polynomy. Pokud jde o aplikaci Zolotarevových polynomů na spektrální analýzu, je implementována aproximovaná diskrétní Zolotarevova transformace, která umožňuje výpočet spektrogramu (zologramu) v reálném čase. Aproximovaná diskrétní zolotarevská transformace je navíc upravena tak, aby lépe fungovala při analýze tlumených exponenciálních signálů. A nakonec je navržena nová diskrétní Zolotarevova transformace implementovaná plně v časové oblasti. Tato transformace také ukazuje, že některé rysy pozorované u aproximované diskrétní Zolotarevovy transformace jsou důsledkem použití Zolotarevových polynomů.

Seznam klíčových slov: Aproximovaná Diskrétní Zolotarevova Transformace, Diskrétní Zolotarevova Transformace, Chebyševovi polynomy, Zolotarevovi polynomy, Tlumené Exponenciální Signály.

Acknowledgements

My gratitude belongs to supervisors prof. Ing. Pavel Sovka, CSc. and prof. RNDr. Miroslav Vlček, DrSc. for their overall extensive support for my work and many valuable comments that have contributed greatly to the results achieved. Thank you both very much indeed.

List of Tables

List of Figures

List of Acronyms

ADZCT Approximated discrete Zolotarev cosine transform. 69

ADZT Approximated discrete Zolotarev transform. 1, 13, 16, 69, 72

ADZTFB1 Approximated discrete Zolotarev transform with fixed bandwidth to 1. 35

DFT Discrete Fourier transform. 6, 72

DR dynamic range. 55, 72

DZT Discrete Zolotarev transform. 1, 72

FFT Fast Fourier transform. 5, 16

FT Fourier transform. 1

HHT Hilbert-Huang transform. 8

STADZT Short Time Approximated discrete Zolotarev transform. 13, 16

STADZTFB1 Short Time Approximated discrete Zolotarev transform with fixed bandwidth to 1. 35

STDFT Short Time Discrete Fourier transform. 6, 13

WT Wavelet transform. 6

WVD Wigner-Ville distribution. 6, 7

ZP Zolotarev polynomial. 1, 9, 48, 51, 54, 55, 57, 66, 73

ZP1S Zolotarev polynomial of the first kind symmetrical. vii, xi, 11, 12, 47, 51–66

ZT Zolotarev transform. 1

Contents

Chapter 1

Introduction

Signal processing is part of our everyday lives today. Many signals are a product of a differential system of which the natural world is composed. Character of the differential system is best captured by spectral characteristics of the produced signal; therefore, spectral analysis plays an important role as a tool to understand and facilitate the natural world. Straightforward spectral analysis methods are based on Fourier transform (FT). The FT is well defined for stationary processes. Many differential systems vary their parameters in time; they are called non-stationary systems. Quality of spectral analysis based on FT of non-stationary system signals suffers.

One of the possible methods indented for non-stationary signal analysis is Discrete Zolotarev transform (DZT); however, its spectral coefficient evaluation remains a mystery. The closest possible way to evaluate DZT spectral coefficients is the Approximated discrete Zolotarev transform (ADZT). ADZT operates in spectral domain, and its basis is composed of a rather simplified, approximated, Zolotarev polynomial (ZP) spectrum. The direct evaluation using Zolotarev polynomials can clarify some of the ADZT properties, of which some are suspected to be a consequence of an Zolotarev polynomial's inherent property and other artifacts of the algorithm itself. We believe, it is worth a further effort to explore the method of direct evaluation of the DZT using ZPs which is the main motivation behind this work.

Chapter 2

State of the Art

Spectral analysis is a field of signal processing, which mainly deals with transformation of signals between time and frequency domain. One of the main goals is to detect, observe and possibly extract signal information that cannot be analyzed in time domain. Many methods have been designed for this purpose in the last 80 year and are now commonly used in practice. The most widespread are Discrete Fourier Transform (DFT) and its Short-Term variant (STDFT), Wavelet Transform (WT) and its Discrete form (DWT), Hilbert-Huang Transform (HHT), Wigner-Ville Distribution (WVD), Principal Component Analysis (PCA) and last but not least Approximated Discrete Zolotarev transform (ADZT) and its short-term variant (STADZT). This chapter aims to map mainly spectral methods which are based on the DFT. The reason for this limitation is that the Zolotarev polynomials, forming the basis of Zolotarev transformations, are generalized Chebyshev polynomials. Analogically, Zolotarev basis in a generalization of Fourier basis and degrades to the Fourier one under some conditions. Thus it is reasonable to compare the Zolotarev transformations mainly to the Fourier ones. The other methods are only briefly described. More detailed description can be found in stated relevant literature.

2.1 Spectral Analysis Methods

2.1.1 Discrete Fourier Transform

One of the most widespread transforms used for spectral analysis is Discrete Fourier Transform (DFT). The DFT expresses the relationship between time and frequency domain according to the following relation [1]

$$S(\ell) = \frac{1}{N} \sum_{n=1}^{N} s(n) \exp\left(\frac{-j2\pi n\ell}{N}\right), \qquad \ell = 1, \ldots, N-1, \tag{2.1}$$

where $s(n)$ is the analyzed discrete signal of a given length N, n denotes the index of the signal sample and ℓ is the index of the spectral component. The complex exponential forms the basis of DFT. The resulting DFT spectrum is composed of spectral coefficients $S(\ell)$, which represent frequency bandwidths containing the analyzed signal energy. More details can be found in [2]. Equation (2.1) can be rewrite into a matrix notation as

$$\mathbf{S} = \mathbf{W}\,\mathbf{s}, \tag{2.2}$$

where $\mathbf{S}$ is a column vector containing the individual spectral components, $\mathbf{s}$ is the input signal vector and the matrix $\mathbf{W}$ contains the basis functions of DFT.

$$\mathbf{W} = \begin{bmatrix} \omega_N^{0\cdot 0} & \omega_N^{0\cdot 1} & \cdots & \omega_N^{0\cdot(N-1)} \\ \omega_N^{1\cdot 0} & \omega_N^{1\cdot 1} & \cdots & \omega_N^{0\cdot(N-1)} \\ \vdots & \vdots & \ddots & \vdots \\ \omega_N^{(N-1)\cdot 0} & \omega_N^{(N-1)\cdot 1} & \cdots & \omega_N^{(N-1)\cdot(N-1)} \end{bmatrix}, \tag{2.3}$$

where $\omega_N = \exp(\frac{-i2\pi}{N})$.

The DFT is a very good tool for stationary signal analysis. However, difficulties occur in the case of non-stationary signals, where the analyzed signal spectral properties change over time. DFT is not able to localize changes in signal spectrum in time. This fact motivated extensive research which gave birth to a number of methods targeting non-stationary signal analysis.

2.1.2 Short Time Discrete Fourier Transform

The Short-Time DFT (STDFT) is one of the most widely used spectral methods for the analysis of a signal with a changing characteristic over time, for example, speech, music, or various biological and diagnostic signals. The STDFT principle lays in segmentation of analyzed signal, signal windowing [1], and applying the DFT to particular segments. This process in described by

$$S(m,\ell) = \frac{1}{N}\sum_{n=1}^{N} s(n)\,w(n-m)\exp\left(\frac{-j2\pi n\ell}{N}\right), \qquad \ell, m = 1,\ldots,N-1, \tag{2.4}$$

where $w(n)$ is the segmentation window, which selects the given signal segment with a defined length N. The segmentation window selects parts of analyzed signal and it is gradually shifted in step m samples. The DFT is then applied to each of the signal segments. The windowing process adds time localization context. Each DFT result of a particular segment is related to a particular segment shift in time. The result of the

STDFT is very clearly expressed by a spectrogram which displays the DFT spectral coefficients in time-frequency lattice.

The frequency and time resolution spectrogram lattice is given by the segmentation window parameters, the window length and step. The length defines the frequency resolution as $\Delta f = \frac{f_S}{N}$, where f_S is the analyzed signal sampling frequency, and the step directly defines the time resolution. The time and frequency resolution is coupled and mutually constrained, which is an intrinsic segmentation principle property. This property is closely related to Heisenberg's uncertainty principle according to the relation [3] as

$$B\,T_0 = constant, \tag{2.5}$$

where B is the equivalent bandwidth and T_0 corresponds to the equivalent length of the record. Another important aspect is the impact of spectral leakage. Spectral leakage becomes gradually significant with shortening of window length. The common approach is to select Hamming window as a weighting window and assume that the frequency accuracy is half of the frequency resolution given by the lattice. The leakage is reduced to -41 dB, which is the relative peak side-lobe amplitude of the Hamming window [1].

The uncertainty principle constrains the frequency and time resolution: it is not possible to achieve better frequency resolution without reduction of the time resolution and vice versa. Thus one has to find a compromise between time and frequency resolution for each particular application. A common approach is to the two types of spectrograms which represent extreme limits of the STDFT resolution. The first type is narrowband spectrogram where STDFT uses long segmentation window. The long window leads to fine frequency grid and spectral leakage is also minimized; however, the time resolution becomes very poor. The second type is broadband a spectrogram which is created using a very short segmentation window. The short window length leads to high time resolution but the frequency resolution is poor.

In general, it can be said that DFT and its short-term variant STDFT belong to the very widespread spectral methods for its simple definition, interpretation, reversibility and linearity. Another reason advantage is the possibility of a very efficient implementation using the Fast Fourier Transform (FFT).

There are modifications to STDFT such as Fractional Fourier transform (FRFT), which generalizes classical FT [4, 5, 6].

2.1.3 STDFT with adaptive time-frequency resolution

The described trade-off between time and frequency resolution of the STDFT is different for each analyzed signal. Thus the parameter of window length N in (2.4) can be taken

as parameter to optimize. The adaptive time-frequency resolution methods optimize the window length in order to minimize the spectrum power fitting best each segment of analyzed signal. These methods can be found in [7, 8, 9].

Minimum spectral leakage methods

A method used for the analysis of audio signals reaches the best time-frequency resolution out of the list. This method selects the optimal window length of the segmentation window based on optimization criteria of spectral leakage energy minimization.

The method calculates DFT for segments of particular shift for all possible lengths. The minimal window length is selected based on the optimization criterion employing the principle of the minimum description length principle [10]. The algorithm [7] can be divided into several steps:

1. Calculation of spectrograms S_r with different window length $N_r = 2^c$, which is centered around the current sample, and increases symmetrically to the sides with increasing length. The parameter c is a natural number of interval $\langle c_{min}, c_{max} \rangle$. Thus we obtain a set of spectra with different time-frequency resolution, of which the one that minimizes the leakage energy is selected.

2. Calculation of spectral leakage energy is realized according to relation [7]

$$L_r(d) = \frac{\sum_{i=1}^{N_r} N_r i \, |a_{i,r}|^2}{\sqrt{\sum_{i=1}^{N_r} N_r \, |a_{i,r}|^2} + \epsilon}, \tag{2.6}$$

   where d is the index of the segment of the r-th spectrogram with the corresponding window length N_r and $a_{i,r}$ denotes the i-th spectral coefficient of the d-th segment. The coefficients $a_{i,r}$ must be arranged descending in size. Expression (2.6) represents the first moment of distribution of variables $|a_{i,r}|^2$ (numerator) normalized by the total signal energy (denominator). The $\epsilon > 0$ in the denominator treats any division by zero.

3. The optimal length of the STDFT window is equal to the length of the spectrogram window with the least energy spectral leakage L_r.

4. The spectrogram with optimal time-frequency resolution is composed of particular spectra of different optimal lengths $S_r(k)$.

The advantage of this adaptive method is the clear principle of selecting the window length, the Fast Fourier transform (FFT) usage and possibility to reverse the signal from the frequency domain back to the time domain (the optimal window length for each signal segment must by stored).

Instantaneous frequency estimation method

The following adaptive method is of Fourier type and selects the STDFT segmentation window length by estimating the instantaneous frequency pertaining to a segment. The optimization criterion is confidence interval of instantaneous frequency estimation [9]. The algorithm can be described as follows. First the spectrograms of analyzed signal with different window lengths are calculated and then the instantaneous frequency $\omega_d(lT, N_s)$ is estimated according as

$$\omega_d(lT, N_s) = \frac{\pi}{N_s T} \operatorname{argmax}(S_d(l)), \tag{2.7}$$

where $S_d(l)$ is the power spectrum of the respective segment d, l is the spectral index, T is the sampling period and N_s is the number of Discrete Fourier transform (DFT) points. The resulting spectrogram is composed of individual spectra with different time-frequency resolution. which is achieved by determining the optimal length windows according to the following conditions

$$|\omega_{h_{s-1}}(lT) - \omega_{h_s}(lT)| < 2\kappa \left(\sigma(h_{s-1}) + \sigma(h_s)\right), \tag{2.8}$$

where h_s denotes the length of the window used to calculate the spectrum and σ is standard deviation of the employed window. This condition sequentially tests all estimated instantaneous frequencies for all window lengths until the condition is still valid. If this condition ceases to be valid, the window length h_{s-1} is marked as optimal. A more detailed theoretical description of this adaptive spectral method can be found in [9] and in [11]. The idea of using instantaneous frequency estimation to adaptively adjust the frequency resolution can also be applied to the Wigner-Ville distribution, as shown in [12].

2.1.4 Wigner-Ville distribution

In addition to spectral methods using the Fourier transform, there are a number of methods which are very often used in practice for the analysis of non-stationary signals and achieve very satisfactory results. These methods include the Wigner-Ville distribution (Wigner-Ville distribution (WVD)), which uses the autocorrelation function of the input signal. The WVD result is determined by the distribution energy of the analyzed signal in the time-frequency domain and offers excellent time resolution [13]. This feature is achieved by not using any weighing window which aggravates frequency resolution and at the same time limits the time resolution as in Short Time Discrete Fourier transform (STDFT) or Wavelet transform (WT). The WVD calculation can be performed according

to the following relation [14].

$$W(t,f) = \int_{-\infty}^{\infty} z\left(t+\frac{\tau}{2}\right) z^*\left(t-\frac{\tau}{2}\right) \exp(-j2\pi f\tau) d\tau, \tag{2.9}$$

where $z(t)$ is the analytical signal and $z^*(t)$ is its complex conjugate. Analytical signal from $z(t)$ is created from the signal $s(t)$ by means of the Hilbert transform (HT) as

$$z(t) = \frac{1}{\pi} P \int_{-\infty}^{\infty} \frac{s(\tau)}{t-\tau} d\tau, \tag{2.10}$$

where P denotes the Cauchy principal value. Frequency spectrum analytical signal is almost identical to the original signal for frequencies that are positive and non-zero, otherwise the frequency spectrum is zero. This feature minimizes interference (cross-terms), which arise between each pair of harmonic components of the analyzed signal [15]. When using an analytical signal, the number of interferences decreases from the original the number $N(2N-1)$ to $N(N-1)$, where N denotes the number of spectral components of the signal. The interference may result in inaccurate interpretation of WVD results. The interference reduction can be achieved by one of the modifications, which seeks to suppress interference making the result energy distribution in time-frequency domain more legible.

One of the most frequently used modifications is called Smoothed pseudo Wigner-Ville distribution (PSWVD), which reduces interference using the time smoothing window $h(m)$ and the frequency smoothing window $g(m)$. In other words, the window $h(m)$ limits the length of the analyzed signal and the function $g(m)$ implements a low-pass filter [16]. The SPWVD can be defined as

$$W(t,f) = \int_{-\infty}^{\infty} h(\tau) \int_{-\infty}^{\infty} g(s-t) z\left(t+\frac{\tau}{2}\right) z^*\left(t-\frac{\tau}{2}\right) ds \exp(-j2\pi f\tau) d\tau. \tag{2.11}$$

Another and very effective way to reduce interference between the spectral components of the analyzed signal is to use a "special distribution core", which can be imagined as a 2-D low-pass filter. Among the widely used "distribution kernels" are the Choi-Williams functions [13, 17]. All the mentioned modifications leading to the reduction of the interference of the analyzed signal have the same disadvantage in lower time-frequency resolution compared to the WVD. Another disadvantage compared to methods based on the Fourier transform is the inability to reverse transform the analyzed signal. The WVD, on the other hand offers excellent time resolution and does not suffer from spectral leakage. In parallel to the STDFT a method reaching optimal window length can be used [18, 12].

2.1.5 Wavelet Transform

The wavelet transform (WT) is one of the transformations that are very often used for spectral analysis of nonstationary signals. The principle of this transformation uses the degree of correlation input signals with a predefined mother wave. Time-frequency analysis is realized by shifting the mother wavelet in time and changing its effective width (scale) - so-called scaling. The base of the WT is formed by a scaled mother wave. WT is further divided into two variants for continuous wavelet transform (CWT) and discrete wavelet transform (DWT). In general, you can write a relation for CWT as

$$W(a,b) = w(a) \int_{-\infty}^{\infty} s(t)\psi^* \left(\frac{t-b}{a} \right) dt, \tag{2.12}$$

where $\phi\left(\frac{t-b}{a}\right)$ is a shifted and scaled mother wavelet which must satisfy the following two conditions: (i) the energy of the ripple must be finite and (ii) its mean value must be equal to zero. The parameter a scales (dilation) the wavelet and the parameter b shifts the wavelet in time. Weighing the function $w(a)$ guarantees that the energy of the ripple is always the same on all scales [19].

The CWT result is represented by a so - called scalogram (scalgram, level diagram), which shows the mutual energy between the base function CWT and the analyzed signal in time-scale space. The relationship between time-frequency and time-scale space must be determined for each mother wave separately and this relationship is expressed as $a = \frac{f_c}{f}$, where f_c is the unique frequency of each mother wave. The resolution of the resulting scalogram is also limited by the uncertainty principle (2.5), as is the case with the spectrogram representing the STDFT result. In contrast to the spectrogram, the frequency resolution in the time and scale domain depends on the frequency characteristics of used mother waveform and given scale. The CWT frequency resolution decreases with increasing scale, while the time resolution increases.

There is a number of wavelet functions to choose from, such as the Mexican hat, the Morlet or Meyer function. Thus it is always necessary to chose best suitable function for particular analyzed signal.

One of the most efficient spectral methods that was developed during the 1990s years for the analysis of nonlinear and non-stationary signals belongs to the Hilbert-Huang transformation (Hilbert-Huang transform (HHT)). This transformation is based on the modal decomposition of the signal (Empirical Mode Decomposition - EMD), which decomposes analyzed signals into a set of signals formed by own modal functions (Instristic Mode Functions - IMF). The modal decomposition of an analysed signal is an iterative process with a number of conditions that define the IMF components themselves and control their calculation. A more detailed description of the HHT calculation can be

found in [20]. The result of decomposition signal is a set of IMF components by which the analyzed signal can be expressed as

$$s(t) = \sum_{i=1}^{n} c_i + r_n, \tag{2.13}$$

where c_i is the i-th IMF component and r_n is the decomposition residuum after the n-th iteration. One whole signal is decomposed to the IMFs, the HT (2.10) is applied to each component. The result is analyzed signal description by the instantaneous frequencies $\omega = \frac{d\theta(t)}{dt}$, where θ is the phase of the analytical signal. The analyzed signal $s(t)$ can be expressed as [21]

$$X(t) = \sum_{i=1}^{\infty} a_i(t) \exp\left(j \int \omega_i(t) dt\right), \tag{2.14}$$

where a_i and ω_i represent the instantaneous envelope and frequency of the analytic signal composed of the i-th IMF component [20]. The envelope and frequency expressed as a function of time form the Hilbert spectrum $H(\omega, t)$ of the analyzed signal. Further details can be found in [22, 23].

2.1.6 Other Methods

There are a number of robust methods using parametric modeling, least squares methods, decomposition of a correlation matrix into a signal and noise subspace, methods performing under L1-norm, L2-norm or infinity norm. Higher order statistics is used as well. Most of the mentioned methods can be found, for example, in [24, 25, 26, 27].

2.2 Zolotarev Polynomials

ZPs are an important generalization of Chebyshev polynomials. This class of polynomials is equiripple in disjoint interval, and non-equirriple in the complement of the disjoint interval. Their maximum of absolute value is situated within the non-equirriple interval. See an example of Chebyshev and Zolotarev polynomials of the first kind in Figure 2.1a and Figure 2.1b, respectively. Both properties are well suited to approximate FIR frequency response; thus, the polynomials were employed in analytical design of FIR filters by prof. Miroslav Vlček and prof. Pavel Zahradník see [28, 29, 30] and also by others [31]. Aditionally, ZPs were also recently employed for design of circular antenna array [32]. Mentioned features of the ZP inspired an application in spectral signal analysis, which led to development of an approximated discrete Zolotarev transform, described in the next section. However, practical utilization of ZP was not possible till recently. The reason was the absence of a method able to generate ZP of high enough degree, as was emphasized

in [33].

Symmetrical Zolotarev polynomials are employed in spectral analysis; their generation is more numerically stable compared to asymmetrical ones. Maximum of absolute value of a symmetrical polynomial is located at the center, or near it, of the function definition interval. Short time variant of the transform, where windowing principle is employed, uses very short analyzing window step. Short window step ensures the central lobe alignment with all analyzed signal subsegments.

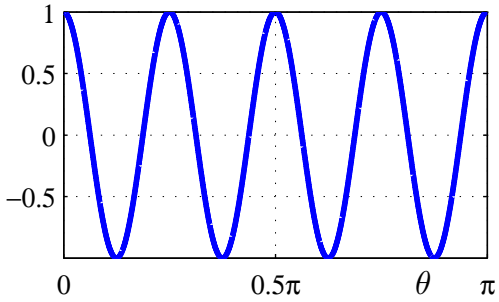

(a) An example of Chebyshev polynomial of the first kind and degree four with substitution $x = cos\,\theta$ relating to cosine function.

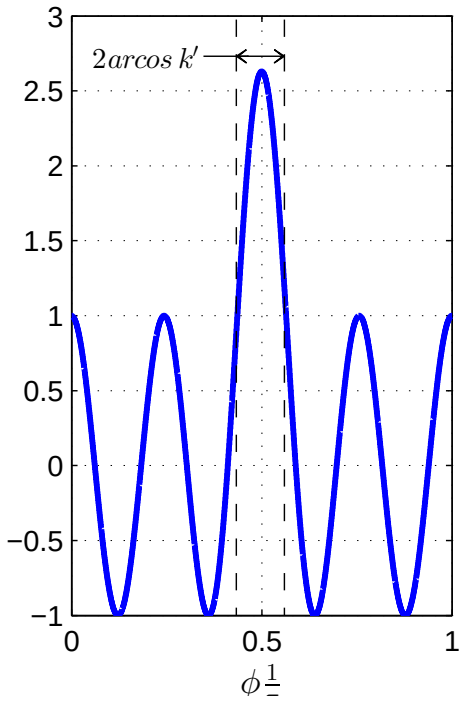

(b) An example of symmetrical Zolotarev polynomial of the first kind and degree four with substitution $x = cos\,\theta$. Parameter k' relates to the width of the interval with non-equiripple property.

Figure 2.1: An example of Chebyshev and Zolotarev polynomials, both of the first kind and forth degree.

2.2.1 A Filter Design Example

Zolotarev polynomials are used for FIR design. Filter's frequency response is approximated by the Zolotarev polynomial, and its coefficients are derived. An example of possible approach to FIR filter design follows. This example was created based on the article [29]. In general, non-symmetrical polynomials are used in the FIR filter design; however, this example uses a symmetrical polynomial for simplicity. Symmetrical Zolotarev poly-

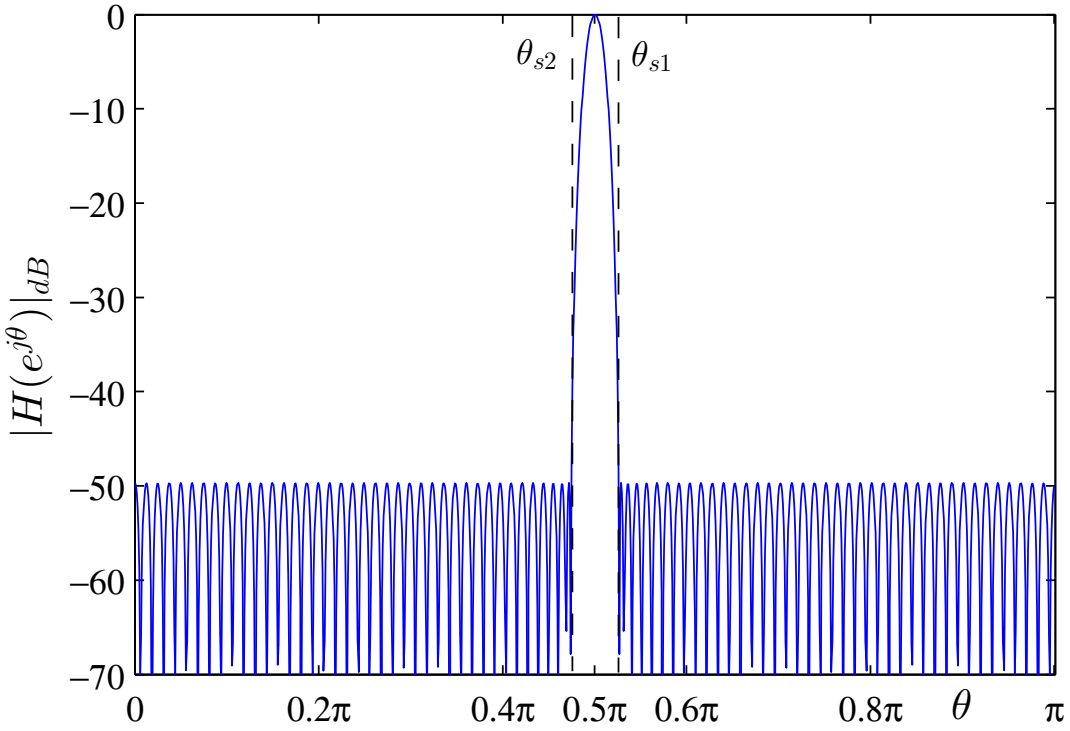

Figure 2.2: FIR filter frequency response based on the symmetrical Zolotarev polynomial of the first kind $Z_M(w, k')$ for $M = 80$ and $k' = 0.08$ yielding left and right stopband edge $\theta_{S1} = 0.4745\pi$ and $\theta_{S2} = 0.5255\pi$, respectively, and stopband ripple $\delta = -49.7dB$.

nomials of the first kind (ZP1S) can form frequency response of a pass band FIR filter with pass-band around central frequency. A FIR filter transfer function can be written in general form [1] as

$$H(z) = \sum_{v=0}^{N-1} h(v) z^{-v}, \tag{2.15}$$

where $h(v)$ is the impulse response, $N = 2M + 1$ is the filter length and M is the filter order. The filter transfer function employing ZP1S polynomial is given [28] as

$$\begin{aligned} H(z) &= z^{-\frac{M}{2}} \frac{1}{A} \left[\sum_{\ell=0}^{M-1} a(\ell) T_\ell(w) \right] = \\ &= z^{-\frac{M}{2}} \frac{1}{A} \left[Z_M(w, k') \right], \end{aligned} \tag{2.16}$$

where A is the scaling coefficient. By comparing (2.15) with (2.16) the impulse response can assembled from a coefficients as

$$\begin{aligned} h(2v) &= \frac{1}{2A}a(M-v), \\ h(2M+2v) &= \frac{1}{2A}a(v), \\ h(2v+1) &= 0, \\ v &= 0,\ldots,M. \end{aligned} \tag{2.17}$$

Such an impulse response is even symmetrical and forms a linear phase type I. FIR filter. The coefficients $a(v)$ are direct output of the backward recursion algorithm [28]. The variable w in (2.16) is related to the complex variable z by transformation $w = \frac{1}{2}(z+z^{-1})$. The transformation degrades to $w = cos(\theta)$ in case of frequency response $H(z = e^{j\theta})$: $w = \frac{1}{2}(z+z^{-1}) = \frac{1}{2}(e^{j\theta}+e^{-j\theta}) = cos(\theta)$. Hence

$$H(e^{j\theta}) = z^{-\frac{M}{2}}\frac{1}{A}\left[Z_M(cos(\theta),k')\right]. \tag{2.18}$$

The k' is a function of θ_S which is a symmetrical stopband edge. Having in mind the transformation of w in case of frequency response $w = cos(\theta)$ the k' is simply given as

$$k' = cos(\theta_{S1}), \tag{2.19}$$

where θ_{S1} is left stopband edge. The stopband ripple is gives as

$$\delta = 20\, log_{10}\frac{1}{A}. \tag{2.20}$$

The scaling coefficient A is virtually maximum value of ZP1S. The maximal value is localized in the center of the polynomial and can be derived from (6.16) by substituting $w = 0$ as

$$A = Z_M(w=0,k')_{max} = \sum_{\ell=0}^{M-1} a(\ell)T_\ell(0). \tag{2.21}$$

The derivation of the degree equation $p = f(\delta,\theta_S)$ is out of scope of this paper. The example of symmetrical pass band FIR filter using ZP1S is in Fig. 2.2. Also a high pass filter can be formed by discarding zero samples of filter impulse response. A low pass filter can be easily converted from a high pass one. Various filter types based on Zolotarev polynomials are described in [30, 29, 34, 28] and others.

2.2.2 Approximated Discrete Zolotarev Transform

The Approximated Discrete Zolotarev Transform (ADZT) provides high, constant, frequency resolution, given by constant window length and its time resolution is improved by the basis time selectivity properties. The ADZT was proposed by Dr. Špetík in his dissertation thesis [35] and it is best described in Turoň's dissertation [36]. Short Time ADZT (STADZT) [37] is defined in analogy to the STDFT as

$$\begin{aligned} S_Z(\ell, n) &= \sum_{m=-\infty}^{\infty} s(m)w(m-n)\,\mathrm{zexp}(\ell, i2\pi n) \\ &= \mathrm{ADZT}\left\{s(m)w(m-n)\right\}(\ell), \end{aligned} \tag{2.22}$$

where the window w has a final length of N_0 and n is the window offset in samples. The two dimensional spectrum $S_Z(\ell, n)$ can be displayed graphically as a so-called zologram, in analogy to spectrogram. The Short Time Approximated discrete Zolotarev transform (STADZT) spectrum reflects abrupt transitions in signals. Method's key properties are summarized in the following list.

- Significantly better time resolution compared to DFT for selected frequency resolution.
- Significant spectral leakage reduction.
- Side effect of spectral leakage reduction is complete removal of damped exponential signals from spectra for some signal parameters, which prevents detection of such signals.
- Transform's behavior is strongly dependent on analyzed signal shift within analyzed window; the transform is dependent on analyzed signal phase.
- Sensitivity to analyzed signal envelope energy: for example, in a mixture of two harmonic signals the spectrum components localized around zeros of beat frequency envelope are removed.
- Ability to capture analyzed signal non-stationary features is increased with larger transform length.
- Run time of the transform is relatively large, which prevents practical usage.

Rigorous comparison with the other methods can be found in [36] and similarly in [37, 38, 39, 36].

Chapter 3

Goals of the Thesis

Goal 1 ADZT algorithm runtime optimization

- Evaluate computational demands of the algorithm.
- Design a more efficient algorithm in terms of computational demands.
- Implement the algorithm efficiently to be able to acquire outputs in reduced time, in real-time if possible.

Goal 2 Transient signals analysis with ADZT

- Based on analysis of ADZT behavior in the analysis of damped exponential signals, adapt the ADZT to perform better in the detection of transient signals, damped exponential signals in particular. Motivation is a possibility of fault detection in rotating machinery.

Goal 3 Symmetrical Zolotarev polynomials

- Summarize current finding regarding symmetrical Zolotarev polynomials including orthogonality properties.
- Describe yet unresolved desired properties of the polynomials with respect to spectral analysis.
- Explore numerical properties of even Zolotarev polynomials generation algorithm. Assess precision of generated polynomials as a waveform in the time domain and coefficients in the spectral domain.

Goal 4 Symmetrical Zolotarev polynomials in spectral analysis

- Explore evaluation of discrete Zolotarev transform coefficients in the time domain.

- Propose a novel spectral analysis method employing symmetrical Zolotarev polynomials in the time domain; in contrast with the ADZT which uses approximated polynomials and is implemented in the frequency domain.
- Assess the behavior of the proposed spectral analysis method based on symmetrical Zolotarev polynomials by comparing with the ADZT. Describe differences in results given by both methods.

Chapter 4

ADZT Computational Demands and Optimization

The ADZT algorithm leads to relatively high computational load compared to other spectral analysis methods, e.g. FFT algorithm. The STADZT improvement becomes apparent for high segment lengths; 512 samples and higher. In general, longer the segment the better [38]. It is recommended to use segment overlap at least 75 % segment length, 90 % ideally, to prevent information loss [38]. Large segment length, large segment overlap, and structure of the ADZT algorithm leads to significantly high computation load. Therefore, software implementation runtime of the algorithm is relatively long. Original ADZT implementation in Matlab, available at [40], is able to compute one-shot ADZT spectrum of 2048 length in 6.2 s, measured on a PC equipped with Pentium 4 processor. Taking into account large segment overlap total runtime for STADZT of an analyzed signal is in tens of minutes or even more.

Firstly, Computational demands of the algorithm are analyzed with means of algorithm asymptotic complexity. Secondly, a more computationally software implementation is proposed and verified. Thirdly, an embedded solution is designed and verified.

4.1 ADZT Algorithm Description

This section briefly describes the ADZT algorithm. Purpose of the description is to enable analysis of the algorithm computational demands, to be able to propose more efficient implementation as well as its realization.

The ADZT algorithm was first introduced by Radim Špetík in his dissertation thesis [35] and it is best described in Václav Turoň doctoral thesis [36]. The ADZT algorithm [37, 36] can be divided into three steps, see Fig. 4.1, of which descriptions follow.

Step 1 The first step is DFT spectrum computation using the FFT algorithm of

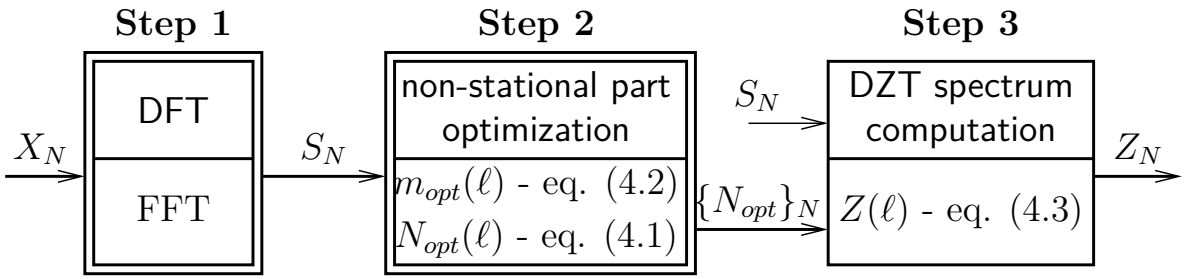

Figure 4.1: The ADZT algorithm diagram; blocks with double line border are implemented in HW and with single line in SW.

length N_{DFT}. Since the algorithm works only with real signal, it is sufficient to work with a one-sided spectrum of length $N = \frac{N_{DFT}}{2}$.

Step 2 In the second step the ADZT basis selectivity refinement takes place. The algorithm works in the spectral domain for each ℓth spectral line, $\ell = \{1, \ldots, N\}$. The DZT spectrum $Z(\ell)$ can be decomposed [41] in the stationary part and non-stationary (N-S) part. The stationary part $S(\ell)$ is ℓth DFT spectral line. The N-S part

$$N(\ell, m) = \sum_{\ell'=1}^{m} (-1)^{\ell'} S(\ell - \ell'), \tag{4.1}$$

is parametrized by bandwidth[1] m of approximated polynomial. The transformation selective feature is comprised in the N-S part. The transformation selectivity refinement is administered by varying the non-stationary part using the bandwidth. Optimal bandwidth is estimated according to

$$m_{opt}(\ell) = \arg\min_{m'} \left\{ \frac{1}{m'} \, N(\ell, m') \, \mathrm{sgn}(S(\ell)) \right\}, \qquad m' = \{1, 2, \ldots, N-1\}, \tag{4.2}$$

where m' is tested bandwidth. The optimal N-S part $N_{opt}(\ell)$ is acquired from (4.1) using estimated optimal bandwidth (4.2).

Step 3 The DZT spectrum is composed from the stationary and the N-S part for each ℓth spectral line, $\ell = \{1, \ldots, N\}$. At first the signs of each part are compared with each other. Based on the result of the comparison one of the following three cases is taken: the first case is to suppress spectral line $Z(\ell) = 0$; the second one is to preserve DFT spectral line $Z(\ell) = S(\ell)$; the third one is to determine a new spectral line value according to

$$Z(\ell) = norm(\ell) \left\{ S(\ell) + k(m_{opt}(\ell)) N(\ell) \right\}, \tag{4.3}$$

[1]The term bandwidth is different from frequency bandwidth.

where

$$norm(\ell) = \frac{1}{\sqrt{1 + m_{opt}(\ell)k^2(m_{opt}(\ell))}}, \tag{4.4}$$

is the normalization coefficient,

$$k(m) = \sqrt{\frac{1-\sigma^2}{m\sigma^2}}, \tag{4.5}$$

is the non-stationarity index (N-S index) and σ is the degree of the N-S part suppression. The parameter σ has a value in interval $\sigma \subset (0, 1)$; it is chosen according to user needs.

The algorithm works separately for the real and imaginary spectrum part; after each part is processed the complex DZT spectrum is recomposed.

4.2 Computational Demands Analysis

At first an estimation of the computational power necessary to execute STADZT transform is performed. The analysis of the ADZT algorithm in Fig. 4.1 asymptotic complexity for each step follows.

Step 1 computation of the N_{DFT}-point DFT spectrum $S(\ell)$. The DFT spectrum is computed using the FFT algorithm. N_{DFT} is constrained to be the power of 2. Thus the asymptotic complexity of this step is $O_1 = O(N_{DFT}\ \log_2 N_{DFT})$.

Step 2 Estimation of the optimal bandwidth $m_{opt}(\ell)$ by minimization (4.2) of the N-S part (4.1) for one-sided DFT spectrum of length N. The asymptotic complexity of this step is $O_2 = O(N^2)$.

Step 3 The DZT spectrum composition according to (4.3); this step has constant time complexity of $O_3 = N$.

Hence the asymptotic complexity of the ADZT algorithm is $O_{ADZT} = O(N^2)$. Step 2 is the most time consuming one. Compare this with FFT algorithm asymptotic complexity of $O_{FFT} = O(N\ \log_2 N)$.

Based on the structure of the algorithm we also did a more precise estimation of necessary system-level computation power in MIPS (million instructions per second). We assume a standard Harvard DSP CPU architecture with three buses (instruction, data bus X, and data bus Y), divider with DIV operation, and Multiply And Accumulate (MAC) unit; such that MAC operation unit is able to load two operands simultaneously. Computational powers needed for the algorithm steps are stated in Tab. 4.1. Based on the above we can say that real-time STADZT of $N_{DFT} = 2\,048$ samples with 80 % overlap needs a CPU with performance at least ≈ 210 MIPS, and performance of ≈ 420 MIPS for 90 % overlap. Approximate processor requirements are as follows. A 32 bit fixed-point

Algorithm step	**Operation**	**Inst. per iteration**	**Time complexity**	**Comp. power (MIPS)**	
				Overlap (OV): 80 %	**OV: 90 %**
1(FFT)	complex MULT	4 [2]	$N_{DFT}/2 \times \log_2(N_{DFT})$	≈ 2	≈ 4
	complex ADD	2	$N_{DFT} \times \log_2(N_{DFT})$	≈ 2	≈ 4
2 (N-S opt)	(4.1), (4.2)	5 [3]	N^2	≈ 206	≈ 413
3 (DZT spec.)	(4.5), (4.4), (4.3)	$19 + 18 + 3$ [4]	N	≈ 2	≈ 3
			Total:	≈ 210	≈ 420

[2] four MAC operations
[3] (4.1): one MAC operation, (4.2): one DIV and two MULT operations, arg min search in one operation
[4] (4.5): three multiplications, one subtraction, one division, and fifteen operations for 32 bit square root using Newton's method; (4.4): three multiplications, one subtraction, one division, and fifteen operations for 32 bit square root using Newton's method; (4.3): one addition and two multiplication operations

Table 4.1: The estimation of computational power in MIPS needed for the STADZT real-time computation with segment length of $N_{DFT} = 2\,048$ samples and sampling frequency of $f_s = 16$ kHz for segment overlaps of 80 % and 90 %.

DSP processor with MAC requires clocking frequency of 300 MHz or 600 MHz, for 80 % or 90 % overlap, respectively. A general purpose processor without a MAC unit requires clocking frequency of 400 MHz or 800 MHz, for 80 % or 90 % overlap, respectively; the lack of a MAC unit raises power requirements by ≈ 30 %.

4.3 Optimized Software Implementation

Original ADZT implementation in Matlab, available at [40], uses 64 bit wide floating-point arithmetic, which implementation is rather inefficient in terms of resources and power consumption. For an efficient implementation fixed-point representation is more suitable. We implemented the algorithm model using $N_b = 32$ bit wide fixed-point variables and arithmetic written in C language; the model proper functionality was verified against the original Matlab implementation. The descriptions of computation methods used in the fixed-point algorithm implementation in each algorithm step in Fig. 4.1 follow.

Step 1 We used Fast Fourier Transform (FFT) decimated in frequency (DIF) as DFT computation algorithm. The FFT uses radix-2 with 32 bit fixed-point arithmetic. As a precaution measure to prevent overflows each stage output is divided by 2, see [42]. The FFT has $N_{stages} = \log_2(N_{DFT}) = 11$ stages in case of maximal signal segment length; the output is 11 times shifted right. The overflow does not necessarily occur in every stage.

We carried out a simulation [5] showing that the average count of overflows N_{OF} is 4 and 7 in the worst case. Thus the 32 bit FFT result has 25 Less Significant Bits (LSB) non-zero ($N_b - N_{stages} + N_{OF} = 32 - 11 + 4 = 25$ bits) in average and 28 LSB non-zero in the worst case ($N_b - N_{stages} + N_{OF} = 32 - 11 + 7 = 28$ bits).

Step 2-1 The N-S part is computed according to (4.1). Equation (4.1) can be rewritten into recurrent form

$$N(\ell, m) = N(\ell, m-1) + (-1)^m \, S(\ell - m), \tag{4.6}$$

which is more suitable for computation. An overflow can occur $\log_2(m)$ times in the worst case where $m = N - 1$. The DFT coefficients have 6 Most Significant Bits (MSB) in zero on average case. The saturation must be applied after each addition. Non saturated overflown result could lead to false minimal N-S part detection in the next step; this would result in a distorted DZT spectral line value. If a result is saturated, it will be the largest one in the tested set of bandwidths. The result will not be, most likely, selected as minimal and its value will be discarded. In a nutshell, saturated N-S part does virtually no harm. Moreover, no overflow had occurred in N-S part computation during the conducted simulation using 32 bit wide variables and segment length of $N_{DFT} = 2\,048$.

Step 2-2 Estimation of optimal bandwidth according to (4.2); the N-S part, computed in previous step, is weighted by weighting coefficient $\frac{1}{m'}$ and $\mathrm{sgn}(S(\ell))$ for each m'. The minimal value is being selected simultaneously. The weighting coefficient $\frac{1}{m'}$ in (4.2) for each m' is precomputed in memory in order to multiply by $\frac{1}{m'}$ rather than divide by m'. The weights $\frac{1}{m'}$ are ≤ 1 for each m'; after division by 2 overflow is not an issue here.

Step 3 The DZT spectrum composition according to (4.3) can be rewritten using (4.4) and (4.5) to

$$Z(\ell) = \sigma S(\ell) + K(m_{opt}(\ell)) \, N(\ell), \tag{4.7}$$

where $K(m) = \sigma \, k(m)$. There are two reasons why the rewritten form is more suitable for fixed-point arithmetic computation. Firstly, by pre-computing coefficient $K(m)$ for each bandwidth the N-S is actually multiplied only once; thus, reducing round-off error. Secondly, the range of $K(\ell)$ is $(1, 0)$, which allows us to avoid normalization; thus there is no signal to quantization noise ratio drop.

Designed fixed-point software implementation of the ADZT algorithm in C language allows to compute one-shot ADZT spectrum in 100 μs, measured on a PC equipped with Pentium 4 processor.

[5] The stimuli of the simulation were composed of a few musical tracks of different genres, several minutes of spoken language, and several segments of Gaussian noise.

4.4 Embedded Implementation

An embedded solution enables application in an embedded system. While keeping in mind the main goals of the embedded system: low area requirement and low power consumption, we approached the system design with co-design methods. The algorithm is implemented on hardware (HW) devices with encapsulated processors; main computational stress is loaded on HW units allowing the processor to be simple, small and low power. Field Programmable Gate Array (FPGA) was chosen as a HW platform: the FPGA is widespread nowadays and can be easily integrated into a large System on Chip (SoC). Furthermore, the FPGA power consumption is low especially with non-volatile devices. The system requirements are to compute real-time STADZT spectrum of following parameters:

- the input signal is mono audio signal with sampling rate of $f_s = 16$ kHz,
- maximal segment length is $N_{DFT} = 2\,048$ samples,
- segment overlap of 80 % at least, 90 %, if possible.

The design of the embedded solution is described in Appendix A, see Chapter 9.

4.4.1 Physical Parameters

Xilinx Spartan 6 FPGA [43] was chosen as a target device, since there were several development boards [44] equipped with it at disposal. The design implemented for maximum segment length of $N_{DFT} = 2\,048$ on targeted device XC6SLX45-3 utilizes 1 164 (≈2 %) of the device slice registers and 5 492 (20 %) of the device LUTs.

The FFT coprocessor memory utilizes 8 blocks of $1\,024 \times 32$ bit dual-port block RAMs: twiddle factors ROM is implemented as a block RAM. The Plasma registers and RAM are utilized as distributed memory, and both are composed in the device LUTs utilization. The N-S coprocessor memory is implemented as one $1\,024 \times 32$ bit block RAM. Hence the design utilizes 22 (≈18 %) of the device RAMB16BWER block RAMs. The design total memory utilization is 44 kB, of which 4 kB pertain to the N-S part coprocessor.

DSP48A1 blocks are used as 32×32 bit multipliers in both coprocessors. 32×32 bit multiplier is assembled from four DSP48A1 blocks: each block has one 18×18 bit multiplier [45]. The FFT coprocessor employs 24 DSP48A1 blocks: two radix-2 butterflies, where each one has one complex multiplier composed of three real multipliers [45]. The N-S coprocessor has only one real multiplier. Hence the total number of used DSP48A1s blocks rises up to 28 (48 % the device utilization).

The design maximum clocking frequency is constrained by its critical path. In our case the critical path occurs in the Plasma processor taking 19.059 ns; this allows us to

set clocking frequency up to $f_{CLK} = 50$ MHz. The critical path leads from processor controller through bus multiplexor to RAM.

4.5 Verification

To be certain of proper functionality of both optimized software and embedded implementation have been achieved the verification is mandatory. The verification plan goal on the system level is to validate the system output DZT spectral lines series against the computational model output. The verification uses coverage-driven constrained random-based approach [46]. The functional coverage requirement of the plan is to cover all three cases in Step 3 of the ADZT algorithm, see Sec. 4.1. Since the DZT is intended for spectral analysis of non-stationary signals, the test data must have non-stationary character. The test data were 40 segments of length N_{DFT} samples consisting of music of different genders (pop music, metal, classical music), vocal recordings, and few segments of Gaussian noise. The test data were selected as a subset of the computational model simulation test data set in Section 4.3.

The system level verification environment is depicted in Fig. 4.2. Under Test (DUT) is encapsulated in the verification environment written in behavioral VHDL code. The environment generates a system clock, initializes global reset, and stimulates the DUT with test data. The test data are loaded in Matlab and introduced to the DUT by file I/O interface. The computational model serves as a behavioral model, and it is executed in Matlab. The DUT output is compared in Matlab. The system was validated on both RTL and gate levels. The unit level verification was performed for each coprocessor using a similar scheme as system level verification. Each coprocessor was verified using its own verification environment and behavioral model on both RTL and gate levels. Real system HW realization was validated on the development board [44] using parallel interface [47] as system interface.

4.5.1 Results

The system error performance has been measured on the computational model against the original floating-point algorithm version. The measurement was performed as a part of the simulation in Sec. 4.3 with the same test data set. The performance is quantified using Signal to Noise Ratio (SNR)

$$SNR_{dB}(n) = 10\ \log_{10}\left(\frac{X(n)^2}{\{X(n) - X_{DUT}(n)\}^2}\right), \tag{4.8}$$

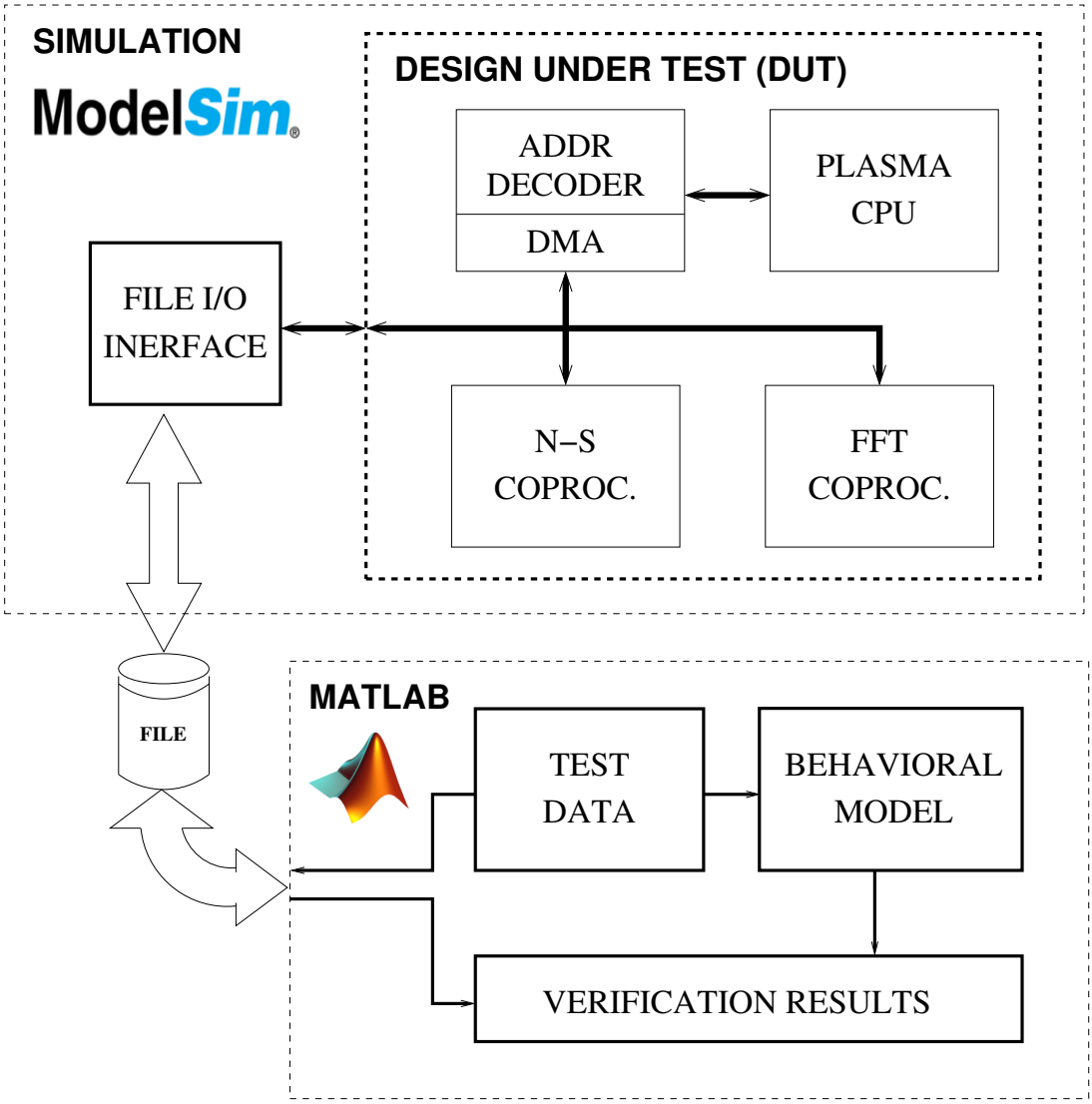

Figure 4.2: The system level verification schema of the system.

and mean SNR

$$SNR_{mean} = 10\ \log_{10}\left(\frac{1}{N}\sum_{n=1}^{N}\frac{X(n)^2}{\{X(n)-X_{DUT}(n)\}^2}\right), \tag{4.9}$$

where $X(n)$ is the floating-point model output value, and $X_{DUT}(n)$ is tested system output value computed using 32 bit fix point arithmetic. The fixed-point version of the algorithm adds quantization noise equivalent to $SNR_{mean} = 160$ dB and $\min\{SNR\} = 58$ dB. None of the computed bandwidths was selected incorrectly, which means that the fixed-point algorithm always selected the correct bandwidth and non-stationary part according to (4.2).

The total runtime for segment length of $N_{DFT} = 2\,048$ is 570 k clock cycles of the 50 MHz clock domain, see Tab. 9.1; thus, approximately 11.4 ms. The system is capable

of computing the STADZT results in real-time with ≈ 91 % overlap considering given segment length and signal sampling frequency. Note that fully SW solutions running on the Plasma processor has runtime of ≈ 400 ms, 20^6 clock cycles. The required computational power for a fully SW solution for given STADZT parameters estimation is 470 MIPS. Employed Plasma processor computational power is 50 MIPS of general purpose instruction set: maximum clocking frequency is 50 MHz [48]. The difference in computational power of ≈ 420 MIPS is overcome by HW parallelism.

4.6 Summary

Fixed-point software implementation of the ADZT algorithm was designed. Its proper functionality was guaranteed by the verification. The C implementation of the algorithm allows to compute one-shot ADZT spectrum of 2048 length in 100 μs. Compared with runtime of original Matlab implementation which runtime is 6.2 s, measured on a PC equipped with Pentium 4 processor, the fixed-point implementation allows to produce results in quick enough fashion.

First embedded implementation of the ADZT algorithm was designed. The algorithm asymptotic time complexity of $O(N^2)$, which is relatively high compared with the FFT algorithm, was revealed by its analysis. Such high time complexity was dealt with using the co-design methods. Dedicated HW parts bear main computational stress, while the SW part carries the less demanding calculations and algorithm decisions. The embedded solution is powerful enough to compute the STADZT spectrum of mono audio signal in real-time assuming sampling frequency of 16 kHz, segment length of 2 048 samples and overlap of 91 %. Computed real-time STADZT spectrum does not suffer from excessive information loss. Light and low-power processor with 50 MIPS of computational power is employed as a heart of the system; the whole solution computational power is equivalent to 420 MIPS processor with Harvard DSP CPU architecture and MAC unit. The system memory utilization is 44 kB from which the N-S part coprocessor utilizes 4 kB. The platform can be further adapted to support a simple application exploiting ADZT spectrum; the application can be implemented by SW on the processor with relatively low additional design efforts. The design targets FPGA device; therefore, it can be relatively easily integrated into a larger system on chip.

Chapter 5

Damped Exponential Signals Analysis

Damped exponentials model can represent different signals in a number of applications. For example, fault detection in rotating machinery [49], fault detection in power transmission [50, 51], health monitoring [52], structural statics [53], and others. The analysis of faulty rotating machinery, bearings, vibration signals is the main motivation behind this analysis. A model example of a faulty bearing vibration signal and its brief analysis is in Section 5.2.4. Note that it has been shown recently that the STADZT performs well detecting faults in rotating machinery, bearings, in comparison with other methods [54].

The analysis of the linear combination of damped exponentials has several established methods available. This work explores application to the analysis by spectral methods, the ADZT in particular. The spectral methods can be divided into parametric deterministic, parametric stochastic, and non-parametric. Non-parametric spectral methods can be used to detect damped harmonic signals; however, they do not estimate particular harmonic component damping and amplitude values. This can be limitting to its application. On the other hand, non-parametric methods do not suffer from instability due to unknown, and/or large, number of signal components as parametric methods do, which makes the results more stable in more complex signal cases. A representative is the DFT. Since the damped harmonic signal is non-stationary it is reasonable to assume non-stationary transforms, the ADZT. However, the analysis [55] shows that the ADZT is not suitable for damped harmonic signal analysis. The ADZT does not show the signal energy in the spectrum at all for some cases. This phenomenon is explored in more detail and a modification of the ADZT, performing better, is proposed, in Section 5.2 and Section 5.2.1, respectively. The modification results are compared against the DFT since the DFT is an inherent part of the ADZT.

Parametric deterministic spectral methods such as Prony method [56] and iterative

Steiglitz McBride [57] are well established. They are a common tool used to analyze damped exponentils signals. Both represent a sub-optimal solution of nonlinear identification problem using least squares error minimization. Stochastic spectral methods representatives are autocorrelation and covariance methods [58]. The covariance method normal equations are formally equal with the Prony method ones. The autocorrelation method normal equations converge to Prony ones for larger sample sequences as well. Therefore, the autocorrelation and covariance methods are not distinguished from the Prony one. The original Prony method is not a consistent estimator. There are extensions improving its robustness to noise; however, they are not considered since noise-free signal is assumed in this analysis. Another group of parametric spectral methods is autocovariance decomposition to signal and noise subspaces, such as MUSIC [59], Pisarenko, etc. Usage of the parametric methods is debated later in this chapter, in Section 5.1.

This work debates analysis of a real signal composed of a damped harmonic component without the presence of noise. Following discrete signal is assumed

$$s(n) = Ar^n \sin\left(\frac{2\pi f n}{f_s}\right), \qquad r \in (0,1), n \in \{0,1,\ldots,N-1\}. \tag{5.1}$$

It is a harmonic signal of amplitude A, frequency f, zero initial phase, sampled with sampling frequency of f_s and N samples long. The r^n is the signal envelope which is exponentially decaying according to $r^n = \exp(\sigma n)$ with damping coefficient $\sigma = \ln r$. An example of the signal is in Figure 5.1.

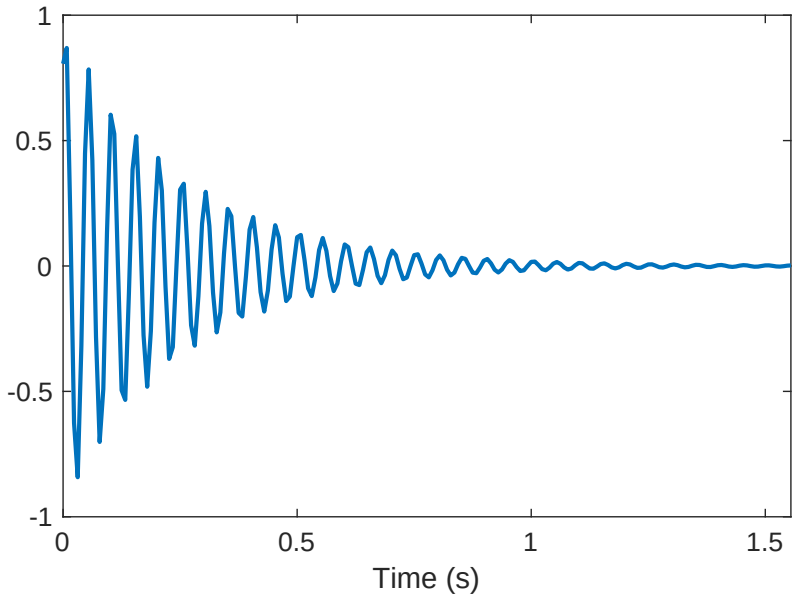

Figure 5.1: Example of the damped harmonic signal (5.1) of parameters: $A = 0$ dB, $f = 20$ Hz, $r = 0.97$, $N = 200$ samples, $f_s = 128$ kHz.

The signal power spectrum is given as

$$S(\exp(j\omega)) = Z^*\{s(n)\}Z\{s(n)\}_{|z=\exp(j\omega)}, \tag{5.2}$$

where the signal (5.1) in Z-domain is

$$Z\{s(n)\} = A\,\frac{rz^{-1}\sin\left(\frac{2\pi f}{f_s}\right)}{1-2rz^{-1}\cos\left(\frac{2\pi f}{f_s}\right)+r^2z^{-2}}. \tag{5.3}$$

Equation (5.3) can be interpreted as a system impulse response with complex conjugate poles having modulus r. The signal spectrum is non-zero in the whole frequency range. It varies from narrowband to wideband for small and large damping, respectively. The signal envelope time constant can be approximated for small damping $r \approx 1$ by impulse invariance method [60] as

$$\tau = \frac{1}{1-r}\frac{1}{f_s}. \tag{5.4}$$

5.1 Parametric spectral methods

At first let us focus at the AR model frequency response estimation methods: Prony and Steiglitz-McBride, and compare estimated power spectrum with the theoretical power spectrum (5.2). An important parameter of both methods is AR model order. Theoretically, the AR model order is given by the order of signal component Z-transformation (5.2), while no additional noise is assumed. In general number of signal components is unknown in practice, while selecting the model order is crucial. There are information statistical criteria which estimate number of degrees of freedom; however, they are out of the scope of this paper.

An important question is how to detect presence of a signal component and its frequency. A common approach is to manually select a pole pertaining to desired signal feature, component, and then extract the pole frequency. Consider example signal as mixture of two damped harmonic components (5.1) with parameters: $f_1 = 20$ Hz and $f_2 = 40$ Hz, $r_1 = r_2 = 0.97$, $A_1 = 0$ dB, $A_2 = -10$ dB, $N = 200$ samples long sampled with $f_s = 128$ Hz sampling frequency. The order of the signal frequency response is equal to four. However, both methods do not perform well for AR model order of four, see the Figure 5.2a. Estimated power spectrum almost ignores the second component peak. The second pole frequency error is relatively high, $\Delta f_2 \approx 4.5$ Hz for both methods. The results are better if higher AR model order is chosen. The reason is that the methods use biased covariance estimate and the signal has rather limited length due to damping. This does not allow covariance estimate to converge with small enough bias. More degrees of

freedom improve the behavior. The error in pole frequency localization decreases with higher model order; however, if number of poles in the model is higher, it becomes increasingly difficult to distinguish single pole to each component. The first peak in frequency is defined by multiple poles, see Figure 5.2d.

An option is to detected distinctive peaks in power spectrum and extract its frequencies, assuming that local maximum of a distinctive peak is close to a signal component frequency; however, there are cases of false peaks in power spectrum, see Figure 5.2b, thus this approach is tricky. In addition to that there are cases where a signal component does not have a peak in the power spectrum. Consider an example, where frequencies are spaced closer together, damping is higher and amplitude of the second component is smaller: $f_1 = 20$ Hz, $f_2 = 25$ Hz, $A_1 = 0$ dB, $A_2 = -20$ dB, $r_1 = r_2 = 0.90$. In this case the second component frequency is indeed hidden in the first component bandwidth, there is only a slight inflection around its frequency, see the theoretical power spectrum in Figure 5.3a. The cause is combination of larger bandwidth due to damping as well as smaller distance in amplitude and frequency. In case where order of AR model is equal to the signal Z-transformation order of four, the second component pole frequency has relatively large error of $\Delta f_2 \approx 8.6$ Hz, see Figure 5.3a. The error decreases for higher model orders, for example, order of sixteen has the error of $\Delta f_2 \approx 1.6$ Hz, see Figure 5.3b. But again it is problematic to detect the component presence since power spectrum peak search is inconclusive.

Usage of AR model frequency response methods leads to time consuming, per signal, usage in order to be able to tune the model parameter. This makes automatic detection troublesome. Another aspect is that to extract a detected component frequency is not straightforward. It can be difficult to assign correct pole to a peak in power spectrum, especially since a peak can be composed by more than a single pole. For these reasons we will not elaborate further about the methods. No extended comparison with the non-parametric methods is conducted. The Prony method is compared only illustratively on a single example.

Let us now focus at the methods based on auto-covariance decomposition to signal and noise subspaces, such as MUSIC, Pisarenko etc. These methods do not perform well compared to Prony one. The first reason is that there is no noise present in the analyzed signal. The second reason is that the auto-covariance decomposition requires more samples for reliable estimation, more than the analyzed signal is composed of due to damping. Due to both reasons, the estimated pseudo-spectrum suffers from false peaks significantly. Consider an example of signal identical to the one analyzed in Figure 5.2. Pseudo-spectrum estimated by MUSIC method [59] is in Figure 5.4. If the order of MUSIC model is higher than the signal frequency response order the pseudo-spectrum estimate

suffers from false peaks. Since the signal frequency response order is generally unknown, it is a significant problem. Thus this type of methods is not relevant to damped harmonic signal analysis and will not be further considered.

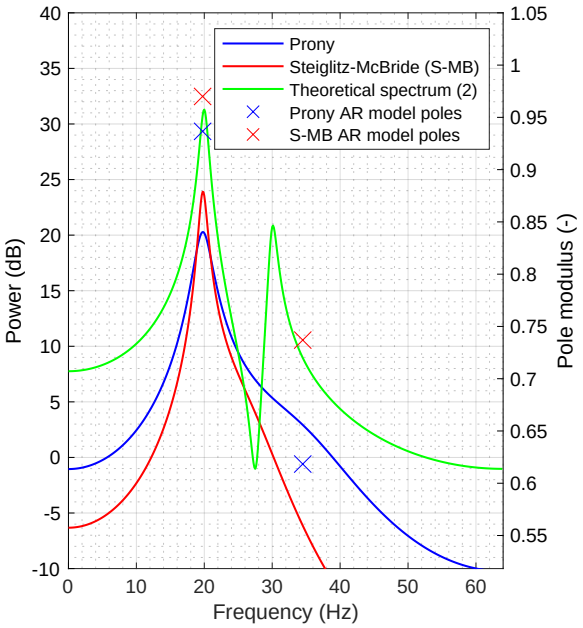

(a) AR model order $p = 4$, closest pole to each signal component frequency delta: $\Delta f_1 \approx 0.25$ Hz, $\Delta f_2 \approx 4.5$ Hz.

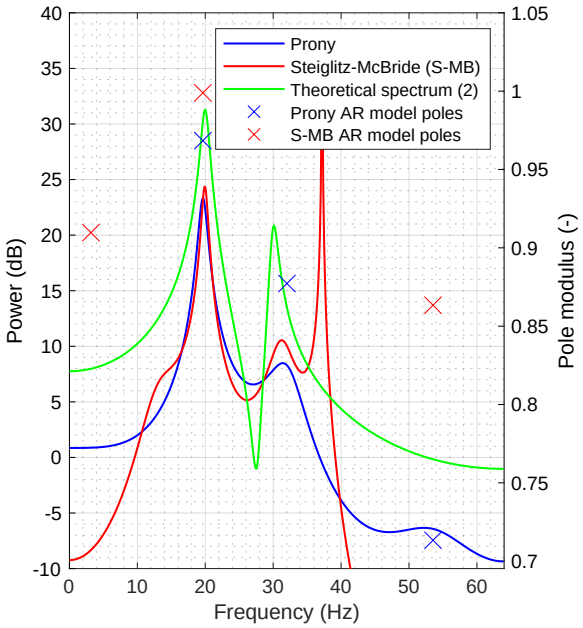

(b) AR model order $p = 8$, closest pole to each signal component frequency delta: $\Delta f_1 \approx 0.36$ Hz, $\Delta f_2 \approx 2.0$ Hz.

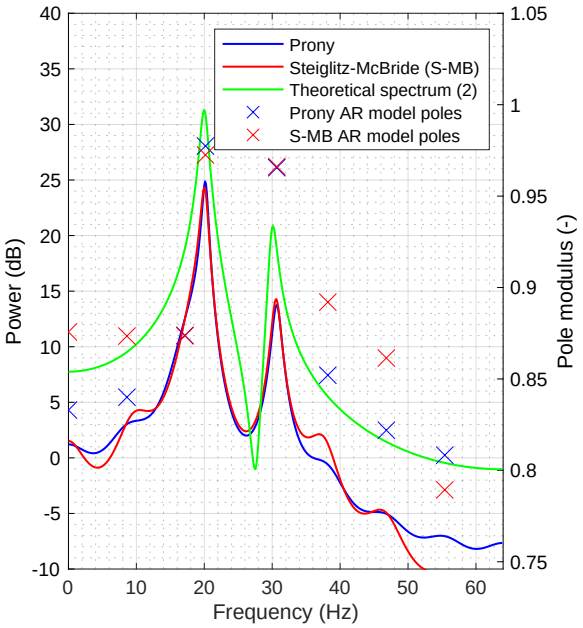

(c) AR model order $p = 16$, closest pole to each signal component frequency delta: $\Delta f_1 \approx 0.1$ Hz, $\Delta f_2 \approx 0.6$ Hz.

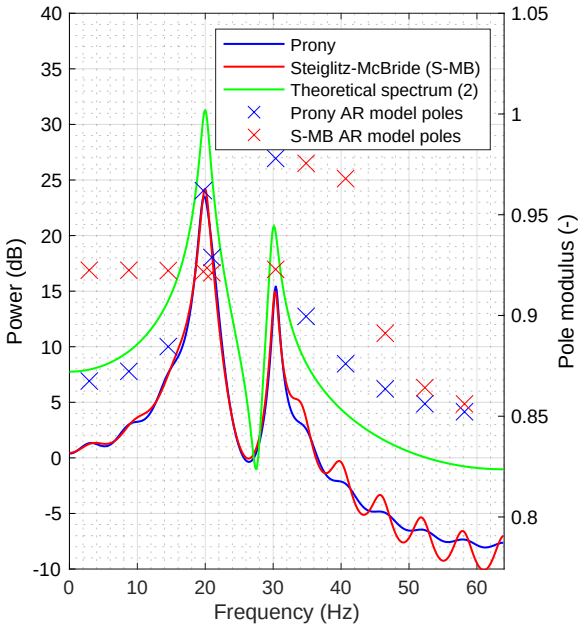

(d) AR model order $p = 24$, closest pole to each signal component frequency delta: $\Delta f_1 \approx 0.3$ Hz, $\Delta f_2 \approx 0.3$ Hz.

Figure 5.2: Estimated power spectrum for mixture of two damped harmonic components (5.1) for Prony and Steiglitz-McBride spectral parametric methods. The signal parameters are $A_1 = 0$ dB, $f_1 = 20$ Hz, $A_2 = -10$ dB, $f_2 = 30$ Hz, $r_1 = r_2 = 0.97$, $N = 200$ samples, $f_s = 128$ Hz. AR model poles are depicted as crosses. Poles with non-negative frequencies are displayed only; their complex conjugates are not.

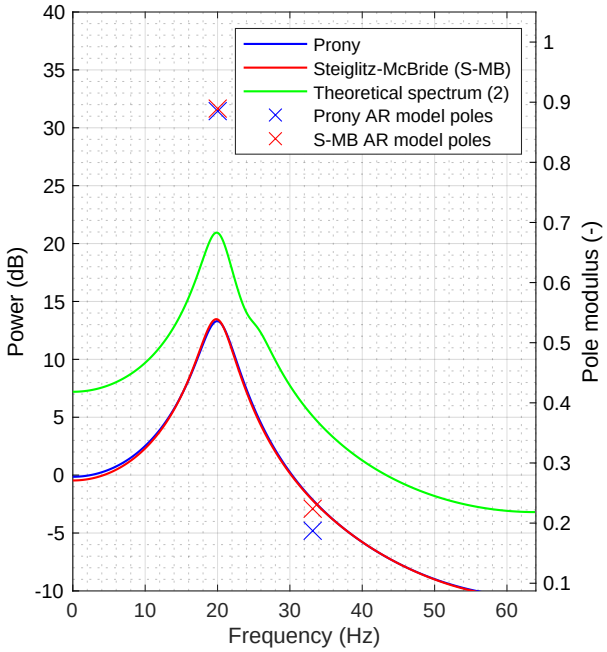

(a) AR model order $p = 4$, closest pole to each signal component frequency delta: $\Delta f_1 \approx 0.01$ Hz, $\Delta f_2 \approx 8.6$ Hz.

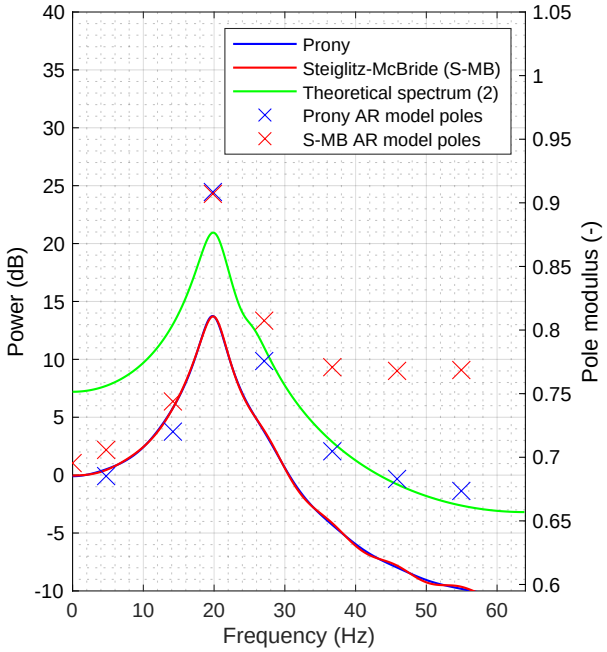

(b) AR model order $p = 16$, closest pole to each signal component frequency delta: $\Delta f_1 \approx 0.2$ Hz, $\Delta f_2 \approx 1.6$ Hz.

Figure 5.3: Estimated power spectrum for mixture of two damped harmonic components (5.1) for Prony and Steiglitz-McBride spectral parametric methods. The signal parameters are $A_1 = 0$ dB, $f_1 = 20$ Hz, $A_2 = -20$ dB, $f_2 = 25$ Hz, $r_1 = r_2 = 0.90$, $N = 200$ samples, $f_s = 128$ Hz. AR model poles are depicted as crosses. Poles with non-negative frequencies are displayed only; their complex conjugates are not.

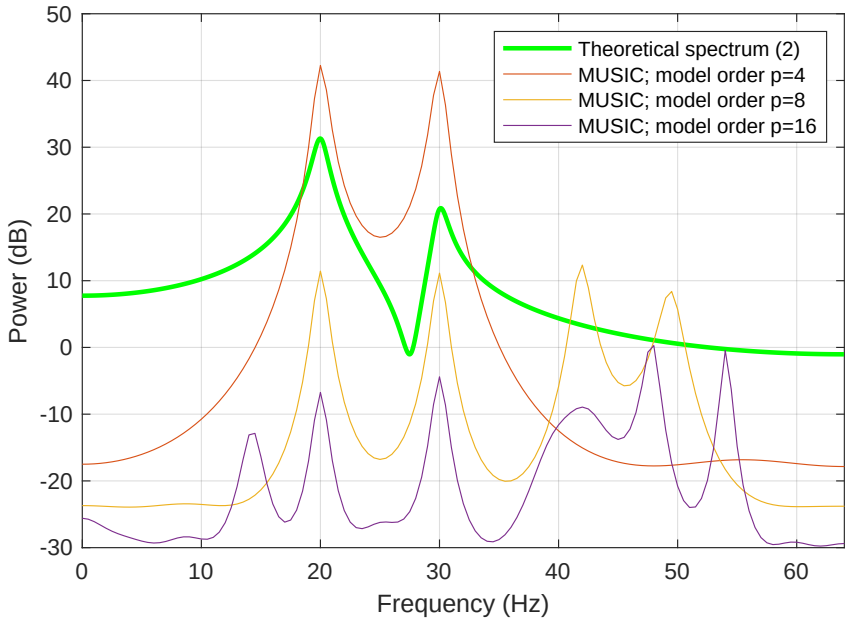

Figure 5.4: Estimated pseudo-spectrum via MUSIC for mixture of two damped harmonic components (5.1). The signal parameters are $A_1 = 0$ dB, $f_1 = 20$ Hz, $A_2 = -10$ dB, $f_2 = 30$ Hz, $r_1 = r_2 = 0.97$, $N = 200$ samples, $f_s = 128$ Hz.

5.2 Analysis with ADZT

Since the damped harmonic signal is non-stationary the non-parametric methods are used in their non-stationary form. The DFT as STDFT producing spectrogram and the ADZT as STADZT producing zologram. In order to acquire signal Power Spectral Density (PSD), spectrogram and zologram are marginalized using periodogram averaging method [1]. A question raises whether the periodogram averaging is a suitable method since its purpose is to estimate PSD of stationary stochastic signals; however, the signal (5.1) is deterministic, non-stationary and noiseless. DFT spectral lines within the signal bandwidth have consistent magnitude in all periodograms. The spectral leakage is inconsistent within different analysing window steps. Thus resulting PSD estimates the signal spectrum, while the spectral leakage is slightly reduced. The same can be said for the ADZT since it takes the DFT spectrum as a start point and filters it.

In order to distinguish different harmonic signal components in the spectrum, leakage reduction is the key. It is reduced by two mechanisms in this case: the former described periodogram averaging and by used window weighting function. Additionally by the ADZT optimization properties. Hamming, Blackman weighting windows are considered. Hamming since it is commonly used in signal analysis and Blackman for its usage in radar target detection, where is considered as the most suitable to prevent target masking [61]. The other windows are not considered, since the key aspect is low peak side lobe amplitude level which is lower for both Hamming and Blackman than the others.

Transform length is set to $N_0 = 128$ and step to one sample for both spectrogram and zologram. The transform length, or window length, is a question of frequency step which is set to $\Delta f = 1$ Hz. Note that the frequency localization cannot be increased by lengthening the transforms for larger dampings. The analyzed signal energy dissipates due to damping; longer transform length effectively manifests as zero padding, see the Figure 5.5b. The analysing window step of one sample yields as zologram 99 % overlap, which guarantees no information loss [38].

Figure 5.5c shows the spectrogram, Figure 5.5e the zologram, both with Hamming weighting window, and Figure 5.5g estimated PSD. The analyzed signal is the same as in Figure 5.2. It is noticeable that both spectrogram and zologram detect both harmonic components. The estimated PSD shows distinct peaks for both the STDFT and the STADZT.

The STADZT removes spectral leakage thoroughly; however, significant part of harmonic component energy is removed as well. The component with higher frequency is even removed completely for higher damping value $r = 0.90$, see figure 5.5f and 5.5h. The STADZT assumes the signal is of leakage characteristics and removes it. Experiments showed that the signal is completely removed if the signal time constant in samples

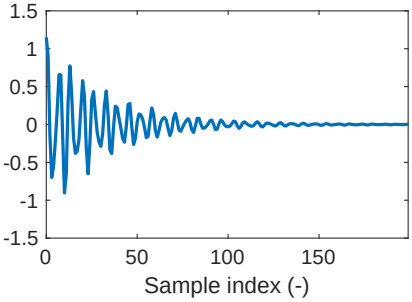

(a) Analyzed signal; damping of $r = 0.97$.

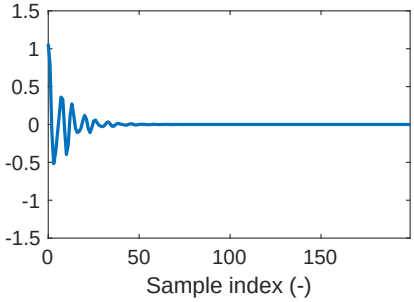

(b) Analyzed signal; damping of $r = 0.90$.

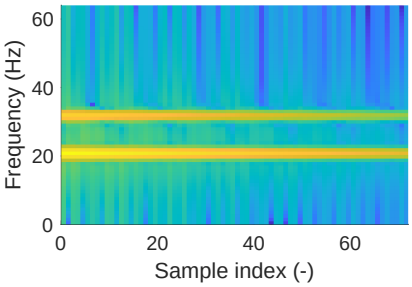

(c) Spectrogram; Hamming; damping of $r = 0.97$.

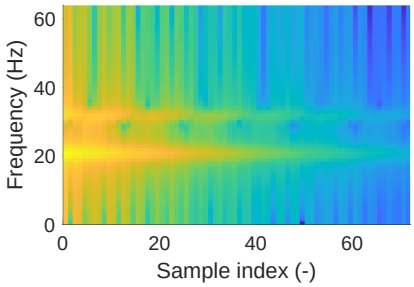

(d) Spectrogram; Hamming; damping of $r = 0.90$.

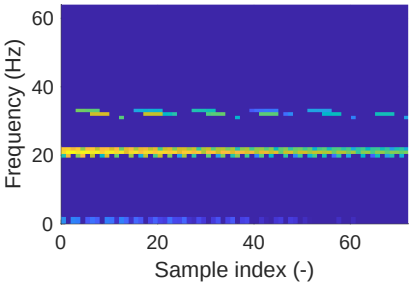

(e) Zologram; Hamming; damping of $r = 0.97$.

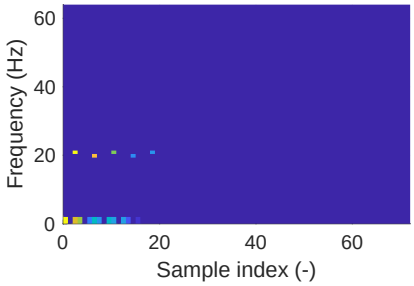

(f) Zologram; Hamming; damping of $r = 0.90$.

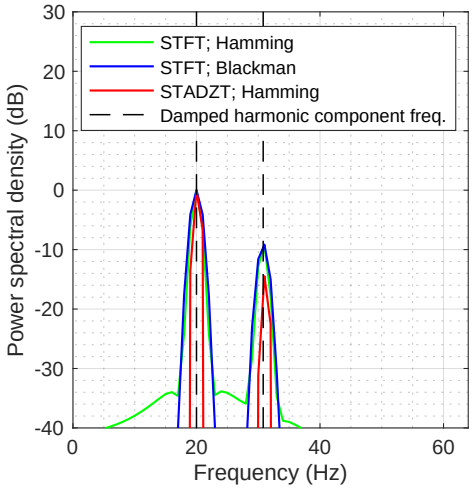

(g) Estimated PSD; damping of $r = 0.97$.

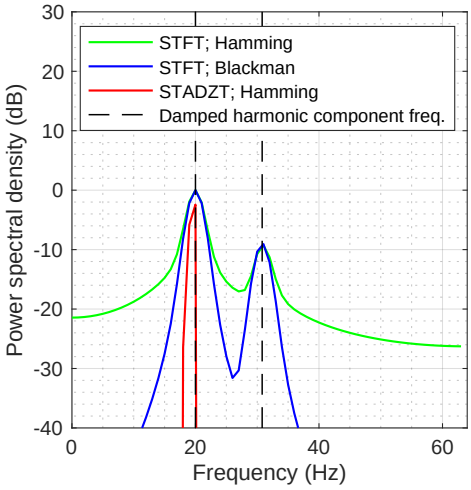

(h) Estimated PSD; damping of $r = 0.90$.

Figure 5.5: Analysis of mixture of two damped harmonic components (5.1) closely spaced in frequency; $f_1 = 20$ Hz, $f_2 = 30$ Hz, $A_1 = 0$ dB, $A_2 = -10$ dB, $N = 200$ samples, $f_s = 128$ Hz; both transforms lengths are 128 samples, steps are 1 sample.

$N_\tau = \lceil \tau f_s \rceil$ is roughly an order of magnitude shorter than analyzed window length N_0. This relation is examined in Table 5.1.

r_i	N_τ	$N_0 = 32$	$N_0 = 64$	$N_0 = 128$	$N_0 = 256$
0.97	33	✓	✓	✓	✓
0.91	11	✓	✓	✗	✗
0.86	7	✓	✗	✗	✗

Table 5.1: Ability of STADZT to detect harmonic signal of $f = 64$ Hz frequency sample by $f_s = 512$ Hz in relation to different signal time constant in samples N_τ and transformation length N_0. The symbol ✓ depicts the presence of the signal while the symbol ✗ the opposite.

5.2.1 ADZT Modification for Damped Harmonic Signals

The modification of the ADZT lays within reducing amount of spectral leakage removal in spectrum. Amount of spectral leakage removal is proportional to value of the transformation basis bandwidth, see the term definition in Section 4.1. Higher the bandwidth value is more aggressively are spectral leakage lines removed. Thus by introducing constrains of the bandwidth value during the optimization process the spectral leakage removal can be moderated. In general, two options are available. Firstly, to limit optimized bandwidth to a cap value. Secondly, to fix the bandwidth to a specific value. The experiments shown that if the bandwidth value is limited the optimization process does not behave property. A number of unpredictable artifacts emerges in the resulting spectrum. The second option, to fix the bandwidth to a specific value is a better option. Resulting spectrum does not suffer from artifacts. This modification introduces a trade-off between high frequency-time resolution precision of original ADZT and spectral leakage reduction. It was found by an experiment that the best performance, in terms of damped harmonic signal preservation and spectral leakage reduction, is provided when the bandwidth is limited to a value of 1. In case of the bandwidth being fixed to 1 the transform algorithm degrades into a much simpler form. There no need to find an optimal bandwidth by (4.2), the N-S part degrades to

$$N(\ell, m = 1) = (-1)^\ell S(\ell - 1). \tag{5.5}$$

Furthermore, the decision part of the algorithm reduces only to two cases. In the first case, where the signs of stationary part and N-S part are equal $sgn\{S(\ell)\} = sgn\{N(\ell)\}$, the spectral line is kept as stationary part (DFT spectral line) only $S_Z(\ell) = S(\ell)$. In the second case, where the signs are different $sgn\{S(\ell)\} \neq sgn\{N(\ell)\}$, the spectral line is removed $S_Z(\ell) = 0$.

The ADZT with fixed bandwidth to 1 (ADZTFB1) preserves the damped harmonic component spectral line in spectra in all cases specified in the Table 5.1, see Table 5.2, while the spectral leakage is still being reduced compared to STDFT results. Experiments showed the best performance in terms of spectral leakage and signal preservation is achieved with Hamming weighting window. Compare the results achieved by the modification with the original ADZT in Figure 5.6.

Short time version of the modified method, the (Short Time Approximated discrete Zolotarev transform with fixed bandwidth to 1 (STADZTFB1)), is defined by (2.22), where the ADZT function is replaced by Approximated discrete Zolotarev transform with fixed bandwidth to 1 (ADZTFB1).

r_i	N_τ	$N_0 = 32$	$N_0 = 64$	$N_0 = 128$	$N_0 = 256$
0.97	33	✓	✓	✓	✓
0.91	11	✓	✓	✓	✓
0.86	7	✓	✓	✓	✓

Table 5.2: Ability of STADZTFB1, the STADZT modification with bandwidth fixed to 1, to detect harmonic signal of $f = 64$ Hz frequency sample by $f_s = 512$ Hz in relation to different signal time constant in samples N_τ and transformation length N_0. The symbol ✓ depicts the presence of the signal while the symbol ✗ the opposite.

5.2.2 Benchmark

The main objective is to compare the STADZTFB1 against the STDFT. The Prony method is compared only illustratively.

Test1 Compare the STADZTFB1 and the STDFT performance in detection of multiple damped harmonic components randomly distributed in frequency.

Test2 Compare the STADZTFB1 and the STDFT performance in detection of damped harmonic components which are close together in frequency, close enough so that one component is partially masked by the other one's bandwidth.

The tests are realized by simulation which description follows. Each iteration a test signal as sum of harmonic components (5.1) with random parameters is generated, and PSD is estimated for each method. To evaluate the results a simple peak detector was designed. The peak detector locates local maximum and peak width in the PSD using a-priori knowledge of given component frequency. A peak is considered as detectable if the peak height is at least 3 dB. Note that false detections are not taken into account for simplicity. Frequency of a peak is calculated as spectral centroid, center of mass of frequency bins, within the peak. Error in estimated peak frequency is given by comparing

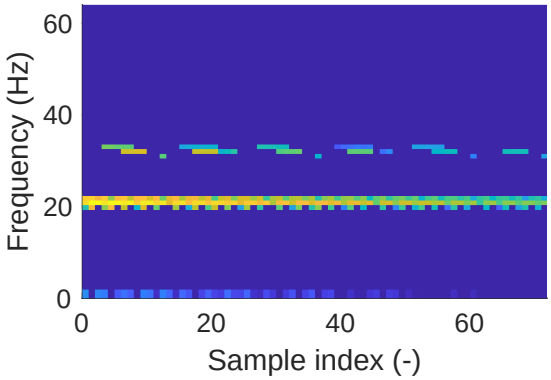

(a) Original STADZT zologram; Hamming; damping of $r = 0.97$.

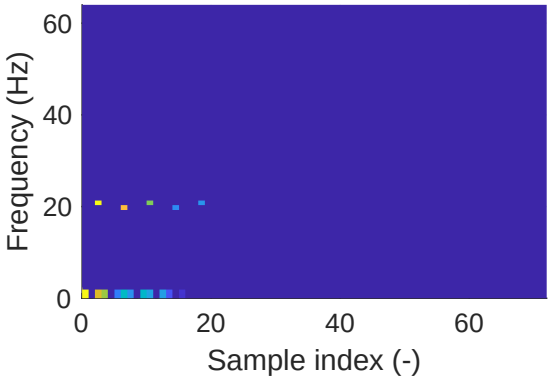

(b) Original STADZT zologram; Hamming; damping of $r = 0.90$.

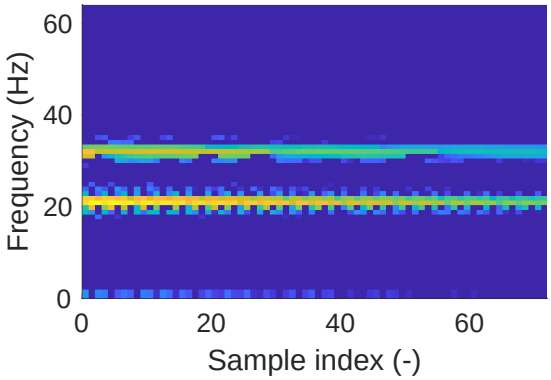

(c) STADZTFB1 zologram; Hamming; damping of $r = 0.97$.

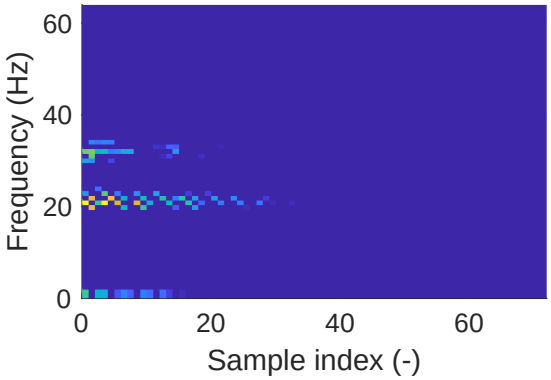

(d) STADZTFB1 zologram; Hamming; damping of $r = 0.90$.

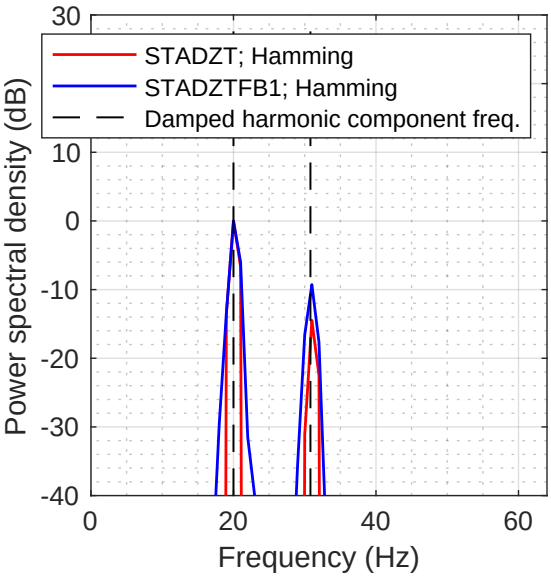

(e) Estimated PSD; damping of $r = 0.97$.

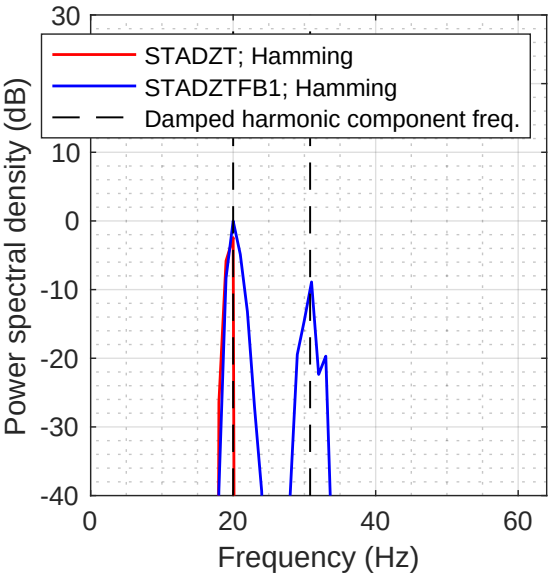

(f) Estimated PSD; damping of $r = 0.90$.

Figure 5.6: Analysis of mixture of two damped harmonic components (5.1) closely spaced in frequency; $f_1 = 20$ Hz, $f_2 = 30$ Hz, $A_1 = 0$ dB, $A_2 = -10$ dB, $N = 200$ samples, $f_s = 128$ Hz; both transforms lengths are 128 samples, steps are 1 sample.

the frequency against known given component frequency. The outputs of the simulation are histograms of component frequency error and peak height accumulated in multiple

iterations.

In case of the Test1 the simulation was set up as follows. The test signal contained N_C harmonic components (5.1) with random parameters: frequency uniformly spread within $\left(0, \frac{f_s}{2}\right)$, amplitude uniformly spread within $\langle 0, 1\rangle$ and damping uniformly spread within $\langle 0.90, 0.999\rangle$. The output statistics are given for all the components cumulatively.

In case of the Test2 the simulation was set up as follows. The test signal contained a pair of harmonic components (5.1) with defined distance in frequency f_{dist}, distance in amplitude A_{dist} and fixed damping for both; thus $f_2 = f_1 + f_{dist}$ (Hz) and $A_2 = A_1 + A_{dist}$ (dB). Frequency of the first component is spread uniformly within $\left(0, \frac{f_s}{2}\right)$ across iterations. Both distances in frequency and amplitude have additional normal noise of small variance, 0.5^2 Hz and 1 dB, respectively. The second, weaker in amplitude, hence masked, component output statistics are of interest.

5.2.3 Results

Simulation of the Test1, described in Section 5.2.2, was conducted with test signals containing $N_C = 6$ damped harmonic components (5.1) of random amplitude, damping and frequency across spectrum. Estimated frequency error histogram for STDFT with Hamming window is in Figure 5.7a and for STADZTFB1 in Figure 5.7b. The STDFT mean error is zero and standard deviation 0.09 Hz. The STADZTFB1 reaches mean error 0.27 Hz and standard deviation 0.44 Hz. Thus the STADZTFB1 frequency estimation is biased and deviates more. However, the error statistics are calculated only for occurrences where a peak was actually detected. The STDFT detected 85.8 % of components and the STADZTFB1 98.0 %. The STADZTFB1 is more capable of detection a component. Further experiments showed that the higher standard deviation of STADZTFB1 is partially caused by components which STDFT failed to detect. For the components STDFT detected correctly the STADZTFB1 standard deviation is 0.21 Hz, approximately double of the STDFT one.

Simulation of the Test2, described in Section 5.2.2, was conducted with test signals containing a pair of components with distance in frequency $f_{dist} = 5$ Hz and amplitude $A_{dist} = 20$ dB. Two simulations were done separately for lower $r = 0.97$ and higher $r = 0.90$ damping, illustrations of estimated PSDs for each damping are in Figure 5.8a and Figure 5.8b, respectively. The statistical results are given for the weaker component, the second one with lower amplitude and higher frequency.

The simulation for $r_{1,2} = 0.97$ revealed the STDFT frequency estimation error mean 0.02 Hz, standard deviation 0.13 Hz and 70.8 % peaks detected, see Figure 5.9a. In case of the STADZTFB1 error mean 0.06 Hz, standard deviation 0.08 and 99.5 % peaks detected, see Figure 5.9c. It is noticeable that the STDFT with Hamming window starts to fail

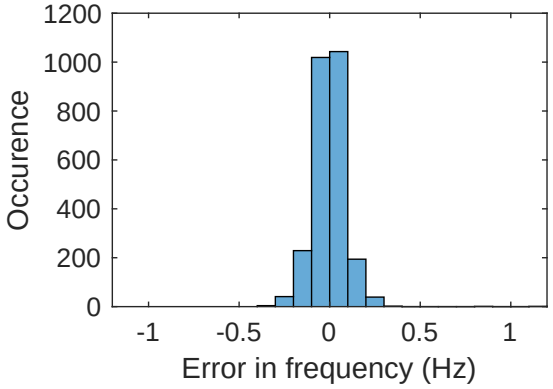

(a) Error of detected peak frequency estimation for STDFT, Hamming window.
$mean_{err} = 0.00$ Hz,
$std_{err} = 0.09$ Hz,
85.8 % peaks detected.

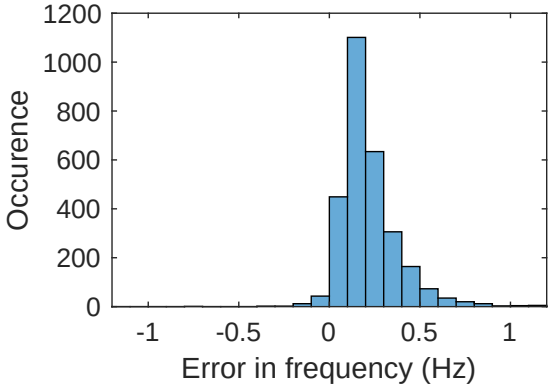

(b) Error of detected peak frequency estimation for STADZTFB1, Hamming window. $mean_{err} = 0.27$ Hz,
$std_{err} = 0.44$ Hz,
98.0 % peaks detected.

Figure 5.7: Simulation results for mixture of $N_C = 6$ damped harmonic components (5.1) with random frequency, amplitude and damping; the transform length is 128 samples ($\Delta f = 1$ Hz), step is one sample; 500 iterations.

in detection of components. Peak of the second component in the example Figure 5.8a is relatively small and can diminish in some other process realizations. This can be observed in peak height histogram of the method in Figure 5.9b. The STDFT is on the edge of 3 dB peak heigh, while the STADZTFB1 peak height distribution is quite tailed, see Figure 5.9d. The STDFT statistics further degrade if damping is higher, distance in frequency smaller or distance in amplitude higher, see the Table 5.3. Note that the STADZTFB1 keeps similar performance for all parameters in the table.

The second simulation of the Test2 with higher damping $r_{1,2} = 0.90$ revealed that the STDFT failed to detect all peaks. By looking at the example Figure 5.8b we can see that the peak of the second components is quite small in this case, actually, it was smaller than 3 dB, or non-existent, for all process realizations. On the other hand the STADZTFB1 detected 90.8 % of peaks with mean error 0.17 Hz and standard deviation 0.29 Hz, see Figure 5.10a. The peak height distribution in Figure 5.10b still offers margin for a detector. If a higher damping is used the STADZTFB1 performance degrades quickly, see the Table 5.4. Note that the STDFT failed to detected the second components in all cases of all parameters in the table.

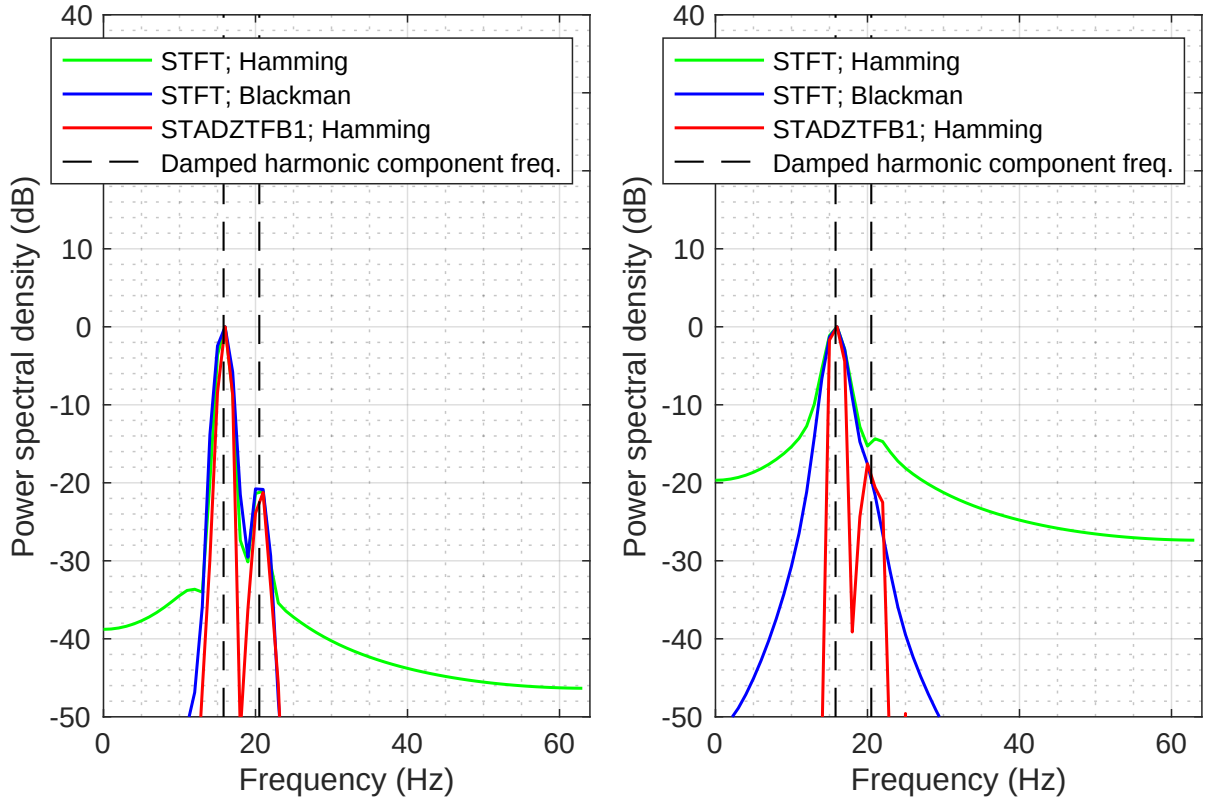

(a) Smaller damping $r_{1,2} = 0.97$.

(b) Larger damping $r_{1,2} = 0.90$.

Figure 5.8: An example of estimated PSD of two damped harmonic components closely spaced in frequency; $f_1 = 15.8$ Hz, $f_2 = 20.5$ Hz, $A_1 = 0$ dB, $A_2 = -20$ dB, $N = 200$ samples, $f_s = 128$ Hz; the transform length is 128 samples ($\Delta f = 1$ Hz), step is one sample.

f_{dist} \ A_{dist}	25 dB	20 dB	15 dB
4 Hz	0 %	0.14 Hz, 0.76 Hz, 14 %	0.07 Hz, 0.37 Hz, 83 %
5 Hz	0 %	0.08 Hz, 0.14 Hz, 79 %	0.05 Hz, 0.10 Hz, 97 %
6 Hz	0 %	0.07 Hz, 0.14 Hz, 99 %	0.05 Hz, 0.10 Hz, 100 %

Table 5.3: The STDFT with Hamming window performance in detection of the weaker component in mixture of two damped harmonic components closely spaced in frequency, where $f_2 = f_1 + f_{dist}$ (Hz), $A_2 = A_1 + A_{dist}$ (dB) and damping $r_{1,2} = 0.97$. The $f1$ is uniformly spread. $N = 200$ samples, $f_s = 128$ Hz; the transform length is 128 samples ($\Delta f = 1$ Hz), step is one sample. Entries are in following format: ($mean_{err}$, std_{err}, $P_{detection}$).

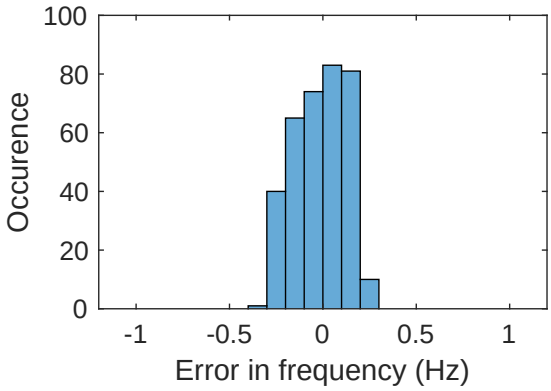

(a) Error of detected peak frequency estimation for STDFT, Hamming window.
$mean_{err} = 0.02$ Hz,
$std_{err} = 0.13$ Hz.

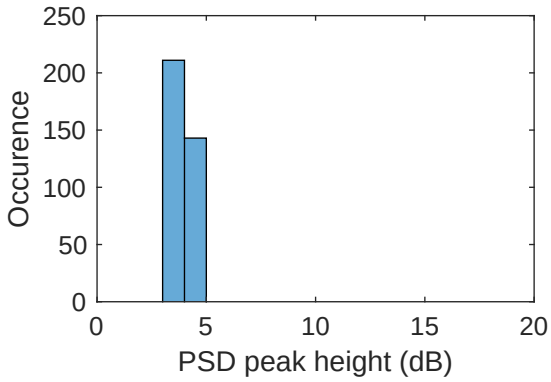

(b) Peak height histogram for STDFT, Hamming window.
70.8 % peaks detected.

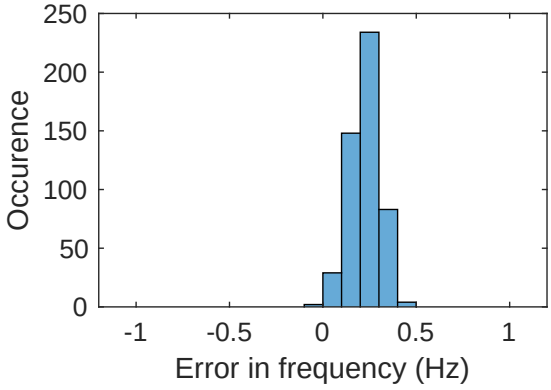

(c) Error of detected peak frequency estimation for STADZTFB1, Hamming window.
$mean_{err} = 0.06$ Hz,
$std_{err} = 0.08$ Hz.

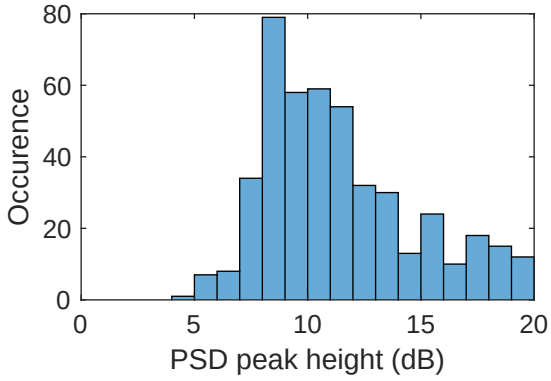

(d) Peak height histogram for STADZTFB1, Hamming window.
99.5 % peaks detected.

Figure 5.9: Simulation results of two damped harmonic components (5.1) mixture; $f_{dist} = 5$ Hz, $A_{dist} = -20$ dB, $r = 0.90$, $N = 200$ samples, $f_s = 128$ Hz and damping of $r_{1,2} = 0.97$; the transform length is 128 samples ($\Delta f = 1$ Hz), step is one sample; 500 iterations.

f_{dist} \ A_{dist}	25 dB	20 dB	15 dB
4 Hz	0.29 Hz, 0.51 Hz, 71 %	0.15 Hz, 0.28 Hz, 75 %	0.09 Hz, 0.19 Hz, 83 %
5 Hz	0.25 Hz, 0.49 Hz, 86 %	0.17 Hz, 0.29 Hz, 91 %	0.12 Hz, 0.16 Hz, 98 %
6 Hz	0.36 Hz, 0.58 Hz, 88 %	0.19 Hz, 0.22 Hz, 90 %	0.12 Hz, 0.09 Hz, 100 %

Table 5.4: The STADZTFB1 with Hamming window performance in detection of the weaker component in mixture of two damped harmonic components closely spaced in frequency, where $f_2 = f_1 + f_{dist}$ (Hz), $A_2 = A_1 + A_{dist}$ (dB) and damping $r_{1,2} = 0.90$. The $f1$ is uniformly spread. $N = 200$ samples, $f_s = 128$ Hz; the transform length is 128 samples ($\Delta f = 1$ Hz), step is one sample. Entries are in following format: ($mean_{err}$, std_{err}, $P_{detection}$).

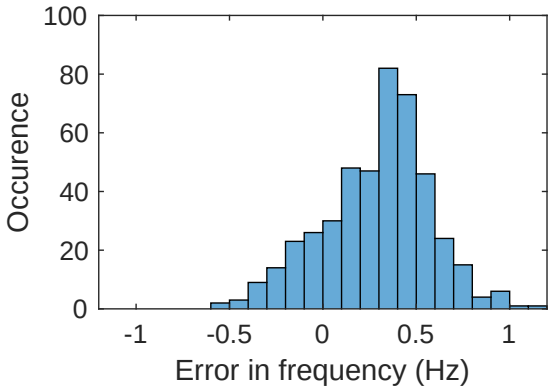

(a) Error of detected peak frequency estimation for STADZTFB1, Hamming window.
$mean_{err} = 0.17$ Hz,
$std_{err} = 0.29$ Hz.

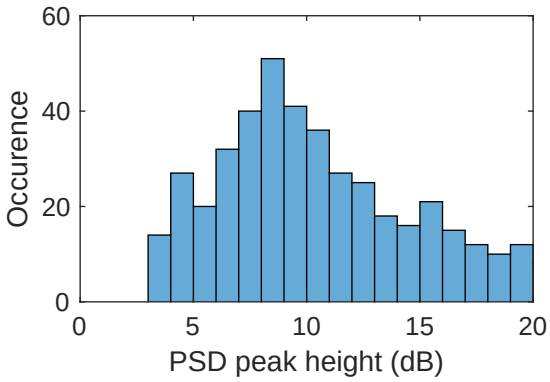

(b) Peak height histogram for STADZTFB1, Hamming window.
90.8 % peaks detected.

Figure 5.10: Simulation results of two damped harmonic components (5.1) mixture; $f_{dist} = 5$ Hz, $A_{dist} = -20$ dB, $r = 0.90$, $N = 200$ samples, $f_s = 128$ Hz and damping of $r_{1,2} = 0.90$; the transform length is 128 samples ($\Delta f = 1$ Hz), step is one sample; 500 iterations.

5.2.4 Bearing Fault Detection

This section presents a model example of a faulty bearing vibration signal analysis. The analysis is only illustrative. A proper analysis is out of the scope of this theses, a reader is kindly asked to refer to [62] for proper analysis methodology.

Firstly, a model example of simulated signal of bearing with inner race fault signal is generated according to [63]. The model signal is in Figure 5.11a, resulting spectrogram in Figure 5.11b, and resulting zologram using the ADZT modification STADZTFB1 in Figure 5.11c. By comparing the spectrogram and zologram, it is noticeable, the zologram has improved time resolution while keeping the same frequency resolution.

Secondly, an illustrative analysis of an example real world signal of faulty bearing with inner race fault is presented. The real world captured signal is in Figure 5.12a, resulting spectrogram in Figure 5.12b, and resulting zologram using the ADZT modification STADZTFB1 in Figure 5.12c. By comparing the spectrogram and zologram, it is noticeable, the zologram has improved time resolution while keeping the same frequency resolution. The illustrative real world signal analysis proves that the application of the STADZTFB1 is indeed possible.

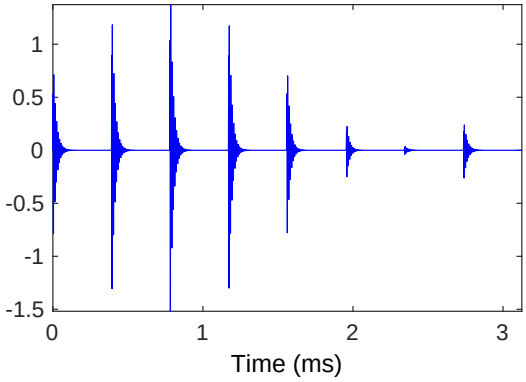

(a) Model vibration signal waveform.

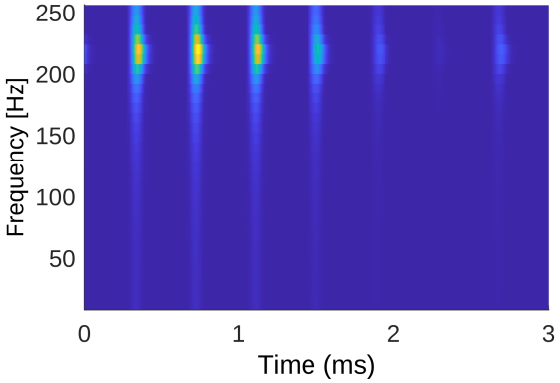

(b) STDFT spectrogram of the simulated vibration signal; Hamming window, window length of 64, and step of 1 sample.

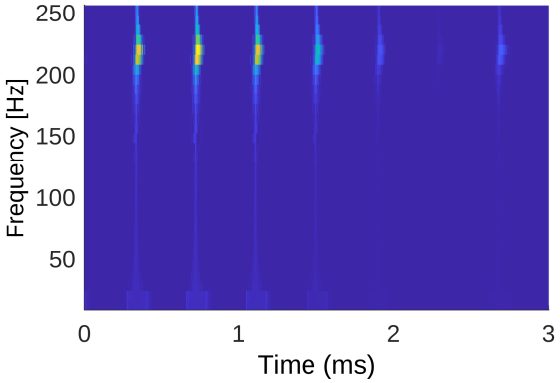

(c) STADZTFB1 zologram of the simulated vibration signal; Hamming window, window length of 64, and step of 1 sample.

Figure 5.11: A model example of simulated signal of bearing with inner race fault with shaft frequency change of 8 %. The simulated model vibration signal and resulting spectrogram and zologram, using the ADZT modification STADZTFB1.

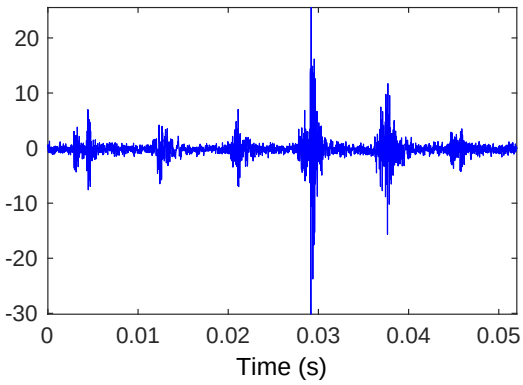

(a) An example of real world vibration signal waveform.

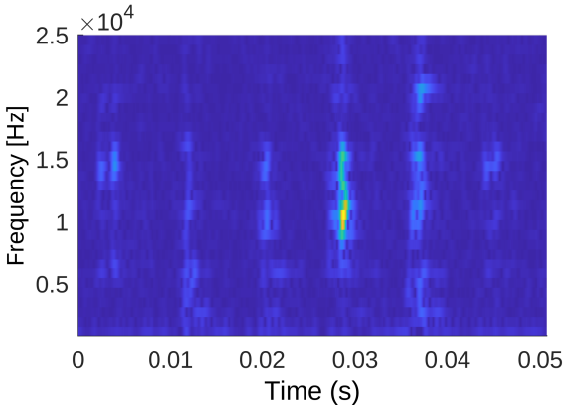

(b) STDFT spectrogram of a real world vibration signal; Hamming window, window length of 64, and step of 1 sample.

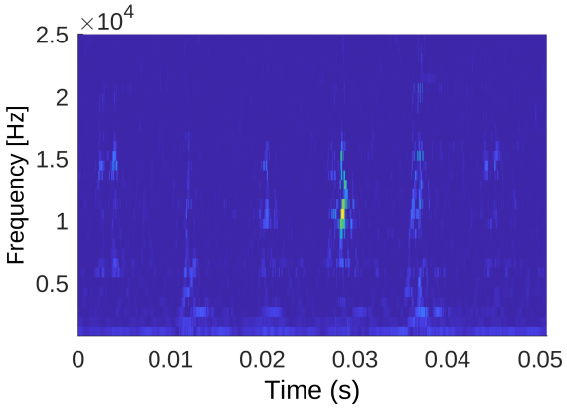

(c) STADZTFB1 zologram of the a world vibration signal; Hamming window, window length of 64, and step of 1 sample.

Figure 5.12: An example of a real world signal of bearing with inner race fault. The generated model vibration signal and resulting spectrogram and zologram, using the ADZT modification STADZTFB1.

5.3 Summary

Original STADZT ignores damped harmonic signal components completely in some cases. The transform considers spectrum of damped harmonic signal (5.1) to be spectral leakage. For higher damping coefficient values the signal's spectrum gets removed completely. Experiments shown that the spectrum is completely removed where analyzed signal time constant (5.4) is roughly a magnitude shorter than the transform length N_0.

The transform modification was proposed overcoming this issue by limiting the bandwidth, see the term definition in Section 4.1, of transformation basis composed of approximated polynomials. This modification introduces a trade-off between high frequency-time resolution precision of original ADZT and spectral leakage reduction. The ADZT with fixed bandwidth to 1 (ADZTFB1) keeps the spectral lines pertaining to a harmonic component frequency, while removes spectral leakage as well as sides of particular component bandwidth. The modification allows to detect closely separated, partially masked, damped harmonic components with better performance than the STDFT. The best STADZTFB1 performance is achieved with Hamming weighting window.

The example of faulty bearing analysis shows it is possible to employ the STADZTFB1.

It has been shown that the parametric spectral methods, namely Prony and Steiglitz-McBride, are not suited to detect damped harmonic signal components relatively closely spaced in frequency. The illustrative example is in Figure 5.3b, where the signal parameters are the same as in the second simulation of the Test2, see Section 5.2.2. The model parameter was set to $p = 16$, where the power spectrum estimates well and a pole can be still easily assigned to both components. However, detectability of the weaker component is questionable without a-priori knowledge of its existence and frequency. The frequency estimation error for the weaker component is 1.6 Hz.

Chapter 6

Symmetrical Zolotarev Polynomials

Symmetrical Zolotarev polynomials (ZP) are employed in spectral analysis, initially proposed by Radim Špetík in his doctoral thesis [35]. Zolotarev polynomial analytical derivation is described in the thesis as well. The main interest from spectral analysis point of view is in the symmetrical ZP of the first and the second kind, even and odd polynomials, respectively. They are described in Section 6.2. There are also Zolotarev polynomials of the third and fourth kind; they lay however out of the scope.

Since generation of the ZPs is not trivial its numerical stability is of interest. The polynomial generation is especially crucial for application in spectral analysis; polynomials of high degrees up to thousands are required to be generated correctly. Evaluation of symmetrical ZP, symmetrical ZP the first kind in particular, is elaborated from numerical point of view in Section 6.3.1. The algorithm to generate the symmetrical ZP of the second kind is closely related to one of the first kind; thus the findings related to the generation of polynomials of first kind can be approximately applied to generation of the second kind ones.

Zolotarev polynomials are a generalization of Chebyshev polynomials. Therefore, it is prudent to first describe the Chebyshev polynomials prior to Zolotarev ones, as is in the following section.

6.1 Chebyshev Polynomials

The Chebyshev polynomial $T_n(x)$ of the first kind is defined by the relation [64]

$$T_n(x) = cos(n\theta) \quad when\ x = cos(\theta). \tag{6.1}$$

Variable x on interval $\subset [-1, 1]$ corresponds to variable θ on interval $\subset [0, \pi]$. Nonlinear transformation of variable x onto variable θ converts $T_n(x)$ into function $cos n\theta$ as

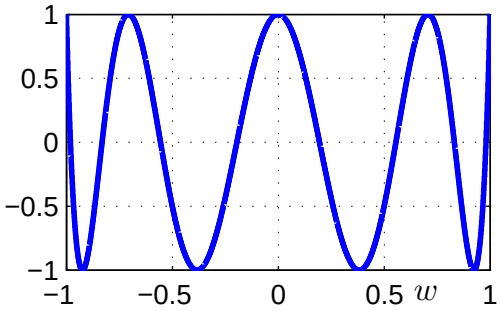

(a) $T_n(x)$ on range $[-1, 1]$; $n = 4$.

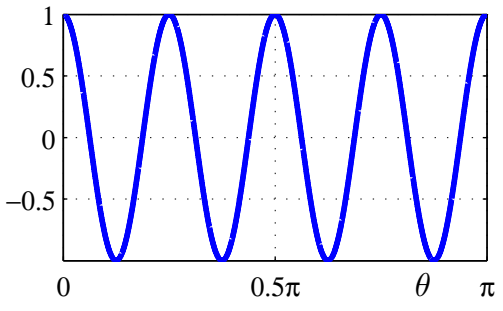

(b) Corresponding function $cos\, n\theta$ on range $[0, \pi]$; $n = 4$.

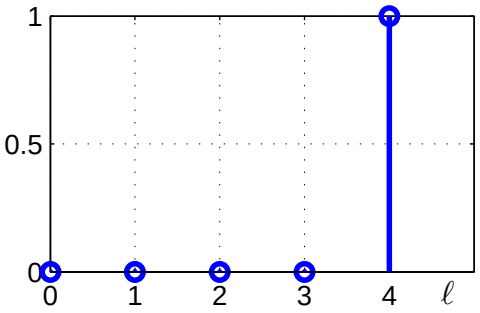

(c) The spectrum of $cos\, n\theta$; $n = 4$.

Figure 6.1: An illustration of mapping of $T_n(x)$ onto $cos\, n\theta$ by transformation $x = cos\, \theta$ together with its spectrum.

illustrated in Fig. 6.1a and Fig.6.1b, respectively.

The Chebyshev polynomial $T_n(x)$ of degree n can be generated iteratively by following forward recursion [64]

$$T_n(x) = 2x\, T_{n-1}(x) - T_{n-2}(x), \quad n = 2, 3, \ldots, \tag{6.2a}$$

with initial condition

$$T_0(x) = 1, T_1(x) = x. \tag{6.2b}$$

Substituting for $x = cos\, \theta$ in (6.2) results in well-known trigonometric identity

$$\begin{gathered} cos\, n\theta = 2\, cos\, \theta\ cos(n-1)\theta - cos(n-2)\theta, \\ n = 2, 3, \ldots. \end{gathered} \tag{6.3}$$

Nevertheless, this formula can not be used for computing ZP1S.

The solution of the recursion (6.2) results in a formula which describes the Chebyshev polynomial of the first kind of degree n in terms of power of x as [64]

$$T_n(x) = \sum_{k=0}^{n/2} c_k^{(n)} x^{n-2k} \qquad \frac{n}{2} \subset \mathbb{N}, \tag{6.4a}$$

where coefficients

$$c_k^{(n)} = (-1)^k\, 2^{n-2k-1}\left[2\binom{n-k}{k} - \binom{n-k-1}{k}\right] \quad (2k < n) \tag{6.4b}$$

and

$$c_k^{(2k)} = (-1)^k \quad (k \geq 0). \tag{6.4c}$$

Thus, the Chebyshev polynomial $T_n(x)$ of order n can be also written as power expansion with coefficients given by binomial expansion.

From spectral signal analysis point of view the Chebyshev polynomials can be interpreted in time spectral domain as follows. If we regard the continuous-time variable x (or $theta$) as "time" then Chebyshev polynomial $T_n(x)$ (or $cos(n\theta)$) can be regarded as a signal waveform. Chebyshev polynomial $cos(n\theta)$ can be converted to a spectral domain using the Fourier series concept. Because we deal with an even symmetrical polynomial the Fourier transform degrades into cosine transform. The resulting spectrum of Chebyshev polynomial $cos(n\theta)$ of degree n is given

$$a_\ell = \frac{1}{\pi}\int_0^\pi cos(n\theta)e^{-j\ell\theta 2\pi/T_0}d\theta, \tag{6.5}$$

where $T_0 = \pi$ for this case. Using the principle of the orthogonality we obtain only one nonzero spectral coefficient on frequencies $\frac{\ell 2\pi}{T_0}$. The Chebyshev polynomial and its corresponding spectrum is shown in Fig. 6.1b and Fig. 6.1c, respectively. This interpretation will be generalized later for Zolotarev polynomials. It should be noted, it is possible to introduce the opposite interpretation, i.e. spectral coefficient $a_\ell,\ \ell = 0, 1, ..., n$ represent the impulse response of a filter in time domain and Chebyshev polynomial can be considered as the frequency response of the respective filter. This approach is used in filter design using ZP [28, 29, 30, 34]. The standard trigonometric identity holds

$$\begin{aligned} T_n^2(x) + (1-x^2)U_{n-1}^2(x) &= 1, \\ cos^2(x) + sin^2(x) &= 1 \end{aligned} \tag{6.6}$$

where n is the degree of polynomials, $T_n(x)$ is the Chebysev polynomial of the first kind and $U_n(x)$ is the Chebysev polynomial of the second kind. The Euler formula holds

$$\begin{aligned} cos(\theta) + isin(\theta) &= e^{i\theta}, \\ cos(\theta) + i\frac{d}{d\theta}cos(\theta) &= e^{i\theta}. \end{aligned} \tag{6.7}$$

6.2 Symmetrical Zolotarev Polynomials

The symmetrical ZP of the first kind can be expressed by Chebysev polynomial as

$$Z_{m,m}(k',w) = (-1)^m T_{2m}(\sqrt{\frac{w^2-k'^2}{1-k'^2}}) = (-1)^m T_m(\frac{2w^2-1-k'^2}{1-k'^2}), \tag{6.8}$$

where k' is the modulus of elliptical functions. The symmetrical ZP of the second kind can be expressed by Chebysev polynomial as

$$\mathcal{Z}_{m-1,m-1}(k',w) = (-1)^m \frac{2}{1-k'^2}\, U_{m-1}(\frac{2w^2-1-k'^{\,2}}{1-k'^{\,2}}). \tag{6.9}$$

Both types of ZP can be generated using an effective and robust algorithm [28, 34]. By substitution $x = \frac{2w^2-1-k'^2}{1-k'^2}$ in (6.6) we obtain standard identity for ZP as

$$T_m^2(\frac{2\,w^2-1-k'^2}{1-k'^2}) + 4\,\frac{(1-w^2)(w^2-k'^2)}{(1-k'^2)^2}\, U_{m-1}^2(\frac{2\,w^2-1-k'^2}{1-k'^2}) = 1. \tag{6.10}$$

Zolotarev cosine can be obtained by comparing the ZP standard identity (6.10) with the trigonometric one (6.6) as

$$\mathrm{Zcos}(m,k',\phi) \doteq (-1)^m Z_{m,m}(k',w)|_{w=\cos\phi} = \sum_{\ell=0}^{m} a(2\ell) T_{2\ell}(\cos\phi) = \sum_{\ell=0}^{m} a(2\ell)\cos 2\ell\phi. \tag{6.11}$$

An example of Zcos is in Fig. 6.2, where the meaning of k' is shown. The Zolotarev sinus could be obtained from the identities in the same fashion as

$$(-1)^m\sqrt{(1-w^2)(w^2-k'^2)}\,\mathcal{Z}_{m-1,m-1}(w,\kappa) = \frac{2}{1-k'^2}\sqrt{(1-w^2)(w^2-k'^2)}\sum_{\ell=0}^{m-1}\alpha(2\ell)U_{2\ell}(w). \tag{6.12}$$

However, the square rooted term is negative in interval of $w \subset (-k'^2, +k'^2)$: the result is in complex range. Prof. Vlček developed a simple modification [65], which allows to express Zolotarev sinus in real range as

$$\begin{aligned}\mathrm{Zsin}(\phi) &= (-1)^m w\,\sqrt{1-w^2}(1-k'^2)\mathcal{Z}_{m-1,m-1}(w,\kappa)|_{w=\cos\phi},\\ &= 2w\,\sqrt{1-w^2}\sum_{\ell=0}^{m-1}\alpha(2\ell)U_{2\ell}(w)|_{w=\cos\phi},\\ &= \sqrt{1-w^2}\sum_{\ell=1}^{m}\beta(2\ell-1)U_{2\ell-1}(\cos\phi).\end{aligned} \tag{6.13}$$

The modification actually forces $k' = 0$ in $\frac{2}{1-k'^2}\sqrt{(1-w^2)(w^2-k'^2)}$. The $\mathrm{Zsin}(\phi)$ is in real range; However, there is a price to pay: its non-equiripple behavioral in $w \subset$

$(-1, k') \cup (k', 1)$, see Fig. 6.3.

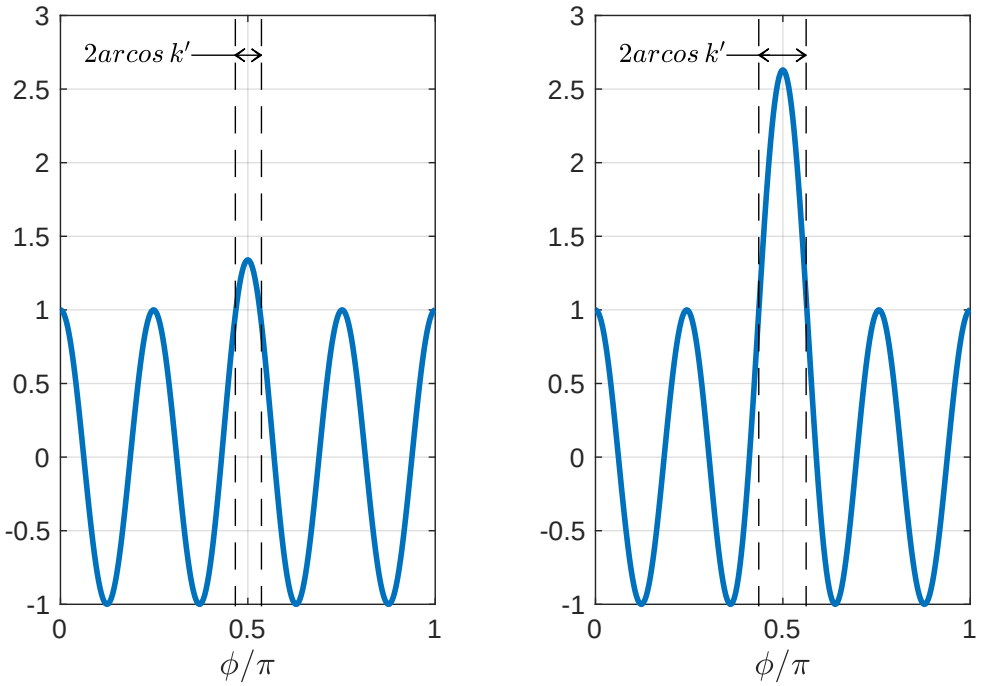

(a) $Zcos(\phi)|m = 4, k' = 0.1$ (b) $Zcos(\phi)|m = 4, k' = 0.2$

Figure 6.2: An example of Zolotarev cosine of the first kind (6.11).

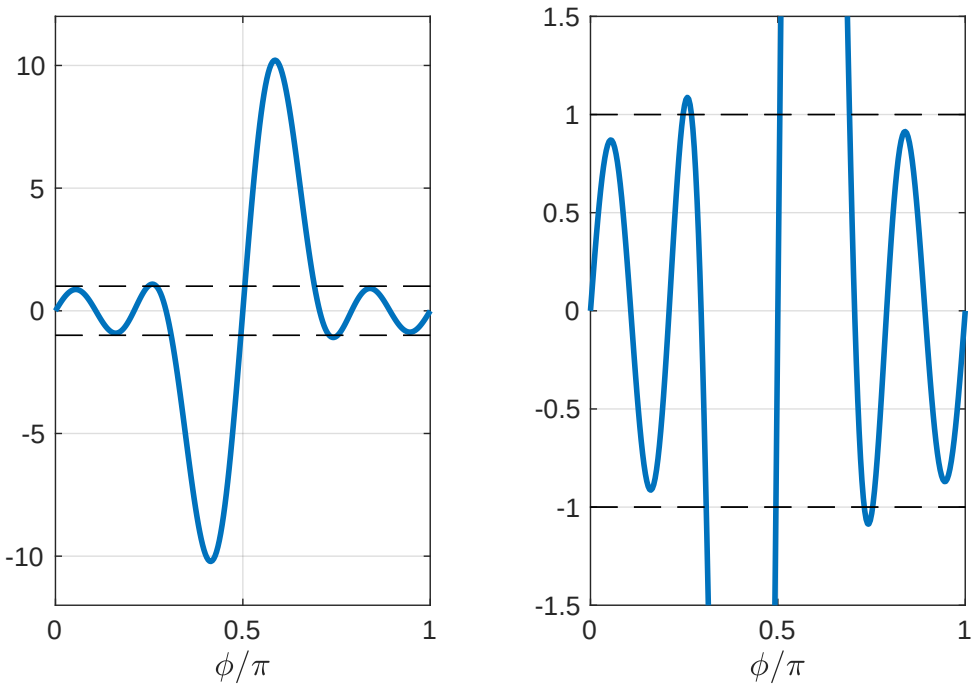

(a) (b) Zoomed vertical axis.

Figure 6.3: An example of Zolotarev sinus of the second kind $(\phi)|m = 4, k' = 0.5$ (6.13).

6.3 Symmetrical Zolotarev polynomial of the first kind

The ZP1S can be expressed using the Chebyshev polynomial of the first kind as

$$Z_p(w, k') = (-1)^{\frac{p}{2}} T_p\left(\sqrt{\frac{w^2 - k'^2}{1 - k'^2}}\right) \quad \frac{p}{2} \subset \mathbb{N}, \tag{6.14}$$

where p is the degree of Chebyshev polynomial as well as of the ZP1S, see [28]. The ZP1S is defined on a standard interval for polynomial approximation $w \subset [-1, 1]$. The k' is the modulus of elliptical functions. The ZP1S main features are equiripple behavioral on two disjoint intervals $w \subset [-1, k'] \cup [k', 1]$ and elevated central lobe on the interval $w \subset [-k', k']$. Thus, the k' can be interpreted as the half-width of the central lobe bounded by intersections with the absolute values[1] of one, see Fig. 6.4. The parameter k' is given on the interval $[0, 1)$. The polynomial degree must be even as the polynomial $Z_p(w, k')$ is even symmetrical. Note that the polynomial has p zeros.

The ZP are members of an elliptical functions family of which mathematical discipline is rather difficult. To understand the ZP1S nature with ease we can approach the Zolotarev polynomial as a trigonometric function. Employing this approach the ZP1S is expressed

[1]The central lobe of the ZP1S of degree p is positive or negative when $\frac{p}{2}$ is even or odd, respectively.

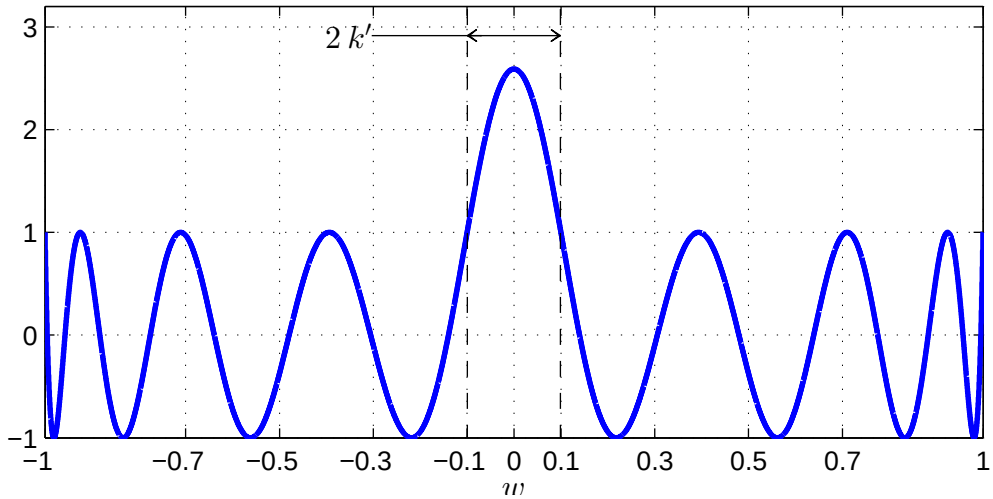

Figure 6.4: The symmetrical Zolotarev polynomial of the first kind $Z_p(w, k')$ for $p = 8$ and $k' = 0.1$.

by the Chebyshev polynomial of the first kind: by using the substitution $w = cos\,\theta$ for ZP1S, denoted as $Z_p(w, k')|w = cos\,\theta$, we obtain a function, which can be interpreted as a cosine with the central lobe elevated, see Fig. 6.5a. Similar approach is used also in [28] for the approximation of FIR filters by a ZP. For $w = cos\,\theta$ and $k' = 0$ the $Z_p(w, k')$ degenerates to the trigonometric cosine of the degree p. This can be easily justified: by substituting $k' = 0$ in (6.14) we obtain $Z_p(w, k') = (-1)^{\frac{p}{2}} T_p(w)$, and by using the substitution $w = cos\,\theta$ we obtain $cos\,p\theta$.

The global extreme of the ZP1S is influenced by both k' and p: its absolute value gets larger when k' or p get larger. This phenomena become obvious by looking at Fig. 6.5. Compare Fig. 6.5a with Fig. 6.5b, where the degree is the same and k' is 0.10 or 0.11, respectively. Furthermore, compare Fig. 6.5a with Fig. 6.5c, where the k' is the same and the degree is 16 and 20, respectively. sRecent analysis shows the ZP1S are orthogonal in both disjoint intervals $w \subset [-1, k'] \cup [k', 1]$ for fixed k' and degrees $p = 2, 4, 6, \ldots$. These findings are yet to be published.

The equation (6.14) can be rewritten using

$$T_{2n}(x) = T_n(2x^2 - 1)$$

as

$$Z_p(w, k') = (-1)^{\frac{p}{2}} T_{\frac{p}{2}}\left(\frac{2w^2 - 1 - k'^2}{1 - k'^2}\right) \quad \frac{p}{2} \subset \mathbb{N}, \tag{6.15}$$

Use of this equation for future generation of ZP1S is beneficial compared with use of (6.14) for three reasons. Firstly, it lowers the upper index of the sum in equation (6.4a) to the half. Secondly, the number of iterations of recurrence (6.2) is also reduced to the half.

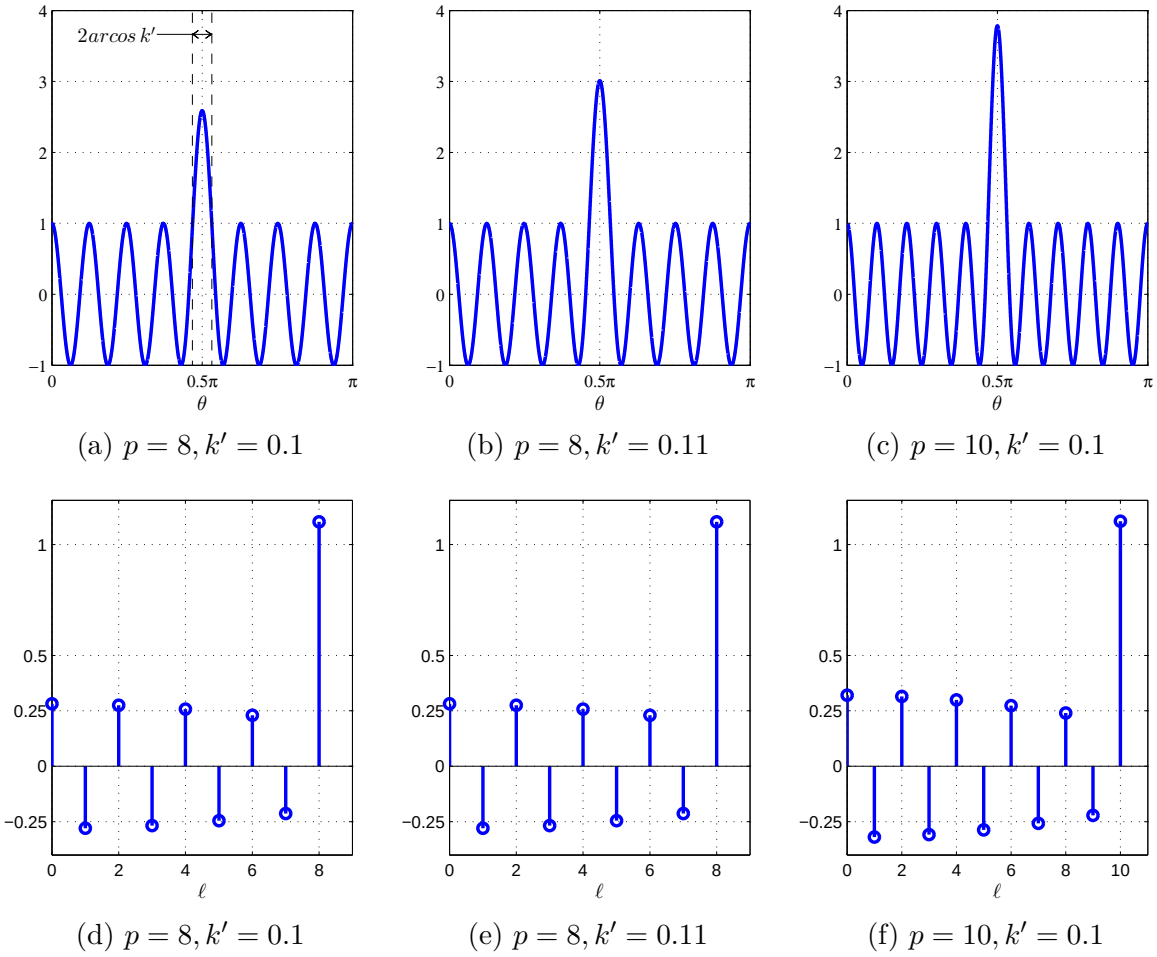

(a) $p = 8, k' = 0.1$ (b) $p = 8, k' = 0.11$ (c) $p = 10, k' = 0.1$

(d) $p = 8, k' = 0.1$ (e) $p = 8, k' = 0.11$ (f) $p = 10, k' = 0.1$

Figure 6.5: Symmetrical Zolotarev polynomial of the first kind $Z_p(w, k')|w = cos\theta$ in Fig. a-c; and together with its spectral coefficients in Fig. d-f .

Thirdly, the argument of $T_{\frac{p}{2}}(x)$ is free of the square root which is a rather problematic computational operation. For all three reasons, the use of equation (6.15) enables to enumerate the ZP1S with less errors compared with equation (6.14).

It is also worthy to note that the ZP1S can be alternatively expressed as the linear combination of the Chebyshev polynomials $T_n(x)$ as [35, 28].

$$Z_p(w, k') = (-1)^{\frac{p}{2}} \sum_{\ell=0}^{\frac{p}{2}} a(2\ell) T_{2\ell}(w) \quad \frac{p}{2} \subset \mathbb{N}. \tag{6.16}$$

By using the substitution $w = cos\theta$ in (6.16) we obtain

$$Z_p(w, k')|_{w=cos\phi} = \sum_{\ell=0}^{\frac{p}{2}} a(2\ell)\ cos(2\ell\theta)\ \frac{p}{2} \subset \mathbb{N}. \tag{6.17}$$

The $a(2\ell)$ coefficients[2] are, in fact, the coefficients of the Fourier series[3] [66]. Therefore, the $a(2\ell)$ coefficients can be regarded as the spectral coefficients of $Z_p(w, k')$. Equation (6.17) expresses the spectrum of ZP which involves generally $\frac{p}{2}$ spectral lines. The expansion (6.16) can be generally used for the approximation of an arbitrary continuous function over a finite interval $[-1, 1]$. One possible solution to how to generate the coefficients $a(\ell)$ can be found in e.g. [67]. Another very effective and simple approach, in which we are interested, can be derived from the linear differential equation for ZP [28] resulting in backward recursion with time-varying coefficients.

Note that the symmetrical Zolotarev polynomials are orthogonal on disjoint intervals $w \subset < -1, -k' > \cup < k', 1 >$. See Appendix B in Chapter 10. This subsequently means that Zcos(ϕ) is orthogonal in the interval of $w \subset < -1, -k' > \cup < k', 1 > |_{w=cos\phi}$. The orthogonality of Zsin in the same interval is questionable; however, we omit this and consider Zsin to be almost orthogonal.

This paragraph introduces a discretization of continuous-time variables x and θ which is needed for computing ZP1S on a computer. All above defined formulas shall be used in a discrete-time manner requiring proper sampling of continuous-time variables x or θ. The discretization can be done by letting $x = iT$, where $i = 0, 1, 2, ...$ and T is the sample step for variable x. Similarly, the variable θ is discretized by letting $\theta = Ti$, where $i = 0, 1, 2, ...$ From this point forward the discussion will be supposing that all schemes of ZP1S are discrete-time functions. Let us remember that when a proper sample step is used then the behavior of a discrete-time method is close to a behavior of the original continuous-time one. We use sample step approximately $T = 1/10^4$ for interval $[-1, 1]$ or $[0, \pi]$.

6.3.1 Methods Of ZP1S Generation

The goal of this section is to explore and compare selected methods for computation of Symmetrical Zolotarev Polynomials of the first kind ZP1S and its spectrum. Such analysis is essential before approaching to symmetrical ZPs utilization in spectral analysis. In spectral analysis the degree of the ZP1S is related to the number of samples of analyzed signal segments, and it is also directly related to the order of a filter. Therefore, utilizing ZP1S in both applications requires to generate polynomials with relatively high degree, typically, degree of hundreds. There are two typical tasks in computing ZP: one is the computation of actual ZP, while the ZP spectral coefficients computation. No method had been able to generate the spectrum of polynomials satisfying high degree [31], until the recursive algorithm was developed [28]. Nevertheless, based on findings in [28], and

[2]Since the ZP1S is even symmetrical function only even coefficients a are nonzero.

[3]In this case the Fourier cosine series.

others, there are several methods of the computation of Chebyshev polynomials or ZP or their coefficients (spectra) e.g. [67], [68], [69], [70], [71]. However, the usability boundaries of these methods and a detailed numerical comparison with each other have not yet been systematically explored. It is also unclear which degree of ZP1S or its spectrum can be achieved. In task of actual ZP1S computation we decided to use two often used methods: Chebyshev recursion [64] and power expansion with binomial coefficients [64]. For computation of ZP1S spectral coefficients we employed backward recursion [28]. An empirical technique determining if the results is not a valid polynomial was developed. Selected ZP1S computational methods in the range of ZP1S parameters are distinguished from each other using this technique. dynamic range (DR) during the computation and its stability explored as well.

Possible schemes of ZP1S computation are defined in the following text. Any ZP1S of order p can be computed using two basic approaches. Firstly, direct computation in "time" domain: by using power expansion with binomial coefficients (6.4a) or by implementing the forward recursion (6.2). Both methods in "time" generate a Chebyshev polynomial of degree p along with the transformation of parameter x onto θ. The parameter x is transformed as

$$x = \frac{2\,cos^2\theta - 1 - k'^2}{1 - k'^2} \tag{6.18}$$

in terms of (6.15). Secondly, by computing polynomial in "spectral" domain: evaluating spectral coefficients a_ℓ using difference backward recursion by Vlcek [28] followed by the inverse (Fourier) cosine transform[4] yielding the "waveform" $Z_p(w, k')|_{w=cos\phi}$ (6.17). There are other possibilities of computing ZP1S, as mentioned before. For example, using the factorized form given by ZP1S zeros [28], or rather complicated methods using Remez algorithm or other approaches based on least deviation and polynomials with weights in "time" domain [69] and [68]. But we are interested in very effective recursive method [28] promising the computation of ZP spectra of high degree and in its counterpart in the "time" domain (6.2). The aim is to compare the numerical behaviour of these selected methods.

ZP1S computation in "time" domain

This subsection briefly discusses and compares the numerical behaviour of linear time variant (LTV) recursion (6.2) and the power expansion with binomial coefficients (6.4a), both used for computing a Chebyshev polynomial of degree p.

[4]For discrete-time functions by discrete time cosine transform.

Computation using expansion of $\mathbf{T_n(x)}$

This method uses binomial coefficients given by equation (6.4a) to generate Chebyshev polynomials $T_n(x)$. Due to use of binomial coefficients the computation demands rather big dynamic range [72] and then poor computational precision can be expected. In consequence only the low degrees of ZP1S can be generated using this technique.

Computation by using LTV recursion

This method of computing Chebyshev polynomials is based on using recursion (6.2) with the substitution (6.18). The discretized version of equation (6.2) can be written as

$$\begin{gathered} T_n[i] = 2x[i]T_{n-1}[i] - T_{n-2}[i], \quad n = 2, 3, \ldots, \\ i = 0, 1, \ldots, N-1. \end{gathered} \tag{6.19}$$

with the initial condition

$$T_0[i] = 1, T_1[i] = x[i], \tag{6.20}$$

where N is the number of points at which ZP1S is sampled. Parameter N is given by using sample step T and the definition scope T_0 of variable x or θ: $N = T_0/T$. In our case we use $N = 10^4$.

Recursive schemes similar to (6.2) no matter if they are time-invariant or time-varying are known to be very effective and stable when used for limited number of samples even when fixed-point arithmetics is used [66, 73, 74]. But to our knowledge, no systematic study of numerical behaviour of this type of LTV recursion has not yet been performed for the special case of computing of ZP1S of very high degree. If recursions (6.2) or (6.3) are used then the zeros of resulting Chebyshev polynomials are almost equidistantly spread in the intervals $[-1, 1]$ or $[0, \pi]$. In the latter case of $T_n(x) = cos(n\theta)$ interval between zeros is precisely equidistant. However, if the Chebyshev recursion (6.2) is applied to compute ZP1S, especially for higher values of k' or higher ZP1S degree, its zeros are pushed towards the edges of both the definition scopes $[-1, 1]$ and $[0, \pi]$. Hence, higher errors in computing ZP1S can be expected. The recursive schemes (6.2) are known to be very effective and stable when used for limited number of samples. The scheme is stable even when fixed-point arithmetics is used. Detailed numerical study of the recursive equation of this type can be found in e.g. [73].

Summary of methods computing $\mathbf{T_n(x)}$. We briefly summarize comparison of methods of $T_n(x)$ computing using either the Chebyshev recursion (6.2) or using power expansion with binomial coefficients (6.4a). The latter method is expected to has worse

numerical behavior. The evaluation of the binomial coefficients by equation (6.4b) causes severe problems due to high dynamic range. We can see in (6.4a) the values of coefficients $c_k^{(n)}$ can be up to twice greater than the values of binomial coefficients $\binom{n-k}{k}$, which results in additional increasing of dynamical range. Nevertheless, there are some modified schemes of computing binomial coefficients (6.4a) which offers better numerical performance, e.g. [75]; however, we did not implemented these schemes. Due to described reasons we favor the use of Chebyshev recursion (6.2).

Generation of ZP1S using spectral coefficients

The algorithm to compute ZP1S spectral coefficients is derived by Vlcek [28]. The algorithm for computing ZP1S is just one of a family, of which algorithms are able to generate various kinds of ZP. The algorithm for ZP1S computation is a backward recursion with time-varying coefficients, and it can be described by

$$\begin{aligned} d_1[\ell]\, a(2\ell-6) = d_2[\ell]\, a(2\ell-4) + d_3[\ell]\, a(2\ell-2) \\ + d_4[\ell]\, a(2\ell) \\ \ell = m+2, m+1, m, \ldots, 3 \end{aligned} \tag{6.21}$$

where $d_1 = m^2 - (\ell-3)^2$, $d_2 = 3(m^2-(\ell-2)^2) + (2\ell-4)(2\ell-5)k'$, and $d_3 = 3(m^2 - (\ell-1)^2) + (2\ell-2)(2\ell-1)k'$ are time-varying coefficients. The $m = \frac{p}{2}$ is half of degree p. The computational algorithm based on the formula is in Table 6.1. The result is set of spectral coefficients a_ℓ, $\ell = 1, \ldots, p$. The spectral coefficients are transformed into ZP1S using the inverse cosine series[5].

given	$m = p/2$, k'
init-	$a\ (2m) = (1-k'^2)^{-m}$, $a\ (2m+2) = 0$,
alisation	$a\ (2m+4) = 0$
body	
(*for*	$\ell = m+2 \quad to \quad 3$)
	$\left[m^2-(\ell-3)^2\right] a(2\ell-6) =$
	$-\left[3(m^2-(\ell-2)^2) + (2\ell-4)(2\ell-5)\, k'^2\right] a(2\ell-4)$
	$-\left[3(m^2-(\ell-1)^2) + (2\ell-2)(2\ell-1)\, k'^2\right] a(2\ell-2)$
	$-\left[m^2-\ell^2\right] a(2\ell)$
end)	

Table 6.1: Recursive evaluation of the coefficients $a(2\ell)$ for symmetrical Zolotarev polynomial of the first kind $Z_p(w,\kappa) = (-1)^m \sum_{\ell=0}^{m} a(2\ell) T_{2\ell}(w)$,

[5]The discrete inverse cosine transform (iDCT)

6.3.2 Evaluation of ZP1S generation methods numerical behavior

In this section we explore numerical behavior of the ZP1S computational methods described in the previous section. Firstly we show that both LTV recursion (6.2) and (6.21) are stable. Secondly, we explore a dynamic range of the methods. And thirdly, we apply empirical criterion onto the methods results.

In case of recursion stability determination we employ following criteria. The first stability criterion states: if cumulated error throughout recurrence iterations is bounded by a linear function then the recursive system is considered stable. A recurrence system has to have a limited number of iterations. This approach is based on the one described in [73]. As a second stability criterion we chose a more analytical approach. We consider each iteration of the LTV system as a LTI system. We show that for every iteration of the LTV system every particular LTI system is stable.

The empirical criterion is based on a fundamental theorem of algebra: the number of zeros of every polynomial is uniquely given by its degree. We facilitate this polynomial property by counting the number of zeros in waveform generated by the tested method. If a number of zeros differs from a given polynomial degree then the generated waveform is definitely not the desired ZP1S polynomial. This criterion is not able to validate a method, but it is capable to point at one which is definitely unusable in a subset of ZP1S parameter space.

Stability of Chebyshev LTV forward recursion

In this section we show illustrative results confirming the stability of Chebyshev LTV forward recursion (6.2). We use previously drafted stability criterion: we adopt and slightly modify the approach suggested in [73]. We evaluate cumulative sums of quantization errors of quantized recurrence. The computation using 32-bit floating-point IEEE number format is considered as "precise". We compare the computation of quantized recurrence in 32-bit fixed point arithmetics with "precise" one. For the recursion (6.2) error is defined as

$$er_n[i] = T_n[i] - \hat{T}_n[i] \qquad i = 0, 1, 2, ..., N-1, \tag{6.22}$$

where $\hat{T}_n[i]$ represents the quantized computation version, while $T_n[i]$ represents the "precise" one. The variable n is an index of recurrence iteration. The p stands for the given polynomial order and N for the number of samples taken from respective definition scope.

The cost function given by the sum of errors is estimated according to

$$J[n] = \frac{1}{n} \sum_{i=0}^{N-1} |er_n[i]|, \; n = 1, 2, \ldots, p. \tag{6.23}$$

The stability criterion is as follows: if the function $J[n]$ is bounded by a linear function then the recursion in question is stable for limited number of iterations within the finite interval $[1, p]$, where $p < \infty$.

The accumulative error $J[n]$ for Chebyshev forward recurrence for $k' = 0.1$ and degree $p = 100$ is shown in Fig. 6.7. The function $J[n]$ is bounded, that is, any linear function with a properly chosen slope gives greater values than $J[n]$; therefore, the recursion can be considered stable. We verified this criterion to be valid up to degree 2000 with various values of k'.

Another interesting property of computed ZP1S waveform by the Chebyshev recursion method reveals the shape of cumulated error throughout θ, "time" dimension. This error which is than cumulated is given by

$$\begin{gathered} er2_n[j] = \sum_{j=0}^{j} T_n[j] - \hat{T}_n[j] \qquad j = 0, 1, 2, ..., N-1, \\ n = 1, 2, \ldots, p. \end{gathered} \tag{6.24}$$

The cumulative sum of error between "precise" computing $T_n[i]$ and quantized computing $\hat{T}_n[i]$ is shown in Fig. 6.6 for different polynomial degree within the interval $[3, 100]$. One can see that the error rapidly grows at the centre of definition scope, where the main lobe of ZP1S is placed. The error at the centre of definition scope gets bigger as polynomial degrees or values of k' increases. For higher polynomial degrees are errors the bigger as can be seen in Fig. 6.6 when we examine curves from bottom to up. This error increase is the consequence of the central lobe maximum value and of ZP1S zeros pushing towards the edges of the definition scope. For higher polynomial degree and constant elliptical modulus k' the main lobe of ZP1S is higher and wider pushing zeros more to the ends of definition scope as can be seen in Fig. 6.5a and 6.5c.

Stability of LTV backward recursion

The backward LTV recursion is given by (6.21) and Tab. 6.1. To analyze its stability we employ the first of described stability criteria. For recursion (6.21) we use the error of spectral coefficients given by

$$err_n[\ell] = a[\ell] - \hat{a}[\ell] \qquad \ell = 3, 4, ..., p+2, \tag{6.25}$$

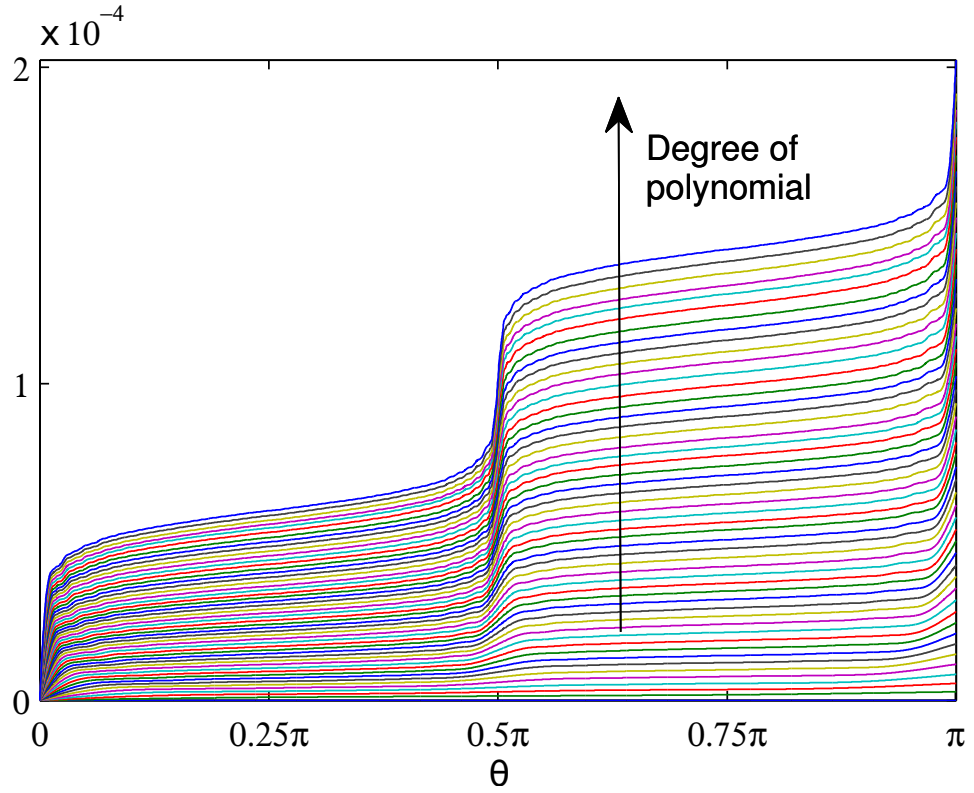

Figure 6.6: The cumulative error between "precise" and quantized ZP1S waveform cumulated in "time" domain for $k' = 0.1$ and degrees of $p = 3, 4, \ldots, 100$.

where the $\hat{a}[\ell]$ represents the quantized version with 32-bit fixed-point arithmetics, and the $a[\ell]$ represents version using 32-bit IEEE floating point arithmetics, which is again considered as "precise". The p stands for the given polynomial degree and the n for iteration index of the recursion. The cost function is now given by the cumulative sum of errors (6.25) as

$$\tilde{J}[n] = \sum_{\ell=3}^{n+2} |err[\ell]|, \qquad n = 3, 4, \ldots, p+2, \tag{6.26}$$

The stability of backward LTV recursion (6.21) can be verified similarly to the stability of forward Chebyshev recursion (6.2). Again, if $\tilde{J}[n]$ is a bounded (or linear) function of the index iteration n then the algorithm stability is ensured for limited number of iterations within the finite interval $[3, p+2]$, where $p < \infty$. The shape of accumulated error $\tilde{J}[n]$ (6.26) is shown in Fig. 6.8. This function is clearly bounded and has a similar shape as function $J[l]$ in previous Fig. 6.7. The stability was experimentally proved for different polynomial degrees within the interval $[10, 2000]$. Furthermore, one can see that the recursion (6.21) gives less maximum of accumulated error than the Chebyshev forward recursion (6.2): compare values 6×10^{-7} with 4×10^{-6}. Also the slope of function $J[l]$ at the beginning and at the end is greater than the slope of function $\tilde{J}[l]$. Thus, it can be concluded, the backward recursion (6.21) is more robust with respect to stability and

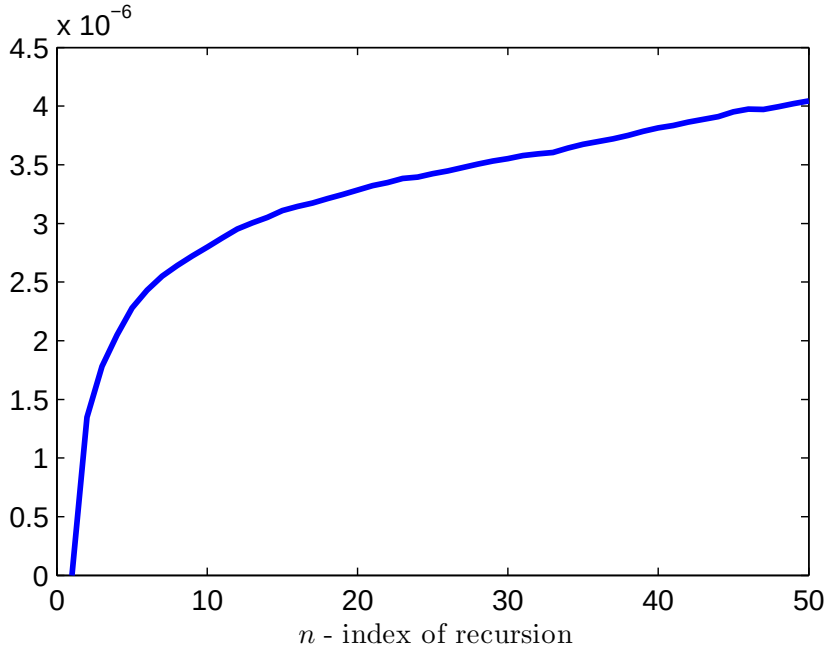

Figure 6.7: The cumulative error (6.23) comparing the quantized ZP1S computation using Chebyshev forward recursion (6.2) with the "precise" computation version; for $k' = 0.1$ and degree $p = 50$.

gives more precise results than the forward Chebyshev recursion (6.2). It is interesting to note that the stability of recursion improves with increasing number of iteration indexes n. This is illustrated by decreasing the slope (or "saturation") of $\tilde{J}[n]$ with increasing iteration index n. It can be concluded that recursion (6.1) is stable. Note that the cumulative error of the backward recursion increases as the polynomial degree increases in linear, not exponential, rate.

The second stability criterion examination follows. The analysis of this type of recursion can be performed using a state-space equation and transition matrix (e.q. [74]). The dependency of coefficients $d[\ell]$ on both $m = \frac{p}{2}$ and ℓ parameters is nonlinear. The dynamical ranges corresponding to time-varying coefficients $d[\ell]$ are significantly different. For both these reasons we approach the LTV system as a set of LTI systems fixed for each iteration rather than to use the analysis of transition matrix behaviour. Analyzed backward LTV recursion can be interpreted as IIR filter of order 6 with time-varying coefficients. When we trace parameters of the recursion in each iteration then the stability of this recursion during the whole iteration process can be verified using pole positions given by the denominator of the transfer function. The idea behind this approach is very simple. We substitute the LTV system with a linear time-invariant one. That means for

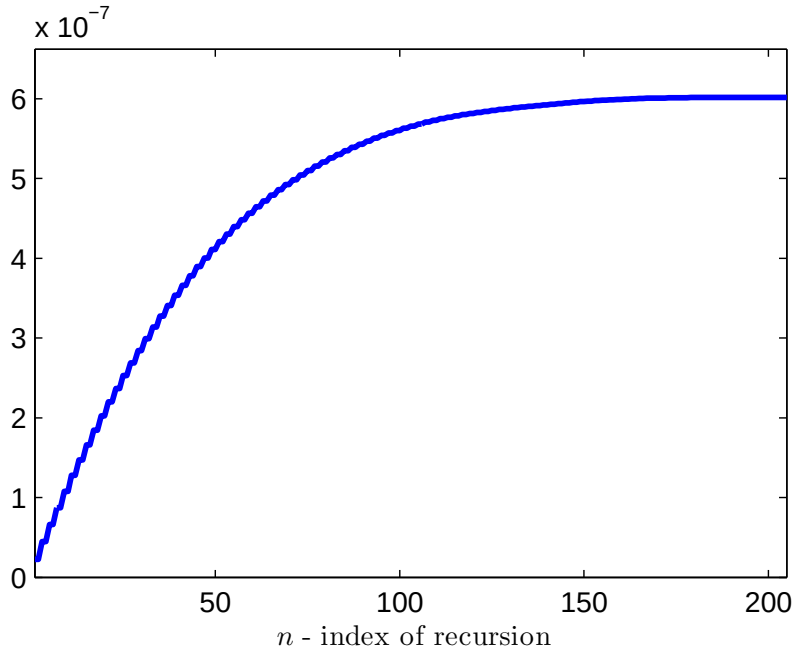

Figure 6.8: The cumulative error (6.26) comparing the quantized ZP1S computation using backward recursion (6.21) with the "precise" computation version; for $k' = 0.1$ and degree $p = 200$.

each fixed iteration instant the system is supposed to be LTI with transfer function

$$H_\ell(z) = \frac{z^6}{1 - \frac{d_2[\ell]}{d_1[\ell]} z^2 - \frac{d_3[\ell]}{d_1[\ell]} z^4 - \frac{d_4[\ell]}{d_1[\ell]} z^6}, \ \ell = 3, ..., n+2 \tag{6.27}$$

where $d_x[\ell]$ are time varying coefficients defined in (6.21). Resulting denominator of the transfer function represents a polynomial for each iteration index ℓ. Roots of this polynomial, poles of transfer function $H(z)$, are inspected and pole positions and the maxima of pole modulus are checked. This evaluation process is repeated throughout whole iteration process. One chosen result is illustrated for ZP1S parameters of $k' = 0.1$ and $p = 100$ in Fig. 6.9, which illustrates the trace of pole positions during the whole iteration process. All pole modulus during the iteration process are less then one: hence, ensuring the stability. The values of poles modulus decreases with iteration index. The best test results (the lowest values of poles modulus: the greatest distances of poles from the unit circle) are obtained for low values of k': $k' \leq 0.2$. Nevertheless, for all permissible values of $k' \subset [0, 1]$ the solution is stable. The stability was experimentally proved for different polynomial degrees within the interval $[10, 2000]$.

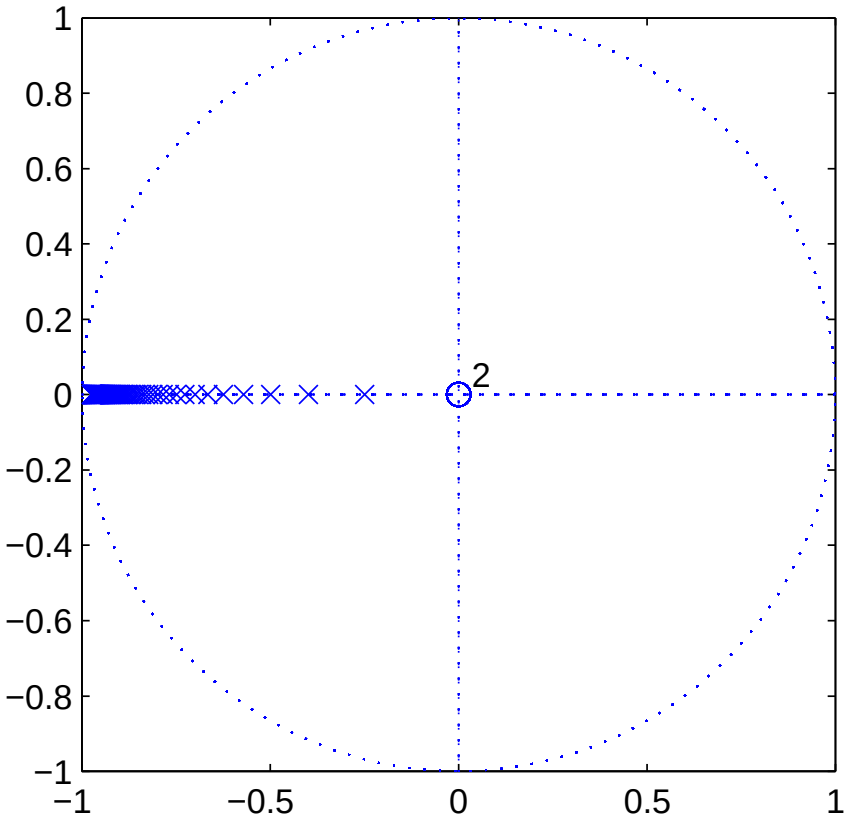

Figure 6.9: Pole positions of LTI transfer function 6.27 for all iterations of LTV backward recursion for given ZP1S parameters: $k' = 0.1$ and degree $p = 200$

Dynamic range

Dynamic range needed for all selected methods for the computing ZP1S was checked for all polynomial degrees within the interval $[10, 2000]$. The result is as expected. Dynamic range needed for binomial coefficients computing (6.4a) is much greater than for the LTV forward Chebyshev recursion (6.2) and also greater than backward LTV recursion (6.21).

For example, for degree $N = 100$ and $k' = 0.1$, the range of binomial coefficients $c_k^{(n)}$ in eq. (6.4b) values is approximately 10^{37}, while for LTV forward recursion is about 10^6 and for LTV backward recursion and its coefficients $a(2\ell)$ approximately 10^5. When we compare the dynamic range of the floating-point 32-bit IEEE number format with the range needed for the computing binomial coefficients we can see that the 32-bit floating-point number format is not sufficient for safe computing these coefficients. On the other hand dynamic ranges for both LTV recursions are comparable and much less than the dynamic range of the 32-bit floating-point number format. This is the reason why both

recursions work properly while binomial coefficients do not.

Empirical test criterion

The empirical criterion tests if a generated waveform representing ZP1S satisfies the number of zeros. The number of zeros is uniquely given by the polynomial order p. Therefore, we can find the number of zeros of computed polynomial ZP1S and compare it with the polynomial order p. If the number of found zeros differs from the given polynomial degree then the tested waveform ZP1S can not be a proper Zolotarev polynomial. The simple and robust enough way of enumerating the number of zeros is the zero crossings count (ZCC)

$$ZCC(y) = \sum_{i=0}^{N-1} \left| \frac{diff\left\{sgn(y[i])\right\}}{2} \right|, \tag{6.28}$$

where $y[i]$ is tested discrete generated polynomial. Using (6.28) we can define the zero count error (ZCE) as

$$ZCE(y,p) = -p + \sum_{i=0}^{N-1} \left| \frac{diff\left\{sgn(y[i])\right\}}{2} \right|. \tag{6.29}$$

Thus, if the ZCE computed by (6.29) is bigger than zero then the generated waveforms do not meet ZP1S properties. If the number of zeros of computed polynomial ZP1S is equal to the given polynomial order then this ZP1S might be the proper polynomial. Tests for all selected methods of ZP1S computation are using 32-bit IEEE floating number format. All waveforms are represented by $N = 10^4$ samples.

The results of ZCE evaluated for polynomials generated using power expansion with binomial coefficients (6.4a) is in Fig. 6.10. We can see that the method (6.4a) definitely fails if the polynomial degree is greater than 80. Tested method computes the waveform based on (6.15). If the waveform is computed based on (6.14) the method fails if the degree reaches ≈ 35. In case a waveform generated by LTV Chebyshev forward recursion (6.2) the results show correct number of zeros throughout all values of tested ZP1S parameter space: $k' \subset (0,1)$ and $p = 3, \cdots, 2000$.

The results of the ZCE evaluated for a waveform computed using the LTV backward recursion (6.21) followed by the iDCT are in Fig. 6.11. We can see that it should be possible to generate ZP1S of high degrees; however the interval of k' is being severely limited with increasing degree.

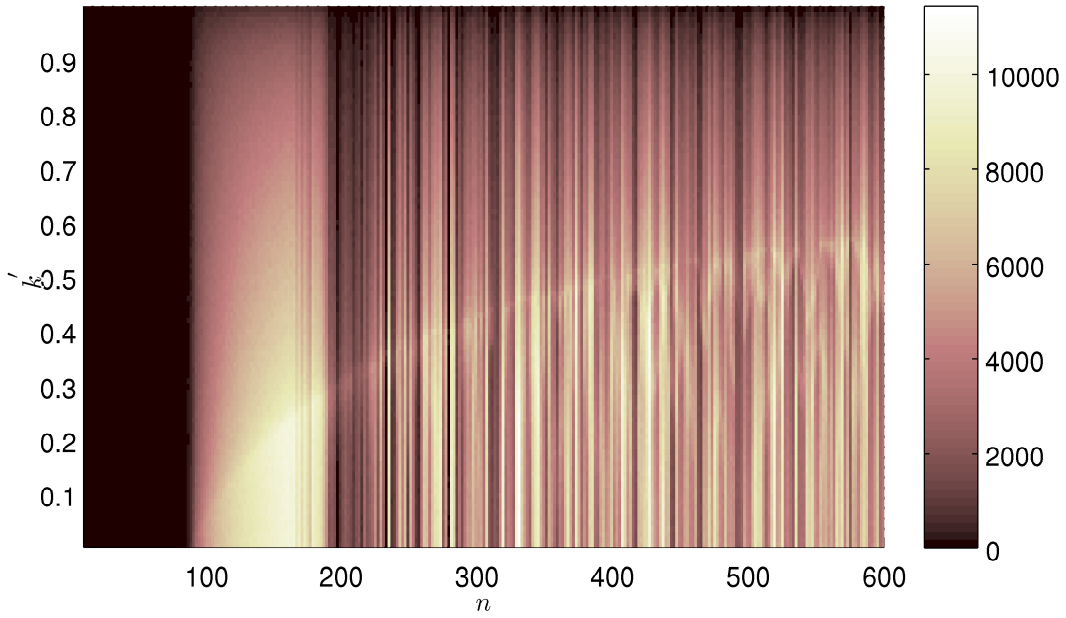

Figure 6.10: The ZCE evaluated for a waveform generated using power expansion with binomial coefficients (6.4a); non black areas denote the ZP1S parameter space where the generated waveform definitely does not meet ZP1S properties.

6.3.3 Summary

The study of selected ZP1S computation methods reveals that the one employing the Chebyshev LTV forward recursion (6.2) is the most suitable method for computing ZP1S: the empirical criterion shows the number of zeros matching the polynomial degree throughout whole parameter space $k' \subset (0, 1)$ and $p = 3, \cdots, 2000$; furthermore, the study confirms the stability of the LTV forward recursion in the same ZP1S parameter space.

In case of method using the LTV backward recursion followed by the iDCT the empirical criterion shows much worse performance, compared with forward recursion. However, the analysis of stability shows the LTV backward recursion more stable than the forward one. This seemingly contradicts, but it can be explained as follows. Both the LTV backward recursion and the iDCT are not free of the error propagation caused by quantization used in the numerical computation of ZP1S on a digital system. The problem is, we are unable to separate errors of the LTV backward recursion from errors caused by iDCT. Thus, one can expect that this method has worse results than direct computing ZP1S by forward LTV recursion (6.2). Since the LTV backward recursion is stable, even more stable than forward, it is obvious that the iDCT introduces greater errors during the computation compared with the LTV backward recursion. The iDCT errors are the result of the accumulation of cosines weighed by the spectral coefficients $a(2\ell)$ in (6.17). More detailed analysis of iDCT errors is out of the scope of this paper; however, it could prove

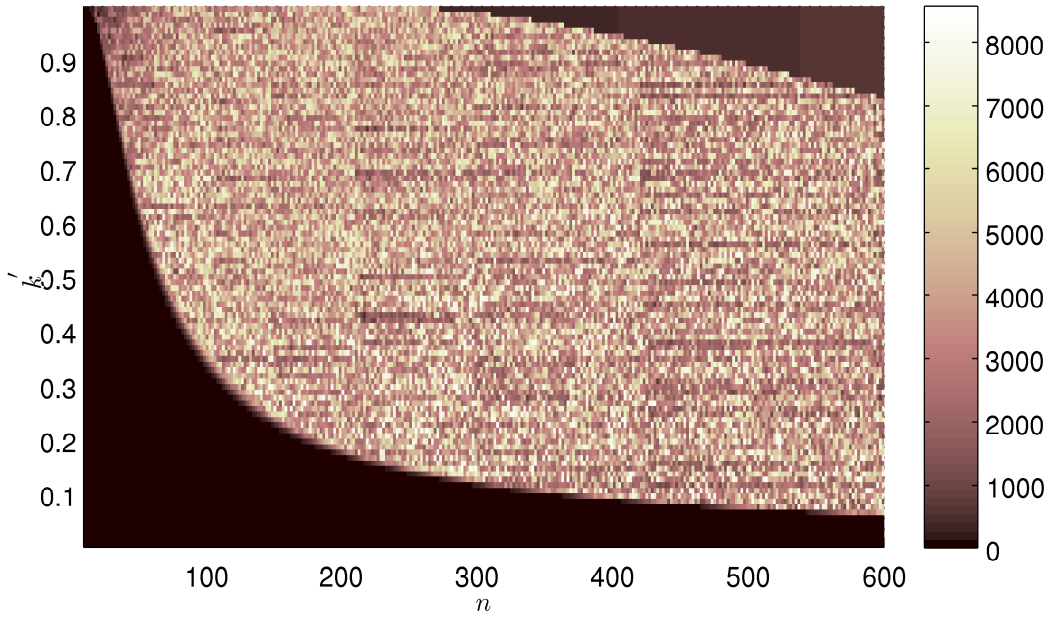

Figure 6.11: The ZCE evaluated for a waveform generated using the LTV backward recursion followed by the iDCT; non black areas denote the ZP1S parameter space where the generated waveform definitely does not meet ZP1S properties.

interesting.

In the case of employing the ZP for design of FIR filters we have shown that the methods based on backward recursion are stable and capable of generate a filter coefficients of high orders up to thousands. However, corresponding filter frequency response, which is bounded with a filter coefficients by inverse Fourier series, might be problematic in some cases. Therefore, it seems to be advisable to use the LTV forward Chebyshev type of recursion to generate a filter frequency response.

We intend to focus future research on errors of iDCT, and generally on reducing errors of latter methods for computing ZP1S.

Numerical study of computing symmetrical Zolotarev polynomials of the first kind shows that both recursions, the forward recursion for direct computing ZP1S and the backward recursion for computing spectrum of ZP1S, are stable. Method employing forward LTV Chebyshev recursion is the one most suitable one for computing the polynomial. For computing spectrum of the polynomial the Vlcek backward recursion has the best performance with respect to errors. This study also reveals that the method of computing ZP1S by backward recursion followed by iDCT has much worse numerical behavior than the one using forward recursion.

Chapter 7

Spectral Analysis using Zolotarev Polynomials

History of Zolotarev polynomials (ZP) usage for spectral analysis has begun with Radim Špetík's definition of discrete Zolotarev Transform (DZT) in his dissertation thesis [35]. However, the DZT coefficients were never evaluated directly in the time domain. Radim Špetík developed an alternative method working in the spectral domain, the ADZT. As a consequence, all conclusions regarding the DZT spectrum properties, in his thesis, are based on the ADZT resulting spectrum. An extensive study of ADZT features was conducted in Václav Turoň's dissertation thesis. However, uncertainty arises whether the described properties of the ADZT are truly DZT features or rather artifacts produced by the ADZT non-linear algorithm. The ADZT uses approximated polynomials, due to the complexity of ZPs generation. The basis optimization is conducted in the spectral domain to accelerate computation thanks to the FFT computational efficiency, see chapter 4 for computational complexity analysis. This approach is theoretically sound; however, the algorithm performs hard decisions based on the periodogram DFT spectrum's phase and amplitude. The DFT periodogram spectrum stochastic properties are quite complex to analyze mathematically [1]; moreover, the hard decisions performed by the algorithm make the theoretical analysis even less feasible. It is not clear whether, in combination with the used approximated symmetrical ZPs, the ADZT produces artifacts in the resulting spectrum. This is the main drawback preventing from wider usage of the ADZT.

We need to make certain about the DZT spectrum properties, and consequently approving or disapproving the ADZT. The next logical step is to perform DZT spectrum evaluation in the time domain using actual symmetrical ZPs. It is much more feasible to link features of the resulting spectrum to the basis properties in the time domain. Firstly, the parameters of the symmetrical ZPs are directly observable in the polynomial waveform. And, secondly, symmetrical ZPs have only a single parameter, the modulus

of elliptical functions k', related to the time selectivity feature of the polynomials, see Section 6.2. Unlike the approximated ZPs which have two parameters, the bandwidth m and non-stationary index k, see Section 4.1.

The ADZT significant properties are stated in the following Section 7.1. The DZT definition along with its spectrum coefficients evaluation are in Section 7.2. A novel method of symmetrical ZPs utilization for spectral analysis is proposed in Section 7.3. The results of the novel method are compared with the ADZT in Section 7.4.

7.1 ADZT Spectrum Significant Properties

The ADZT spectrum properties and behavior of the algorithm in general is described in [36] in detail. Here, only the most significant ADZT properties are mentioned. The ones the most questionable with respect to the ADZT usage. The analysis of proposed spectrum evaluation in time domain focuses on these particular properties.

One of the most noticeable ADZT short-time spectrum features is the intermittent spectrum of stationary signals. A model example is a sum of two real harmonic components of different frequencies, the same amplitudes, and arbitrary phases, see Figure 7.1a. The STADZT spectrum of the analyzed signal is in Figure 7.1b. The energy corresponding to the component with lower frequency is continuous in time, almost constant. However, the second component's energy distribution in time is not constant, even though the component is stationary. One can observe that the energy distribution of the second component is correlated to the analyzed signal envelope. The sum of two harmonic components of different frequencies forms an envelope with the beat frequency. The spectrum of the second component intermits at time instances where the beat frequency envelope crosses zero, see Figure 7.1c illustrating this effect. This behavior can be interpreted as imposed local signal energy distribution properties on the global ones. The global signal energy properties are related to the signal long-term integral properties, interval within the signal can be considered stationary. The local signal energy properties are related to the signal envelope. On the first hand, non-stationary transforms in their essence address the trade-off between the local and global signal energy properties. Thus the behavior is expected from that perceptive. For example, the Hilbert Huang transform exhibits similar behavior, which is shown in [35]. On the other hand, there is no direct control of how distinctive this feature is. One representation of a successful attempt is the ADZT modification for damped harmonic signals, see Section 5.2.1. Furthermore, the spectral lines at the positions of envelope absolute value minimums are abruptly removed, which is a consequence of the hard decisions within the algorithm. In the case of a more complex analyzed signal, of which composition is less clear and with a possibility of noise presence,

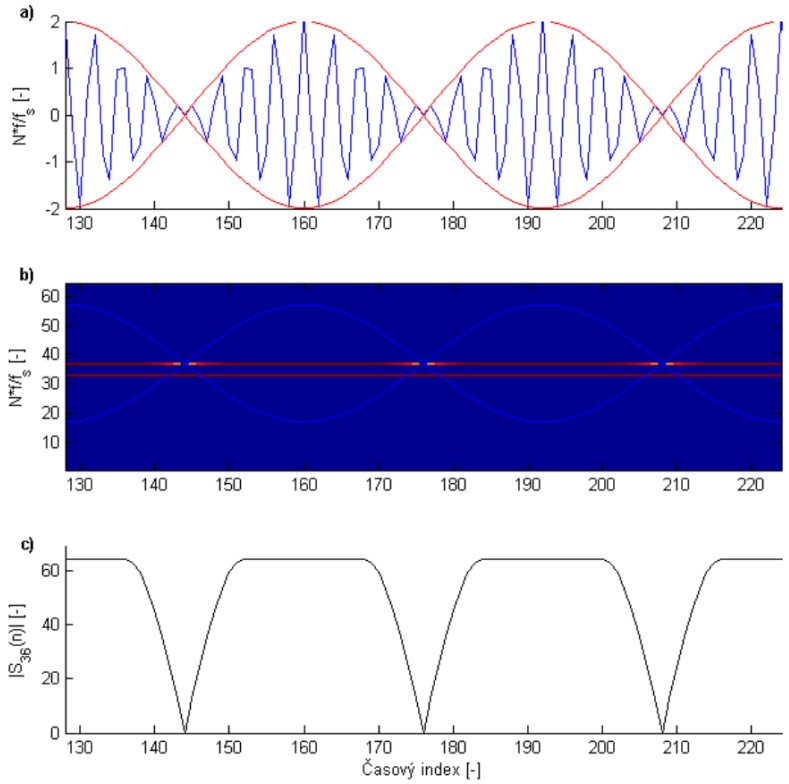

Figure 7.1: An illustration of STADZT spectrum behavior with respect to analyzed signal envelope; addition of two real harmonic components with unit amplitude, frequencies ${}_f1 = 32f_s/N$ and $f_2 = 36f_s/N$ with depicted signal envelope (first), STADZT zologram of the analyzed signal (second), and absolute value of the second component's spectral coefficient (third). Taken over from [36] with the author's approval.

the resulting spectrum is hard to interpret.

This behavior impeded further reasearch in field of signal coding using the ADZT, as proposed in [55], or rather its modification Approximated discrete Zolotarev cosine transform (ADZCT) [76].

7.2 Discrete Zolotarev Transform

This section briefly defines the Discrete Zolotarev Transform (DZT) for the purpose of explaining its nature, and to allow to make further assumptions and conclusions. Radim Špetík's dissertation thesis [35] contains detailed definition along with proof of its bi-orthogonal property.

The DZT employs a family of symmetrical Zolotarev polynomials as its basis. The Zolotarev polynomials can be expressed as a linear combination of Chebyshev polynomials with a certain set of coefficients, see Section 6.2. Analogically, the DZT spectrum can be

expressed as a linear combination of the DFT spectrum, which can be written as

$$\mathbf{S_z} = \mathbf{ZWs}, \tag{7.1}$$

where $\mathbf{s}$ is analyzed signal, $\mathbf{W}$ is the DFT basis composed from $\exp(2\pi\mu nT)$, $\mu \in \langle 0, N-1\rangle, n \in \langle 0, N-1\rangle$ and $\mathbf{Z}$ matrix contains the coefficients linking the DZT basis to the DFT basis as $\mathbf{W_Z} = \mathbf{ZW}$. Thus the DZT spectrum can be expressed using the DFT spectrum as

$$\mathbf{S_z} = \mathbf{ZS}, \tag{7.2}$$

where $\mathbf{S}$ is the DFT spectrum, $\mathbf{S} = \mathbf{Ws}$.

Zolotarev Series

The Zolotarev series [35, 41] expansion can defined analogically to trigonometric series expansion.

$$W_\ell(t, k_r, k_i) = \mathrm{Zexp}(\ell, i\omega t, k_r, k_i) = \mathrm{Zcos}(\ell, \omega t, k_r) + i\,\mathrm{Zsin}(\ell, \omega t, k_i), \tag{7.3}$$

where $\omega = 2\pi$ for $0 \leq t \leq 1$, ℓ is the degree of ZP and k' is modulus of elliptical functions. The expression can be simplified with parameters k_r and k_i in mind as

$$W_\ell(t, k_r, k_i) = \mathrm{Zexp}(\ell, i\omega t) = \mathrm{Zcos}(\ell, \omega t) + i\,\mathrm{Zsin}(\ell, \omega t) \tag{7.4}$$

Note that Zexp of a higher degree cannot be obtained from a lower degree function be scaling.

The Zexp must be normalized to exhibit normal properties as

$$\gamma_\ell^2 \left\langle \mathrm{Zexp}'(\ell, i2\pi t)\,,\, \mathrm{Zexp}'(\ell, i2\pi t) \right\rangle = 1, \tag{7.5}$$

where Zexp' is normalized basis, ℓ is the degree of ZP and γ is normalization coefficient. Since the ratio between the real and imaginary part of the Zexp generally vary; it is reasonable to scale the real and imaginary parts independently. While having in mind

$$\left\langle \cos(2\pi kt)\,,\, \sin(2\pi lt) \right\rangle \equiv 0, \quad \forall k, l \subset \mathcal{Z}, \tag{7.6}$$

and subsequently

$$\left\langle \mathrm{Zcos}(k, 2\pi t)\,,\, \mathrm{Zsin}(l, 2\pi t) \right\rangle \equiv 0, \quad \forall k, l \subset \mathcal{Z}, \tag{7.7}$$

yielding

$$\gamma_{r,\ell}^2 \langle \, \mathrm{Zcos}(\ell, 2\pi t) \, , \, \mathrm{Zcos}(\ell, 2\pi t) \, \rangle = \frac{1}{2}, \tag{7.8}$$

$$\gamma_{i,\ell}^2 \langle \, \mathrm{Zsin}(\ell, 2\pi t) \, , \, \mathrm{Zsin}(\ell, 2\pi t) \, \rangle = \frac{1}{2}. \tag{7.9}$$

The normalized Zolotarev series denotes as

$$\mathrm{Zexp}'(m, i2\pi t) = \frac{1}{\gamma_{r,\ell}} \mathrm{Zcos}(\ell, 2\pi t) \; + \; i\frac{1}{\gamma_{i,\ell}} \mathrm{Zsin}(\ell, 2\pi t), \tag{7.10}$$

where

$$\mathrm{Zcos}'(\ell, 2\pi t) = \frac{1}{\gamma_{r,\ell}} \mathrm{Zcos}(\ell, 2\pi t), \tag{7.11}$$

and

$$\mathrm{Zsin}'(\ell, 2\pi t) = \frac{1}{\gamma_{i,\ell}} \mathrm{Zsin}(\ell, 2\pi t). \tag{7.12}$$

The normalization constants can be computed as

$$\gamma_{r,\ell} = \frac{1}{\sqrt{2}} \frac{1}{\sqrt{\langle \, \mathrm{Zcos}(\ell, 2\pi t) \, , \, \mathrm{Zcos}(\ell, 2\pi t) \, \rangle}}, \tag{7.13}$$

and

$$\gamma_{i,\ell} = \frac{1}{\sqrt{2}} \frac{1}{\sqrt{\langle \, \mathrm{Zsin}(\ell, 2\pi t) \, , \, \mathrm{Zsin}(\ell, 2\pi t) \, \rangle}}. \tag{7.14}$$

Discrete Zolotarev Transform Definition

The DZT basis can be defined based on the Zolotarev series as

$$Z_N^{\ell,n} = \frac{1}{\sqrt{N}} \mathrm{Zexp}\left(\ell, \frac{i2\pi n}{N}\right), \quad \ell, n = 0 \ldots N-1, \tag{7.15}$$

where ℓ is the degree of ZP, n is the time index and N is the number of samples of the basis. Consequently, the basis is normalized according to as

$$Z_N^{'\ell,n} = \frac{1}{\sqrt{N}} \mathrm{Zexp}'\left(\ell, \frac{i2\pi n}{N}\right), \quad \ell, n = 0 \ldots N-1, \tag{7.16}$$

where Zexp' is the normalized basis according to (7.10); thus complying with (7.5).

Assuming an N-point discrete signal $s[n],\ n = 0 \ldots N-1$, DZT spectrum of the signal can be written as

$$S_Z[\ell] = \left\langle Z_N^{\ell,n}, s[n] \right\rangle, \quad \ell, n = 0 \ldots N-1, \tag{7.17}$$

and assuming the normalization applied as

$$S'_Z[\ell] = \left\langle Z'^{\ell,n}_N, s[n] \right\rangle, \quad \ell, n = 0 \dots N-1. \tag{7.18}$$

7.2.1 Evaluation of Coefficients

DZT spectrum is defined as a set of coefficients given by the scalar product of Zolotarev basis with analyzed signal (7.17). This approach is in direct analogy with the DFT. However, the DZT spectrum direct coefficient evaluation was not yet archived.

Initial efforts as part of this work to generate the spectral coefficients of DZT, DZT spectrum, according to (7.17) were unsuccessful and rather discouraging. The result of the scalar product (7.17) increases rapidly into astronomical values, while the degree ℓ is being incremented and k' is constant. The result is virtually the same no matter the information carried by an analyzed signal. The heart of this problem lies in the energy of the Zexp. Let's say we want to compute the DZT spectrum of the length of $N = 512$. We choose reasonable $k' = 0.01$, which results in $E\{\text{Zexp}(\ell = 12) = X\}$ giving us the selectivity of X; however, while ℓ rises to 512, $E\{\text{Zexp}(\ell = 12) >> X\}$. The enormous energy of Zexp at higher degrees results in very high DR. Such DR results in DZT spectrum with virtually no information on an analyzed signal. A possible way to overcome the DR problem is to normalize the basis, according to (7.10). The DZT spectrum can be computed according to (7.18). But, the results are still not satisfying. The normalization suppresses the stationary part of the signal still resulting in a DZT spectrum with no legibility either.

To evaluate the coefficients of analyzed signal projected on the transformation basis, DZT spectrum or DZT spectrum, knowledge of approximation of signal using the Zolotarev series is desirable. A signal approximation would lead to coefficients evaluation. Nonetheless, such an approximation is yet not known. The main reason is that the Zolotarev polynomials are mathematically complex and not yet fully explored.

An alternative approach to evaluate the DZT spectrum, proposed in [41]. It resides in minimizing the DZT spectrum. This approach led to the ADZT development. The ADZT [35, 36], see Section 4, minimizes the DZT spectrum energy, working in the spectral domain rather than the time domain. The algorithm is capable of zeroing the DZT spectrum's spectral lines of higher degrees where the energy of the basis exceeds reasonable DR.

DZT spectrum minimization approach application in the time domain according to the scalar product of analyzed signal and the normalized basis as (7.18) is possible by selecting optimal modulus of elliptical functions k' of the Zexp for each spectral index ℓ such as it minimizes the spectrum. Such experiments were performed and shown minor improvement in the amount of signal information contained in DZT spectrum, compared

to the direct result of the scalar product (7.18). Nevertheless, a set of selected moduli of elliptical functions k' does not appear to carry much of analyzed signal information. It is rather dominated by the basis of non-stationary part energy similar to the previous attempts. This method has not proven to be profitable either.

7.3 Proposed Novel Approach

This section introduces an alternative approach to spectral coefficient evaluation using symmetrical ZPs, an alternative to the DZT. For the reason of lack of signal approximation by the Zolotarev series, the approach is ad hoc.

The ad hoc approach is based on the following reasoning.

- Firstly, let define the assumption of that the method shall exhibit DFT spectrum properties global properties. Such that a stationary signal result is similar to the DFT spectrum of analyzed signal.
- Secondly, let the method reflect both the global and local spectral properties of the analyzed signal. The global signal energy properties are related to the signal long-term integral properties, interval within the signal can be considered stationary. The local signal energy properties are related to the signal envelope. This reasoning is also introduced in Section 7.1.
- Thirdly, the amount of the local analyzed signal property, so-called local selectivity K, is given by the scalar product of analyzed signal and a selective basis function closely related to the symmetrical ZPs.
- Fourthly, the local selectivity is imposed on the global properties by multiplication by it. Thus, assuming the global analyzed signal spectral properties are represented in the DFT spectrum, then the DFT spectrum is multiplied by the local selectivity value, which is the result of the scalar product.

Now, let illustrate the principle on a example. Assume an analyzed triangular signal with a different offset from the center of the analyzed window. The signal with energy centroid in the center is depicted in Figure 7.2a, with right of the center in Figure 7.2c, and with left of the center in Figure 7.2e. An illustration of the selective basis waveform is depicted as a dashed line in the figure. Note that for all analyzed signal shifts the resulting DFT spectrum is equal in its absolute value. Figure 7.2b, 7.2d, and 7.2f depict DFT spectrums for respective analyzed signal shifts; the blue lines denote the DFT spectrum amplitudes.

Consider that the DFT spectrum amplitude values are multiplied by the scalar product of the analyzed signal and the selective basis, the local selectivity K. In the first case,

where the energy centroid of the analyzed signal is at the center, the resulting spectrum is equal to the DFT spectrum. In the second case, where the energy centroid of the analyzed signal is right of the center, the resulting spectrum is reduced in amplitude by $1/K$, see the red lines in the Figure 7.2d. Similarly, in the third case, see the red lines in Figure 7.2f. The local selectivity K is equal for both cases since the selective basis is even symmetric around the center. The result in the second and third cases reflects that the local analyzed signal spectral properties are not aligned with the selective basis. Now assume that the resulting spectrum is composed similarly to the short-time DFT, using the windowing process. The output will exhibit additional resolution in time compared to the STDFT. The result is actually similar to the STADZT.

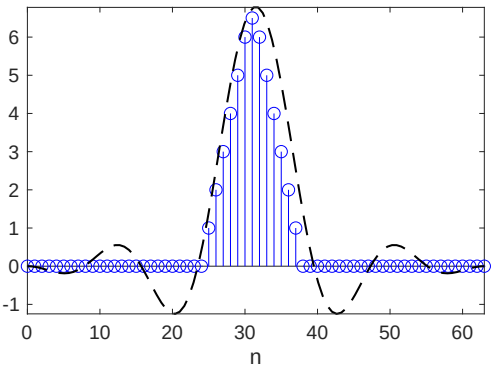

(a) Signal w1; energy at the window center depicted as samples; selective basis waveform is depicted by the dashed line.

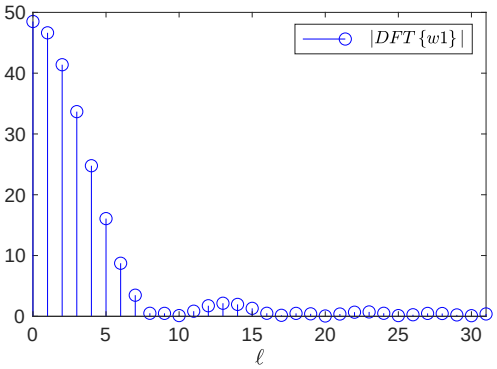

(b) Left half of the DFT spectrum of w1: $|DFT\{w1\}|$.

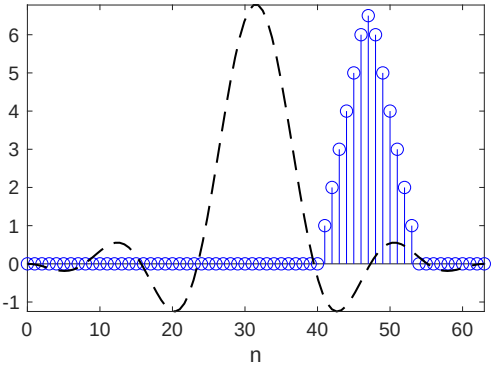

(c) Signal w2; shifted to the right of center depicted as samples; selective basis waveform is depicted by the dashed line.

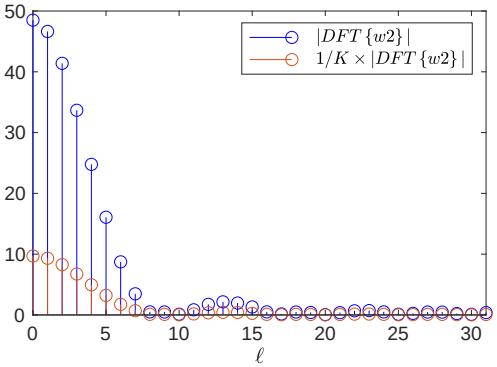

(d) Left half of the DFT spectrum of w2; red samples are the spectrum amplitudes reduced by the factor of $1/K$.

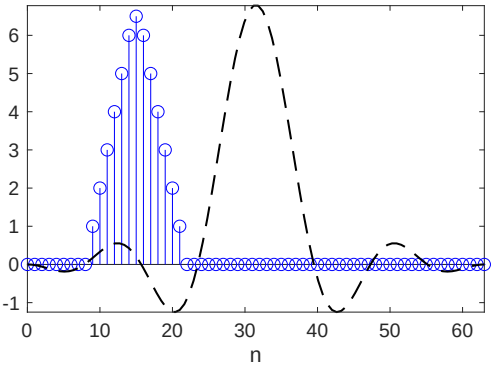

(e) Signal w3; shifted to the left of center depicted as samples; selective basis waveform is depicted by the dashed line.

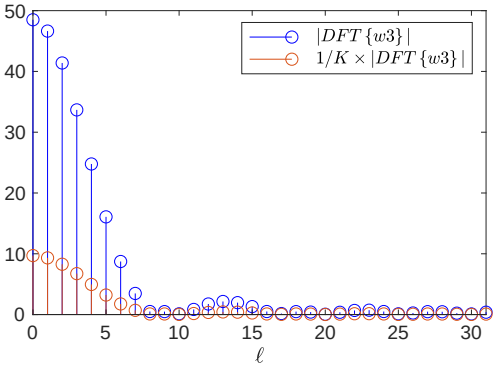

(f) Left half of the DFT spectrum of w3; red samples are the spectrum amplitudes reduced by the factor of $1/K$.

Figure 7.2: An illustration of proposed ad hoc non-stationary DFT based method principle; an example triangular signal with different signal shifts is depicted in a),c), and e). The absolute value of the DFT spectrum for each signal shift is depicted in b), d), and f), respectively, by the blue samples; the resulting spectrum with signal local spectral properties imposed is depicted by the red samples.

7.3.1 Selective Basis

The selective basis of the proposed method is composed of a non-stationary part of the Zolotarev exponential Zexp (7.3), see Section 7.2. The Zexp can be decomposed into stationary and non-stationary parts. This principle was introduced in [41]. It is related to the fundamental property of the Zexp; Zexp is a generalization of the complex trigonometric exponential, and it is additionally parametrized by the modulus of elliptical functions k'. When the $k' = 0$ the Zexp degrades to the trigonometric exponential, as shown for Zolotarev cosine and sine in Section 6.2. The decomposition to the stationary and non-stationary for Zcos is depicted in Figure 7.3d.

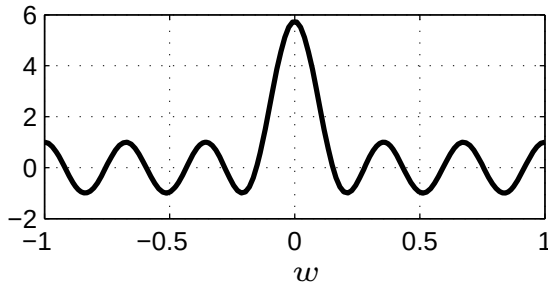

(a) Zcos waveform.

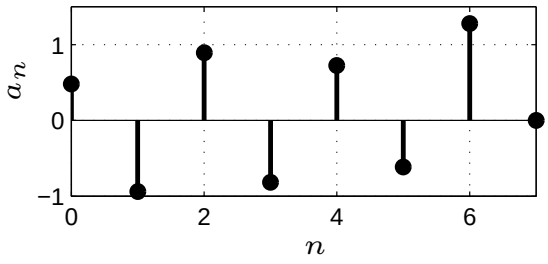

(b) Spectrum of Zcos.

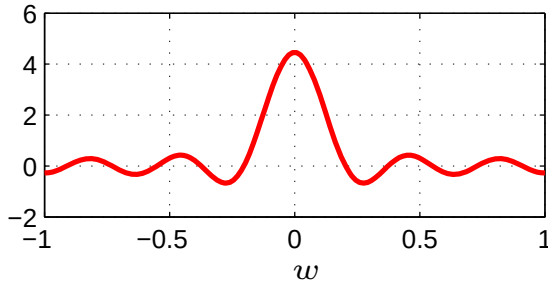

(c) Non-stationary part of Zcos.

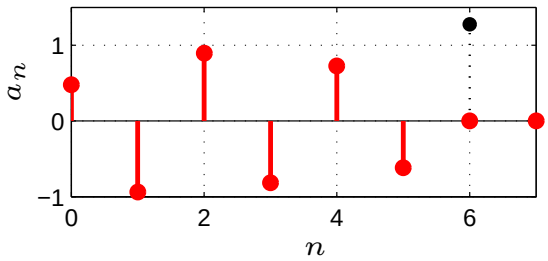

(d) The spectrum of non-stationary part of the Zcos.

Figure 7.3: Illustration of Zcos decomposition into stationary and non-stationary pars; $\mathrm{Zcos}(m, k', \phi)$; $m = 6$, $k' = 0.2$.

However, the decomposition described in [41] is not entirely correct. The article regards the stationary part as the mth coefficient of the Zexp spectrum. The non-stationary part is composed from all coefficients of with indexes $\ell \subset \{0, ..., m-1\}$, see Figure 7.3d. In this case, the non-stationary part waveform energy is not limited at the edge of the window, see Figure 7.3c. This work rather defines the decomposition to of the non-stationary part as

$$\begin{aligned} \mathcal{N}\left\{Zexp(m, k', i\phi)\right\} &= Zexp(m, k', i\phi) - Zexp(m, k', i\phi)|_{k'=0}, \\ &= Zexp(m, k', i\phi) - exp(m, i\phi). \end{aligned} \tag{7.19}$$

The stationary part holds

$$\begin{aligned} \mathcal{S}\left\{Zexp(m,k',i\phi)\right\} &= Zexp(m,k',i\phi)|_{k'=0}, \\ &= exp(m,i\phi). \end{aligned} \tag{7.20}$$

The difference between approach in [41] and the proposed one is shown in Fig. 7.4.

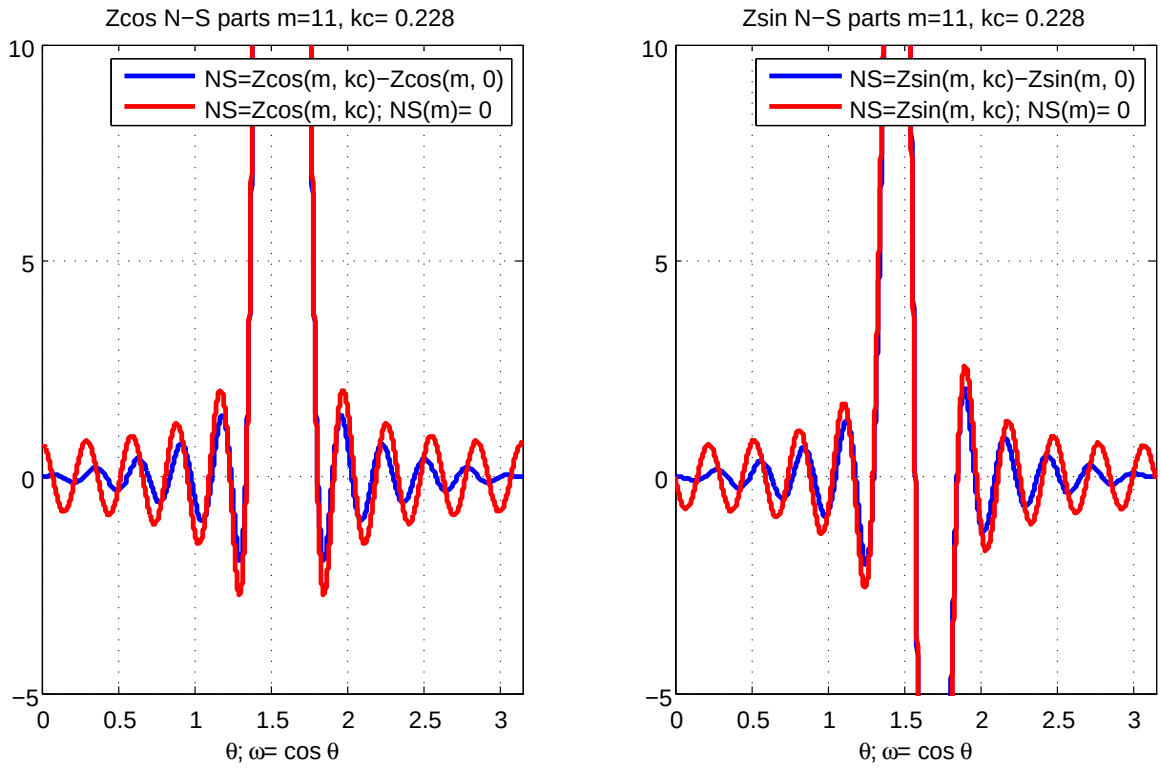

Figure 7.4: Non-stationary part of Zexp, denoted as NS in this figure legend, the non-stationary part waveform is depicted separately for the real and imaginary part of the Zexp, where the blue line denotes the proposed approach and the red line denotes the approach in [41].

Thus the selective basis denoted as $\Delta(m,k')$ for the proposed method is composed of the Zexp non-stationary part according (7.19) as

$$\Delta(m,k') = \mathcal{N}\left\{Zexp(m,k',i\phi)\right\}, \tag{7.21}$$

m is degree of the Zexp and k' is modulus of elliptical functions.

7.3.2 Definition of the Method

As outlined previously the principle of the method result evaluation is the DFT spectrum of analyzed signal multiplication of by the local selectivity K. The local selectivity K is a scalar product of the selective basis $\Delta(m,k')$ (7.21), in principle. However, the fact that the energy of symmetrical ZPs, which is mostly composed of the non-stationary part, has

large dynamic range has to be addressed. The high dynamic range is mitigated by the introduced Zexp normalization (7.10). Additionally, the analyzed signal window energy has to be normalized as well. Both normalization lead computation of the local selectivity K as a correlation coefficient between the analyzed signal window and the selective basis Δ as

$$K(\ell, k') = \frac{\langle\ \Delta(\ell, k'), s(n)\ \rangle}{\mathrm{E}\left\{\Delta(\ell, k')\right\} \mathrm{E}\left\{s(n)\right\}}, \tag{7.22}$$

where $\Delta(\ell, k')$ is the selective basis (7.21), $s(n)$ is the analyzed signal window and operator $\mathrm{E}\left\{.\right\}$ is signal energy operator. The result is then equal to the multiplication of the analyzed signal window DFT spectrum by the $K(\ell, k')$ as

$$|S''_Z(\ell)| = |\mathrm{DFT}\{s(n)\}(\ell)|\ K(\ell, k'), \quad \ell \subset \{0, ..., N-1\} \tag{7.23}$$

The spectrum is computed separately for the real and imaginary parts. This is possible for analysis of a real signal. A short proof follows. The L1-norm and L2-norm are defined by scalar product, see [77], as

$$\begin{aligned} \mathbf{x} &\subset \mathbb{C}^n, \\ ||\mathbf{x}|| &= \sqrt{\sum_{j=0}^{n-1} |x_j|^2} = \sqrt{\langle \mathbf{x}, \overline{\mathbf{x}} \rangle}, \quad \langle \mathbf{x}, \overline{\mathbf{x}} \rangle \geq 0, \\ ||\mathbf{x}||^2 &= \langle \mathbf{x}, \overline{\mathbf{x}} \rangle, \end{aligned} \tag{7.24}$$

where product polarization identity defines scalar product as

$$\begin{aligned} \mathbf{x}, \mathbf{y} &\subset \mathbb{C}^n, \\ \langle \mathbf{x}, \mathbf{y} \rangle &= \frac{1}{4} \left(||\mathbf{x} + \mathbf{y}||^2 - ||\mathbf{x} - \mathbf{y}||^2 + i||\mathbf{x} + i\mathbf{y}||^2 - i||\mathbf{x} - i\mathbf{y}||^2 \right), \\ \langle \mathbf{x}, \mathbf{y} \rangle &= \left(\sum_{j=0}^{n-1} x_j\ \overline{y_j} \right), \\ ||\mathbf{x}|| &= \sqrt{\langle \mathbf{x}, \overline{\mathbf{x}} \rangle}, \quad \langle \mathbf{x}, \overline{\mathbf{x}} \rangle \geq 0. \end{aligned} \tag{7.25}$$

The scalar product can be performed separately for the real and imaginary parts. Let's denote $\mathbf{x} = \Delta(\ell, k') \subset \mathbb{C}$ and $\mathbf{y} = s[n] \subset \mathbb{R}$, and use as arguments of polarization identity (7.25), while using (7.24). The result is confirms that consistent with the the separate evaluation of (7.23) for the real and imaginary parts if the analyzed signal is real. This separation holds for the real analyzed signal only.

7.3.3 Results

Discrete Zolotarev transform based methods are a generalization of discrete Fourier transform. Thus it is sensible to compare results with STDFT and its adaptive time-frequency modifications. However, a comparison of the ADZT results with STDFT based methods was already done comprehensively in Václav Turoň's dissertation thesis [36]. Therefore, it would be redundant as part of this work. A reader is kindly asked to refer to the [36]. The proposed method is compared only with STADZT and STDFT.

The proposed method does not perform any optimization of the selective basis; no optimal modulus of elliptical function k' is being found. Instead, the k' is a parameter of the method. The parameter k' is related to frequency bandwidth where the method provides improved time-resolution compared with the STDFT. Lower the value of the k' higher the frequency band center is. This feature is similar to, so-called, "zoom" technique, where a desired frequency band is selected by a filer bank and consequentially zoomed in.

Choosing an k' automatically for each frequency index is possible. A set of correlations of analyzed signal with a set of the selective basis of tested k', reveals a single k' value where a maximum value of the correlation exhibits. However, by choosing such k' the method's time selectivity feature is degraded. This approach requires further effort and will be studied in the future.

The examples of the method spectrum in comparison with the STDFT and STADZT are in Figure 7.5, Figure 7.6, and Figure 7.7, for different values of $k' = 0.150, 0.075$, and 0.097, respectively. The first illustrative result sets the frequency band focus at lower frequencies, where the base of the Dirac impulse frequency can be observed; the time resolution is comparable with the STADZT. The second illustrative result sets the frequency band focus at lower middle frequencies, where the base of the first mixture of harmonic components can be observed. Note that the spectrum of the harmonic components is intermittent similarly to the STADZT spectrum. The Dirac impulse spectrum is also observable with the time resolution is comparable with the STADZT. The Gauss pulse is also noticeable although the energy in its spectrum is low; that is due to the frequency-focused band center being slight of the Gauss pulse frequencies. The third illustrative result sets the frequency band focus at higher middle frequencies, where the base of the first mixture of harmonic components can be observed. Only the higher harmonic component of the second mixture can be observed due to frequency focus. Note that the spectrum of the harmonic components is intermittent similarly to the STADZT spectrum. The Dirac impulse spectrum is also observable with the time resolution is comparable with the STADZT. Figure 7.8 shows an illustrative example of an ECG signal analysis using the proposed method in comparison with the STADZT. Both methods capture spectrum of the QRS complex pulse distinctively in time. The P and T pulses are better visible in the

proposed method's spectrum compared with the STADZT spectrum. The DZT spectrum property of intermittent spectral information in time is again noticeable in the spectrum of both methods. The STDFT spectrum provides no time selectivity whatsoever for the selected frequency resolution.

The fourth subplot shows the result of (7.23). Particularly pictures shows results for synthetic and ENG signal for different chosen k'.

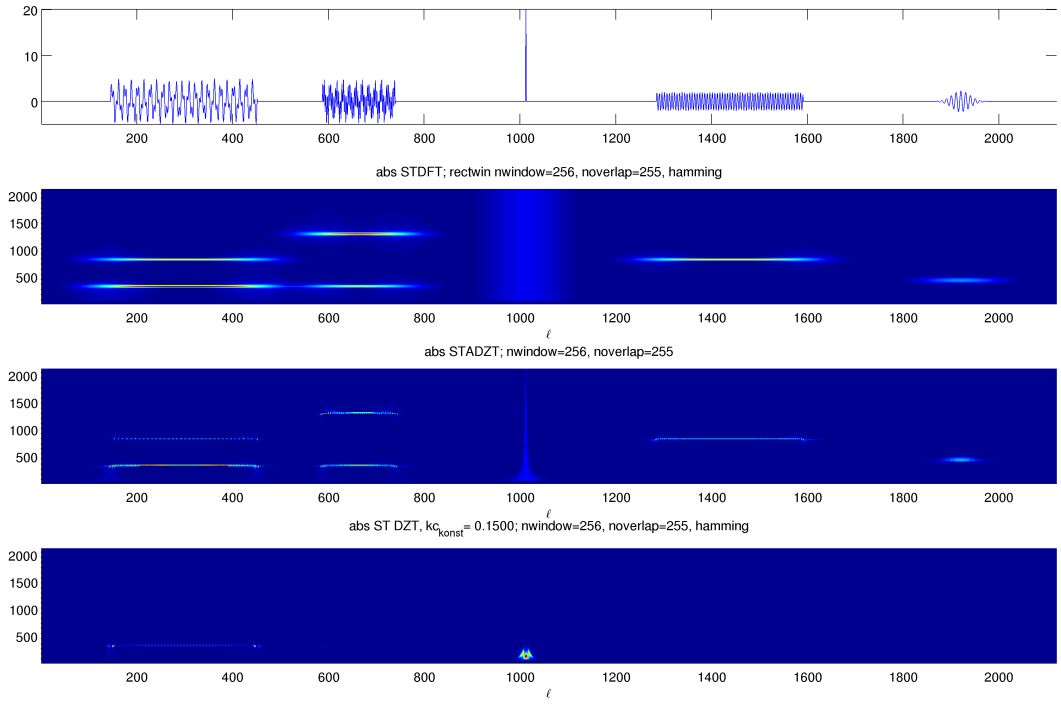

Figure 7.5: Comparison of the proposed method spectrum for synthetic signal composed of the different consecutive synthetic signals; addition of two harmonic components with different frequencies, a Dirac pulse, a single harmonic component, and the Gauss pulse. The signal waveform a), the STDFT spectrum b) the STADZT spectrum c), and the proposed method spectrum for $k' = 0.150$ d).

7.4 Comparison of the Novel Approach with ADZT

- The spectrum of both the proposed method and the STADZT are intermittent for stationary harmonic components. Thus this proves that the property is indeed the DZT, and not a property ADZT algorithm.
- The proposed method has only one parameter, the modulus of elliptical function k', so the method has one less degree of freedom compared to the ADZT.
- The proposed method, unlike the ADZT, ZOOMs in the selected frequency band, which depends on the value of the k' parameter.

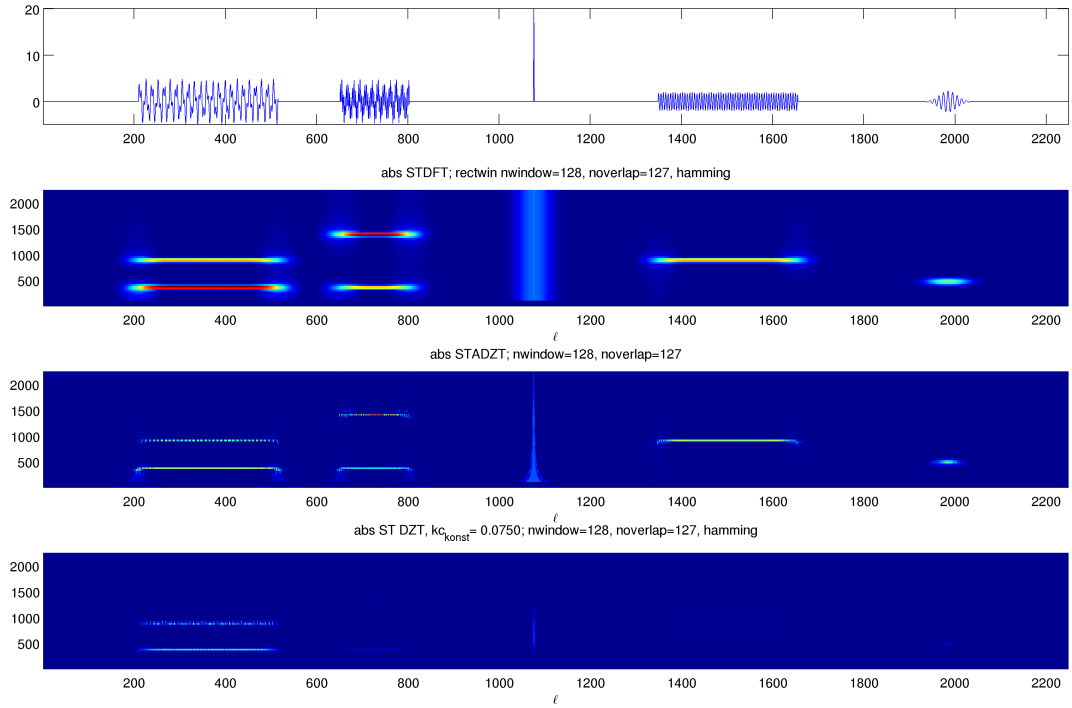

Figure 7.6: Comparison of the proposed method spectrum for synthetic signal composed of the different consecutive synthetic signals; addition of two harmonic components with different frequencies, a Dirac pulse, a single harmonic component, and the Gauss pulse. The signal waveform a), the STDFT spectrum b) the STADZT spectrum c), and the proposed method spectrum for $k' = 0.075$ d).

- The proposed method does not yet allow the setting of k' automatically based on the analyzed signal. Further effort should be dedicated to exploring this feature.

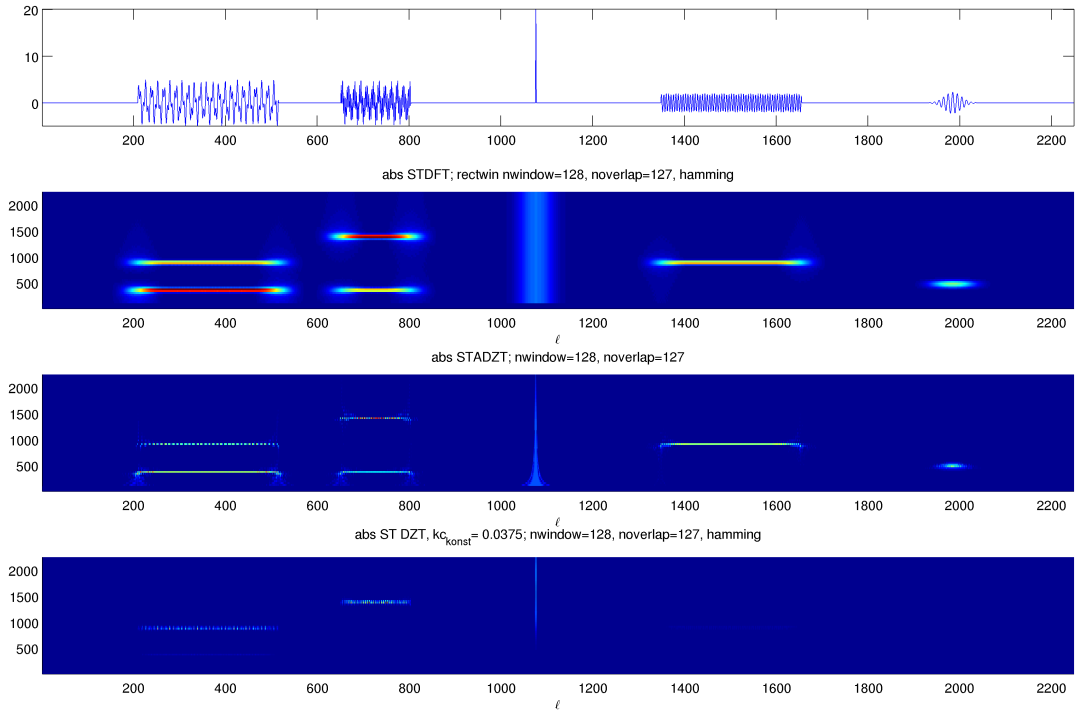

Figure 7.7: Comparison of the proposed method spectrum for synthetic signal composed of the different consecutive synthetic signals; addition of two harmonic components with different frequencies, a Dirac pulse, a single harmonic component, and the Gauss pulse. The signal waveform a), the STDFT spectrum b) the STADZT spectrum c), and the proposed method spectrum for $k' = 0.037$ d).

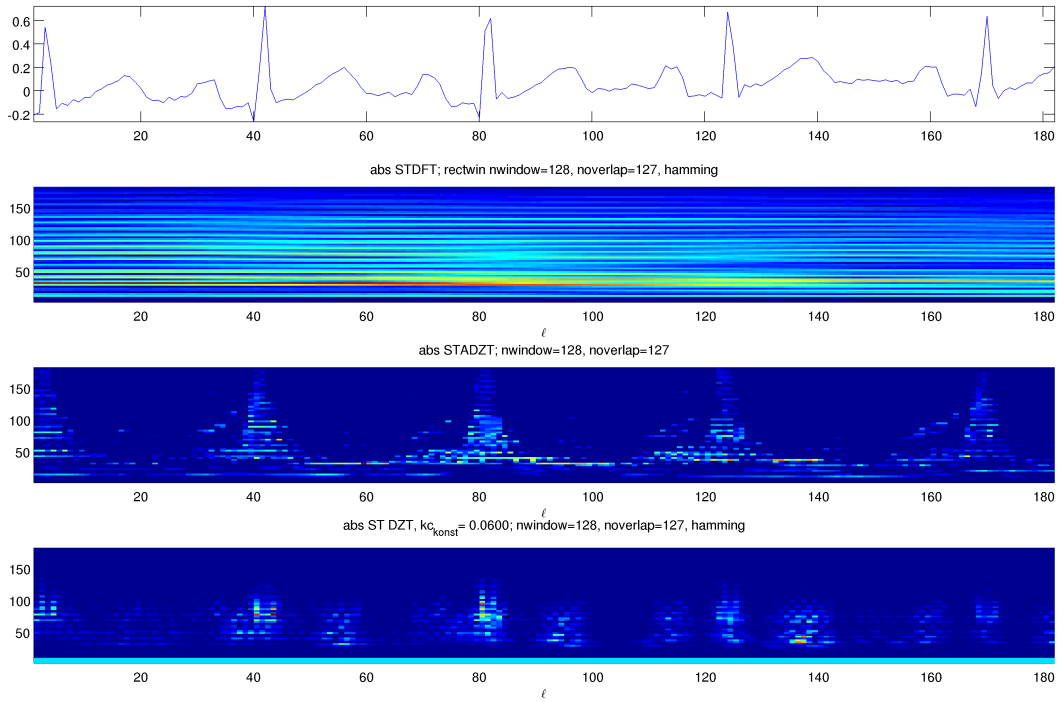

Figure 7.8: Comparison of the proposed method spectrum for a model ECG signal. The signal waveform a), the STDFT spectrum b) the STADZT spectrum c), and the proposed method spectrum for $k' = 0.150$ d).

Chapter 8

Conclusion

This thesis was focused on selected problems connected with the application of ZP to spectral analysis.

- Firstly, the implementation of DZT spectrum evaluation using the approximated symmetrical Zolotarev polynomials, known as the ADZT, was in the focus. The algorithm was studied with respect to its computation demands. The design of a more efficient algorithm software implementation, together with an embedded hardware implementation targeting the FPGA, was suggested and implemented. The embedded implementation enables ADZT computation in real-time. The findings were published in [A2].

- Secondly, the ADZT was studied with the aim to use it for transient signals analysis. A modification of the ADZT tailored for damped exponential signals analysis was described. The modification outperforms both the original ADZT and DFT, using various weighting windows, in the detection of transient signals, damped exponential signals in particular. This study was motivated by a possibility to use the ADZT for analysis of faulty rotary machinery, bearings in particular. The findings were published in [A3].

- Thirdly, the properties of symmetrical Zolotarev polynomials including orthogonality properties were described. Numerical properties of algorithms generating even Zolotarev polynomials were explored and described. It was shown that the algorithm generating the polynomials as either a waveform in the time domain or coefficients in the spectral domain is very precise and stable. Additionally, this study revealed that the method of computing Zolotarev polynomials by backward recursion followed by iDCT has much worse numerical behavior than the one using forward recursion. The findings were published in [A1].

- The novel spectral analysis method employing symmetrical Zolotarev polynomials was proposed. In contrast with the ADZT, which uses approximated polynomials and is implemented in the frequency domain, the new DZT transform is implemented in the time domain. The proposed method has only a single tuning parameter, while the ADZT performance is determined by two parameters. This property is given by the fact that the proposed method related to the DZT uses symmetrical Zolotarev polynomials, not the approximated ones. The novel transform has the feature that generates the intermittent short-time spectrum of stationary signals similar to the ADZT. This fact allows concluding that this feature is in fact the inherent property of symmetrical Zolotarev polynomials when used for spectral analysis. Even though, new results were achieved there is a number of unsolved questions regarding the use of symmetrical Zolotarev polynomials for spectral analysis. These questions were stated in the text of this thesis. The findings were partially published in the technical report [A6].

Chapter 9

Appendix A

9.1 ADZT embedded implementation on FPGA

Today's embedded systems are composed of both SW (software) and HW (hardware) components, each one has its pros and cons:

- Fully SW product solution, for instance [78], [79], is easy to develop as well as debug. The risk of a costly bug in the final products is low. Later modifications can be applied easily; software is very flexible. On the other hand, the software runtime is often unnecessarily long and requires considerable resources. Also, power consumption is often high.

- Fully HW solution is dedicated to perform specific task effectively with respect to time, area resources, and power consumption (e.g., [80], [81], [82]). However, to implement and verify such a solution is time-consuming. There is a considerable risk of a bug in the final product, and even a minor modification can result in a time consuming architecture change. A hardware solution is rather optimized but not very flexible.

SW parts of the system are suited to implement decision-like tasks where data throughput is not an issue often in higher levels of system hierarchy (e.g., control communication protocol, control blocks governing data path blocks). On the other hand, HW system parts are best in tasks where many operations with many data are required as fast as possible; data throughput is a key issue (e.g., data path blocks, MAC blocks). We used co-design methods [83, 84] to achieve a trade-off between the advantages and disadvantages of both SW and HW solutions. Our design goals were speed, simplicity, and the possibility of future minor changes.

The first step in the system level design was to draw the boundary between HW and SW part of the system. We started the system design as fully SW based on the functional

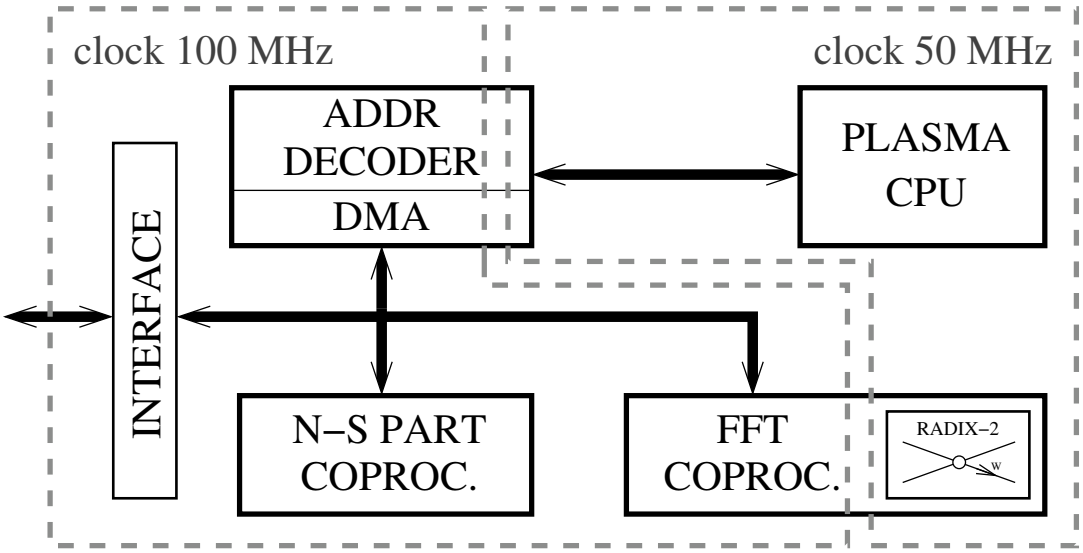

Figure 9.1: System top level architecture. Dashed lines depicts distinct clock domains.

algorithm model using a general-purpose processor; we exploited SW versatility and were able to debug the system quickly and effectively. Then we confirmed the computation bottlenecks, which were revealed by the algorithm asymptotic complexity analysis in Section 4.2. The first algorithm step, the FFT algorithm, we implemented as HW solution. The FFT algorithm is a well covered topic, see [85, 79, 81]. The second algorithm step is the most time complex one. The step is comprised of addition, multiplication, and minimum search in (4.2). Thus the step can be easily implemented by HW: addition and multiplication are common operations, and minimum search requires only one decision. The third algorithm step has linear time complexity; this is not an issue from the computational complexity standpoint. Furthermore, the step comprises of several decisions. Hence the third step is implemented by SW. Figure 4.1 depicts the algorithm steps implemented by HW with a double line border and by SW with a single line border.

The architecture of the system is outlined in Fig. 9.1. It is composed of Plasma processor [48], external address decoder, FFT coprocessor, Non-Stationary (N-S) part coprocessor, and interface. The interface unit stands for a bridge between the bus and the external world. The address decoder selects an external unit and connects its buses to the processor as well as handles simple Direct Memory Access (DMA). We favored 32 bit RISC processor Plasma [48] with MIPS I^{TM} instruction set [86]. The processor has free licence terms, free C language compiler, and it is written in VHDL. The Plasma processor has 8 kB internal memory for programs and data. The SW program, which implements the algorithm step 3 and schedules the execution of both coprocessors, size is $\approx$ 2.8 kB. The data memory is mainly occupied with pre-computed values of $K(m)$ for each m in (4.7): utilizing 4 kB. Thus the processor's internal memory size is sufficient for our needs.

The system is separated into two clock domains. The N-S part coprocessor, part of the FFT coprocessor, and the interface are clocked at 100 MHz. The Plasma processor and the radix-2 butterflies within the FFT coprocessor are clocked at 50 MHz. The address decoder serves as a bridge between the two clock domains. The main reason to introduce two clock domains is to speed up the N-S part coprocessor; thus reducing the step 2 runtime. The coprocessor accesses the FFT coprocessor memory via DMA during the execution. This requires the address decoder and the FFT coprocessor to be in the same clock domain as the N-S part coprocessor is. However, the butterflies would require additional pipelining to reach the higher clocking frequency. This is not necessary since the FFT computation speed up would not yield a significant runtime reduction of the whole system. The solution is to keep the butterflies in the slower clock region. The resynchronization between the domains is relatively simple. The faster clock domain has exactly twice the slower clock domain frequency. The two clock signals have aligned rising edges. Sufficient adaptation is to lengthen control signals leading from the faster to the slower domain to two clock cycles.

All of the system units have been written in VHDL language.

FFT Coprocessor

The hardware design methods to implement an FFT coprocessor have been described previously, see [85, 79, 81]. The FFT coprocessor is composed of a pair of radix-2 butterflies, a pair of double port RAM for each butterfly, and a dedicated address generator. Twiddle factors are stored in a pair of $2\,048 \times 32$ bit ROM; its size is 16 kB. Each butterfly uses 32×32 bit wide complex multiplier with two-stage pipelining. The unit holds complex input samples and output DFT complex spectrum in the memory pair. Real Imaginary Alternate (RIA) format [87] is used. The memory pair has total depth of $2 \times 2\,048 = 4\,096$ depth (2 represents real and imag. part, $N_{DFT} = 2\,048$); the memory size is 16 kB. The memory is accessible through the system bus, and it is used as data memory for the whole system. The unit total memory requirement is 32 kB. The unit computes one-shot DFT spectrum of length $N_{DFT} = 2\,048$ in $\approx 5\,700$ clock cycles of the slower clock domain. The FFT coprocessor has been designed as part of master's thesis [88].

Non-stationary Part Coprocessor

The N-S part coprocessor top-level schema is in Fig. 9.2. The unit realizes computation of the N-S part according to (4.6) and searches for an optimum according to (4.2) for the current ℓth spectral line. The actual computation is implemented in the N-S core block. The address generator generates addresses of DFT coefficients stored in the FFT

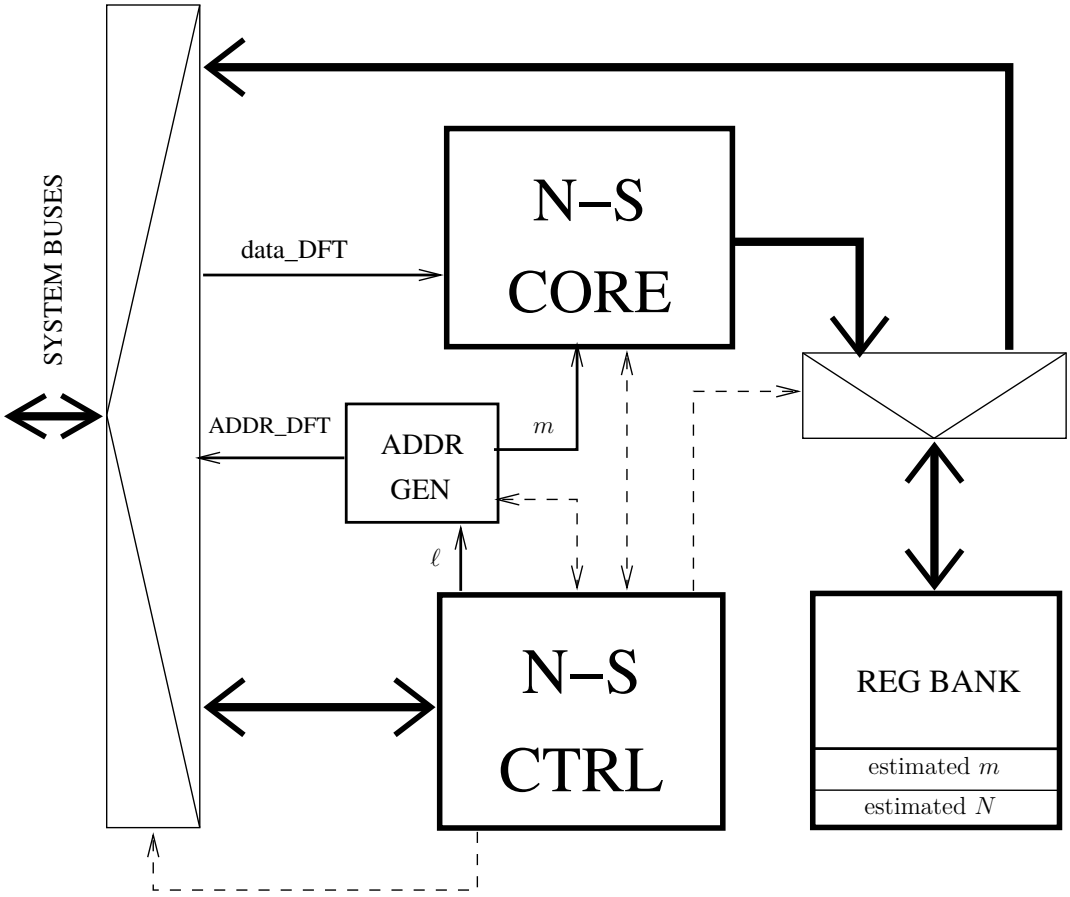

Figure 9.2: Non-stationary part coprocessor top level architecture; dashed lines denote control signals, wide lines denote buses. All buses are 32 bit wide. Clock and global asynchronous reset signals are omitted in the schema.

coprocessor as

$$S\_addr_\ell(m') = (\ell - m') \times 2 + is\_imag, \qquad m' = \{0, 1, \ldots, N-1\}\,. \tag{9.1}$$

Since the algorithm works separately for real and imaginary parts, the address is multiplied by 2 in order to select real or imaginary parts only (according to used RIA format). The real or imaginary part is computed, while the variable *is_imag* is set to 0 or 1, respectively. The address is routed through the system bus to the FFT coprocessor, which output supplies the N-S core unit with stationary part values. The unit is mounted to the system bus as its master via DMA during the unit execution. Input current spectral ℓth line and variable *is_imag* are stored in the register bank. The register bank also holds results supplied by the N-S core block, optimal bandwidth, and N-S part. The controller block controls access to the register bank and the system bus as well as schedules execution of the other blocks.

The principal schema of the N-S core block architecture is in Fig. 9.3. The MEM blocks

Algorithm step	System unit	Runtime (clock cycles)
1	FFT coproc.	≈ 5.7 k
2	N-S coproc.	≈ 539 k
3	Plasma proc.	≈ 318 k
2 & 3 simultaneously	N-S + Plasma + DMA	≈ 570 k

Table 9.1: Algorithm cumulative runtime (the algorithm steps 2 and 3 are executed N times for arbitrary ℓ) for segment length $N_{DFT} = 2\,048$; clock cycles values are given with respect to the 50 MHz clock domain.

stand for a simple synchronous memory composed of a multiplexor and a synchronous register. SIGN MUX 1, adder, and ALT SUM MEM implement (4.6); both SIGN MUX and ALT SUM MEM form a MAC unit with multiplication coefficient of $(-1)^{m'}$. The weighs $\frac{1}{m'}$ in (4.2) are stored in ROM (32 bit wide, N depth: the 4 kB size) and are multiplied with N-S part by 32×32 bit multiplier. The result of the multiplication is rounded to 32 bit wide signal. SIGN MUX 2 stands for $\mathrm{sgn}(S(\ell))$ in (4.2). If a provisional minimal value is found, MIN value is updated; the current $m'(\ell)$ and $N(\ell, m')$ are stored in the register bank. Since the unit core works in five pipeline stages, it has its own Finite State Machine (FSM) controller. The unit runtime for $N = 1\,024$ for arbitrary ℓth spectral line is $\approx 1\,038$ clock cycles.

HW&SW Scheduling

The SW and the HW parts of the system can operate simultaneously using the system DMA unit. This feature can accelerate the algorithm runtime. The runtime for each of algorithm step pertaining to a particular system unit is stated in Tab. 9.1. The runtime of the FFT coprocessor (step 1) is negligible compared with the other ones. Runtime of the N-S coprocessor and the algorithm SW part in the processor (steps 2 and 3) are comparable. Moreover, both algorithm steps are executed N-times for an arbitrary ℓ. Therefore, it is suitable to exploit HW&SW parallelism in steps 2 and 3. The scheduling scheme is to execute the N-S coprocessor to pre-compute l+1th spectral line during the SW part computes lth one. Using this scheduling the total runtime depends virtually on HW N-S coprocessor runtime.

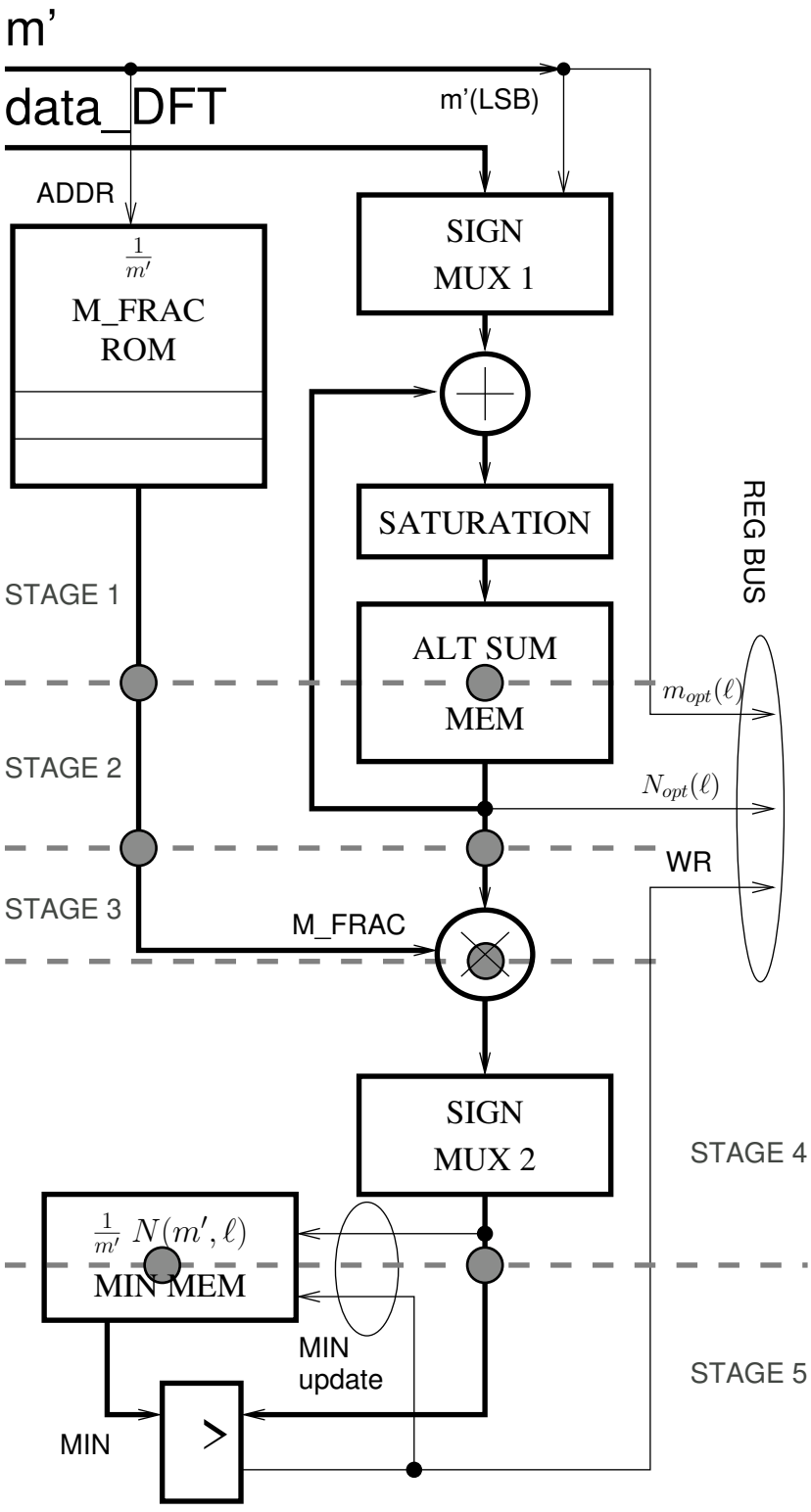

Figure 9.3: Non-stationary coprocessor CORE architecture. MEM clock and global asynchronous reset signals are omitted in the schema. The gray dashed lines denote pipeline stages and the gray dots pipeline registers.

Chapter 10

Appendix B

10.1 Orthogonality of Symmetrical Zolotarev Polynomials

This appendix is a reduced version of prof. Miroslav Vlček's research report which has not been published. The Chebysev polynomial of the first kind is orthogonal [89]

$$2\int_0^1 dx\,\frac{1}{\sqrt{1-x^2}}\,T_{2p}(x)\,T_{2q}(x)=\delta_{pq}\frac{\pi}{2}. \tag{10.1}$$

Let assume substitution

$$x=\sqrt{\frac{w^2-k'^{\,2}}{1-k'^{\,2}}}\quad\text{and}\quad\sqrt{1-x^2}=\sqrt{\frac{1-w^2}{1-k'^{\,2}}}, \tag{10.2}$$

The variable $x\in<0,1>$ provides $w\in<k',1>$, and our orthogonal relation (10.1) reads

$$2\int_{k'}^1\frac{w\,dw}{\sqrt{(1-w^2)\,(w^2-k'^{\,2})}}\,T_p\left(\sqrt{\frac{w^2-k'^{\,2}}{1-k'^{\,2}}}\right)\,T_q\left(\sqrt{\frac{w^2-k'^{\,2}}{1-k'^{\,2}}}\right)=\delta_{pq}\frac{\pi}{2} \tag{10.3}$$

confirming that symmetrical Zolotarev polynomials are orthogonal on disjoint intervals $w\subset<-1,-k'>\cup<k',1>$.

Bibliography

[1] A. V. Oppenheim, R. W. Schafer, and J. R. Buck. *Discrete-Time Signal Processing (2nd Edition) (Prentice-Hall Signal Processing Series)*. Prentice Hall Inc., 1999. ISBN: 0137549202.

[2] W. L. Briggs and V. E. Henson. *The DFT: An Owner's Manual for the Discrete Fourier Transform*. Society for Industrial Mathematics, Jan. 1987. ISBN: 0-89871-342-0.

[3] S. L. Murple. *Digital Spectral Analysis: With Applications*. Prentice Hall Inc., Jan. 1987. ISBN: 9780132141499.

[4] S. C. Pei, M. H. Yeh, and C. C. Tseng. "Discrete fractional Fourier transform based on orthogonal projections". In: *IEEE Transactions on Signal Processing* 47.5 (1999), pp. 1335–1348. DOI: 10.1109/78.757221.

[5] V. Narayanan and K. Prabhu. "The fractional Fourier transform: Theory, implementation and error analysis". In: *Microprocessors and Microsystems* 27 (Nov. 2003), pp. 511–521. DOI: 10.1016/S0141-9331(03)00113-3.

[6] C. Candan, M. A. Kutay, and H. M. Ozaktas. "The discrete fractional Fourier transform". In: *IEEE Transactions on Signal Processing* 48.5 (2000), pp. 1329–1337. DOI: 10.1109/78.839980.

[7] A. Lukin and J. Todd. "Adaptive Time-Frequency Resolution for Analysis and Processing of Audio". In: 4 (Jan. 2012).

[8] D. Rudoy, P. Basu, T. F. Quatieri, et al. "Adaptive short-time analysis-synthesis for speech enhancement". In: *2008 IEEE International Conference on Acoustics, Speech and Signal Processing*. 2008, pp. 4905–4908. DOI: 10.1109/ICASSP.2008.4518757.

[9] V. Katkovnik and L. Stankovic. "Instantaneous frequency estimation using the Wigner distribution with varying and data-driven window length". In: *IEEE Transactions on Signal Processing* 46.9 (1998), pp. 2315–2325. DOI: 10.1109/78.709514.

[10] P. Grünwald. "A Tutorial Introduction to the Minimum Description Length Principle". In: *CoRR* math.ST/0406077 (June 2004).

[11] A. Nazin and V. Katkovnik. "Minimax lower bound for time-varying frequency estimation of harmonic signal". In: *IEEE Transactions on Signal Processing* 46.12 (1998), pp. 3235–3245. DOI: 10.1109/78.735299.

[12] V. Katkovnik and S. L. "Periodogram with varying and data-driven window length". In: *Signal Processing* 67.3 (1998), pp. 345–358. ISSN: 0165-1684. DOI: https://doi.org/10.1016/S0165-1684(98)00049-8. URL: http://www.sciencedirect.com/science/article/pii/S0165168498000498.

[13] L. Debnath. "Recent developments in the Wigner-Ville distribution and time-frequency signal analysis". In: *Proceedings of the Indian National Science Academy. Part A. Physical Sciences* 1 (Jan. 2002). DOI: 10.1007/978-0-8176-8418-1_5.

[14] B. Boashash. *Time Frequency Signal Analysis and Processing, A Comprehensive Reference*. Amsterdam: Elsevier Science, 2003. ISBN: 978-0-0805-4305-5.

[15] P. Chi and C. Russell. "Use of the Wigner-Ville distribution in interpreting and identifying ULF waves in triaxial magnetic records". In: *Journal of Geophysical Research* 113 (Jan. 2008). DOI: 10.1029/2007JA012469.

[16] M. Szmajda, K. Górecki, and J. Mroczka. "Gabor Transform, Gabor-Wigner Transform and SPWVD as a time-frequency analysis of power quality". In: *Proceedings of 14th International Conference on Harmonics and Quality of Power - ICHQP 2010*. 2010, pp. 1–8. DOI: 10.1109/ICHQP.2010.5625371.

[17] A. Papandreou and G. F. Boudreaux-Bertels. "Generalization of the Choi-Williams Distribution and the Butterworth Distribution for Time-Frequency Analysis". In: *IEEE Transactions on Signal Processing* 41.1 (1993), pp. 463–. DOI: 10.1109/TSP.1993.193179.

[18] D. Rudoy, P. Basu, and P. J. Wolfe. "Superposition Frames for Adaptive Time-Frequency Analysis and Fast Reconstruction". In: *IEEE Transactions on Signal Processing* 58.5 (2010), pp. 2581–2596. DOI: 10.1109/TSP.2010.2041604.

[19] R. Merry. *Wavelet theory and applications: a literature study*. DCT rapporten. DCT 2005.053. Technische Universiteit Eindhoven, 2005.

[20] N. Huang, Z. Shen, S. Long, et al. "The empirical mode decomposition and the Hilbert spectrum for nonlinear and non-stationary time series analysis". In: *Proceedings of the Royal Society of London. Series A: Mathematical, Physical and Engineering Sciences* 454 (Mar. 1998), pp. 903–995. DOI: 10.1098/rspa.1998.0193.

[21] N. Huang, Z. Shen, and S. Long. "A new view of non-linear water waves: The Hilbert Spectrum". In: *Annual Review of Fluid Mechanics* 31 (Nov. 2003). DOI: 10.1146/annurev.fluid.31.1.417.

[22] N. E. Huang and Z. Shen. *Hilbert-Huang Transform and Its Applications*. Singapore: Scientific Publishing Co., 2005. ISBN: 981-256-376-8.

[23] N. Huang, M.-L. Wu, S. Long, et al. "A confidence limit for the empirical mode decomposition and Hilbert spectral analysis". In: *Proceedings of The Royal Society A: Mathematical, Physical and Engineering Sciences* 459 (Sept. 2003), pp. 2317–2345. DOI: 10.1098/rspa.2003.1123.

[24] P. Stoica and R. L. Moses. *Introduction to Spectral Analysis*. Prentice Hall, 1997. ISBN: 978-0-132-58419-7.

[25] B. G. Quinn and E. J. Hannan. *The Estimation and Tracking of Frequency*. Cambridge Series in Statistical and Probabilistic Mathematics. Cambridge University Press, 2001. DOI: 10.1017/CBO9780511609602.

[26] S. Haykin. *Nonlinear Methods of Spectral Analysis*. Springer-Verlag, 1979. ISBN: 978-3-540-12386-6.

[27] C. L. Nikias and A. P. Petropulu. *Nonlinear Methods of Spectral Analysis*. Prentice Hall Inc., 1993. ISBN: 978-0-136-78210-0.

[28] M. Vlček and R. Unbehauen. "Zolotarev polynomials and optimal FIR filters". In: *IEEE Transactions on Signal Processing* 47.3 (1999), pp. 717–730. ISSN: 1053-587X. DOI: 10.1109/78.747778.

[29] M. Vlček and P. Zahradník. "Almost Equiripple Low-Pass FIR Filters". English. In: *Circuits, Systems, and Signal Processing* 32.2 (2013), pp. 743–757. ISSN: 0278-081X. DOI: 10.1007/s00034-012-9484-0. URL: http://dx.doi.org/10.1007/s00034-012-9484-0.

[30] P. Zahradník and M. Vlček. "Perfect Decomposition Narrow-Band FIR Filter Banks". In: *Circuits and Systems II: Express Briefs, IEEE Transactions on* 59.11 (2012), pp. 805–809. ISSN: 1549-7747. DOI: 10.1109/TCSII.2012.2218453.

[31] X. Chen and T. Parks. "Analytic design of optimal FIR narrow-band filters using Zolotarev polynomials". In: *Circuits and Systems, IEEE Transactions on* 33.11 (1986), pp. 1065–1071. ISSN: 0098-4094. DOI: 10.1109/TCS.1986.1085868.

[32] K. N. Mohan, D. Kannadassan, and S. R. Zinka. "Design and Implementation of Dolph Chebyshev and Zolotarev Circular Antenna Array". In: *Indian Journal of Science and Technology* 9.36 (2016). ISSN: 0974 -5645. URL: http://www.indjst.org/index.php/indjst/article/view/102137.

[33] R. Levy. "Generalized Rational Function Approximation in Finite Intervals Using Zolotarev Functions". In: *Microwave Theory and Techniques, IEEE Transactions on* 18.12 (1970), pp. 1052–1064. ISSN: 0018-9480. DOI: 10.1109/TMTT.1970.1127411.

[34] P. Zahradník and M. Vlček. "Fast analytical design algorithms for FIR notch filters". In: *Circuits and Systems I: Regular Papers, IEEE Transactions on* 51.3 (2004), pp. 608–623. ISSN: 1549-8328. DOI: 10.1109/TCSI.2003.822404.

[35] R. Špetík. "The Discrete Zolotarev Transform". PhD thesis. Czech Technical University in Prague, Faculty of Electrical Engineering, Feb. 2009.

[36] V. Turoň. "Description of spectral analysis based on Zolotarev polynomials (in Czech)". PhD thesis. Czech Technical University in Prague, Faculty of Electrical Engineering, Aug. 2016.

[37] V. Turoň, J. Janík, Špetík R., et al. "Study of ADZT properties for spectral analysis". In: *In Proceedings of the 11th WSEAS international conference on Signal processing, computational geometry and artificial vision, and Proceedings of the 11th WSEAS international conference on Systems theory and scientific computation (GAVTASC'11)*. Vol. World Scientific and Engineering Academy and Society (WSEAS), Stevens Point, Wisconsin, USA. 2011, pp. 171–176.

[38] V. Turoň. "A study of parameters setting of the STADZT". In: *Acta Polytechnica*. Vol. 52. 5. 2012, pp. 106–111.

[39] V. Turoň, J. Janík, R. Špetík, et al. "Porovnání dvou spektrálních metod pro analýzu akustických signálů". In: *Akustické listy*. Vol. 4. Česká akustická společnost, 2011, pp. 26–30.

[40] *Novel Selective Transforms For Non-Stationary Signal Processing*. [online]. URL: http://amber.feld.cvut.cz/selectivetransforms.

[41] M. Vlček, J. Janík, V. Turoň, et al. "A way to a new multi-spectral transform". In: *In Proceedings of the 11th WSEAS international conference on Signal processing, computational geometry and artificial vision, and Proceedings of the 11th WSEAS international conference on Systems theory and scientific computation (GAVTASC'11)*. Vol. World Scientific and Engineering Academy and Society (WSEAS), Stevens Point, Wisconsin, USA. 2011, pp. 177–182.

[42] B. H. L. Sen M. Kuo. *Real-Time Digital Signal Processing*. John Wiley & Sons, Ltd., 2001.

[43] *Spartan-6 Family Overview*. Xilinx. Oct. 2011. URL: http://www.xilinx.com/support/documentation/data_sheets/ds160.pdf.

[44] *AtlysTM Board Reference Manual*. Digilent. Aug. 2013. URL: https://www.xilinx.com/support/documentation/university/XUP%20Boards/XUPAtlys/documentation/Atlys_rm.pdf.

[45] *Spartan-6 FPGA DSP48A1 Slice*. Xilinx. May 2014. URL: www.xilinx.com/support/documentation/user_guides/ug389.pdf.

[46] J. Bergeron. *Writing Testbenches: Functional Verification of HDL Models, Second Edition*. Norwell, MA, USA: Kluwer Academic Publishers, 2003. ISBN: 1402074018.

[47] *Digilent Parallel Interface Model Reference Manual*. Digilent. Oct. 2004. URL: https://reference.digilentinc.com/_media/reference/software/adept/adept-2/dpimref_programmers_manual.pdf.

[48] S. Rhoads. *Plasma - most MIPS I(TM)*. www.OpenCores.org. Nov. 2016. URL: http://opencores.org/project,plasma,overview.

[49] K. A. Loparo, M. L. Adams, W. Lin, et al. "Fault detection and diagnosis of rotating machinery". In: *IEEE Transactions on Industrial Electronics* 47.5 (2000), pp. 1005–1014. DOI: 10.1109/41.873208.

[50] L. Lovisolo, M. Tcheou, M. Rodrigues, et al. "Modeling of Electric Disturbance Signals Using Damped Sinusoids via Atomic Decompositions and Its Applications". In: *EURASIP Journal on Advances in Signal Processing* (Mar. 2007). DOI: 10.1155/2007/29507.

[51] S. Lotfifard, J. Faiz, and M. Kezunovic. "Detection of Symmetrical Faults by Distance Relays During Power Swings". In: *IEEE Transactions on Power Delivery* 25.1 (2010), pp. 81–87. DOI: 10.1109/TPWRD.2009.2035224.

[52] H. Qarib and H. Adeli. "A new adaptive algorithm for automated feature extraction in exponentially damped signals for health monitoring of smart structures". In: *Smart Materials and Structures* 24.12 (Nov. 2015), p. 125040. DOI: 10.1088/0964-1726/24/12/125040. URL: https://doi.org/10.1088/0964-1726/24/12/125040.

[53] L. Su, S.-Q. Mei, Y.-H. Pan, et al. "Experimental identification of exponential damping for reinforced concrete cantilever beams". In: *Engineering Structures* 186 (2019), pp. 161–169. ISSN: 0141-0296. DOI: https://doi.org/10.1016/j.engstruct.2019.02.015. URL: https://www.sciencedirect.com/science/article/pii/S0141029618322880.

[54] B. Bajpeyee and S. Sharma. "Detection of bearing faults in induction motors using short time approximate discrete Zolotarev transform". In: *International Conference on Signal Processing (ICSP 2016)*. Nov. 2016, pp. 1–7. DOI: 10.1049/cp.2016.1467.

[55] P. Masa, P. Sovka, M. Vlcek, et al. "Using ADZT for a signal reconstruction". In: *2013 European Conference on Circuit Theory and Design (ECCTD)*. 2013, pp. 1–4. DOI: 10.1109/ECCTD.2013.6662335.

[56] S. M. Kay and S. L. Marple. "Spectrum analysis – A modern perspective". In: *Proceedings of the IEEE* 69.11 (1981), pp. 1380–1419. DOI: 10.1109/PROC.1981.12184.

[57] K. Steiglitz and L. McBride. "A technique for the identification of linear systems". In: *IEEE Transactions on Automatic Control* 10.4 (1965), pp. 461–464. DOI: 10.1109/TAC.1965.1098181.

[58] L. Rabiner and B. Juang. *Fundamentals of Speech Recognition*. Prentice-Hall, 1993. ISBN: 0-13-015157-2.

[59] R. Schmidt. "Multiple emitter location and signal parameter estimation". In: *IEEE Transactions on Antennas and Propagation* 34.3 (1986), pp. 276–280. DOI: 10.1109/TAP.1986.1143830.

[60] L. Rabiner and B. Gold. "Theory and Application of Digital Signal Processing". In: *Prentice Hall Inc.* (1975). DOI: https://doi.org/10.1002/piuz.19760070413. URL: https://onlinelibrary.wiley.com/doi/abs/10.1002/piuz.19760070413.

[61] K. Prabhu. *Window Functions and Their Applications in Signal Processing*. CRC Press, Oct. 2013. ISBN: 9781466515833. DOI: 10.1201/9781315216386.

[62] R. B. Randall and J. Antoni. "Rolling element bearing diagnostics—A tutorial". In: *Mechanical Systems and Signal Processing* 25.2 (2011), pp. 485–520. ISSN: 0888-3270. DOI: https://doi.org/10.1016/j.ymssp.2010.07.017. URL: https://www.sciencedirect.com/science/article/pii/S0888327010002530.

[63] N. Sawalhi. "Rolling element bearings localized fault diagnosis using signal differencing and median filtration". In: *Journal of Vibroengineering* 20 (May 2018). DOI: 10.21595/jve.2017.18254.

[64] J. C. Mason. *Chebyshev polynomials*. Boca Raton, Fla: Chapman & Hall/CRC, 2003. ISBN: 978-0849303555.

[65] M. Vlček, P. Sovka, and R. Špetík. "Algebraic Solutions for Iso-extremal Polynomials on Two Disjoint Intervals". In: *9th IMA International Conference on Mathematics in Signal Processing*. The Institute of Mathematics and its Applications. 16 Nelson Street, Southend on Sea, Essex SS1 1EF: Catherine Richards House, Dec. 2012.

[66] A. V. Oppenheim, A. S. Willsky, and with S. Hamid. *Signals and Systems (2nd Edition)*. Prentice Hall Inc., 1996. ISBN: 0138147574.

[67] G. J. Cooper. "The evaluation of the coefficients in the Chebyshev expansion". In: *The Computer Journal* 10.1 (1967), pp. 94–100. DOI: 10.1093/comjnl/10.1.94. eprint: http://comjnl.oxfordjournals.org/content/10/1/94.full.pdf+html. URL: http://comjnl.oxfordjournals.org/content/10/1/94.abstract.

[68] V. P. Sklyarov. "A numerical experiment related to Zolotarev polynomials for weighted sup-norm". In: *Computational Mathematics and Mathematical Physics* 51.10 (2011), p. 1679. ISSN: 1555-6662. DOI: 10.1134/S0965542511100149. URL: http://dx.doi.org/10.1134/S0965542511100149.

[69] B. Bogytarov A. "Effective approach to least deviation problems". In: *Mat. Sb.* 193.12 (2002), pp. 1749–1769.

[70] S. Sukittanon, E. Atlas, W. Pitton, et al. "Numerical Computation of the Markov Factors for the systems of Polynomials with the Hermite and Laguerre Weights". In: *6th Conf. on Numerical Metjhods and Applications NMA 2006, Bulgaria*. Vol. Springer-Verlag Berlin. August 20-24, pp. 386–393.

[71] G. Grasegger and N. T. Vo. *An Algebraic-Geometric Method for Computing Zolotarev Polynomials*. Submitted. 2016.

[72] V. Lampret. "Estimating the sequence of real binomial coefficients." eng. In: *JIPAM. Journal of Inequalities in Pure & Applied Mathematics [electronic only]* 7.5 (2006), Paper No. 166, 16 p., electronic only–Paper No. 166, 16 p., electronic only. URL: http://eudml.org/doc/128373.

[73] H. H. Panjer and n. Shaun Wang. "On the Stability of Recursive Formulas". In: *ASTIN Bulletin* 23 (02 Nov. 1993), pp. 227–258. ISSN: 1783-1350. DOI: 10.2143/AST.23.2.2005093.

[74] J. J. DaCunha. "Stability for time varying linear dynamic systems on time scales". In: *Journal of Computational and Applied Mathematics* 176.2 (2005), pp. 381 –410. ISSN: 0377-0427. DOI: http://dx.doi.org/10.1016/j.cam.2004.07.026. URL: http://www.sciencedirect.com/science/article/pii/S0377042704003449.

[75] C. Loader. *Fast and accurate computation of binomial probabilities*. 2000. URL: http://savannah.gnu.org/bugs/download.php?file_id=24016.

[76] J. Janík, P. Sovka, and M. Vlček. "How we came up with ADZCT". In: *International Conference on Applied Electronics (AE), Pilsen*. 2012, pp. 119–122.

[77] C. D. Meyer. *Matrix analysis and applied linear algebra*. New York, United States: Society for Industrial & Applied Mathematics, U.S., May 2010. ISBN: 978-0898714548.

[78] T. Cupaiuolo and D. Lo Iacono. "A flexible and fast software implementation of the FFT on the BPE platform". In: *Design, Automation Test in Europe Conference Exhibition (DATE), 2012*. Mar. 2012, pp. 1467–1470. DOI: 10.1109/DATE.2012.6176598.

[79] K. Shetti, C. Koh, M. Aung, et al. "Development and code partitioning in a software configurable processor". In: *TENCON 2009 - 2009 IEEE Region 10 Conference*. Jan. 2009, pp. 1–5. DOI: 10.1109/TENCON.2009.5396149.

[80] B. Baas. "A low-power, high-performance, 1024-point FFT processor". In: *Solid-State Circuits, IEEE Journal of*. Vol. 34. 3. Mar. 1999, pp. 380–387. DOI: 10.1109/4.748190.

[81] C. Cheng and K. Parhi. "High-Throughput VLSI Architecture for FFT Computation". In: *Circuits and Systems II: Express Briefs, IEEE Transactions on*. Vol. 54. 10. Oct. 2007, pp. 863–867. DOI: 10.1109/TCSII.2007.901635.

[82] S. He and M. Torkelson. "Design and implementation of a 1024-point pipeline FFT processor". In: *Custom Integrated Circuits Conference, 1998. Proceedings of the IEEE 1998*. Mar. 1998, pp. 131–134. DOI: 10.1109/CICC.1998.694922.

[83] J. Teich. "Hardware/Software Codesign: The Past, the Present, and Predicting the Future". In: *Proceedings of the IEEE*. Vol. 100. Special Centennial Issue. May 2012, pp. 1411–1430. DOI: 10.1109/JPROC.2011.2182009.

[84] T.-H. Tsai, Y.-C. Yang, and C.-N. Liu. "A Hardware/Software Co-Design of MP3 Audio Decoder". English. In: *Journal of VLSI signal processing systems for signal, image and video technology*. Vol. 41. 1. Kluwer Academic Publishers, 2005, pp. 111–127. DOI: 10.1007/s11265-005-6254-2.

[85] W. M. Gentleman and G. Sande. "Fast Fourier Transforms: For Fun and Profit". In: *Proceedings of the November 7-10, 1966, Fall Joint Computer Conference*. AFIPS '66 (Fall). San Francisco, California: ACM, 1966, pp. 563–578. DOI: 10.1145/1464291.1464352.

[86] *MIPS32 Architecture For Programmers Volume II: The MIPS32 Instruction Set*. MIPS TECHNOLOGIES. Mar. 2001. URL: http://www.mips.com/.

[87] Y.-N. Chang and K. Parhi. "High-performance digit-serial complex-number multiplier-accumulator". In: *Computer Design: VLSI in Computers and Processors, 1998. ICCD '98. Proceedings. International Conference on*. Oct. 1998, pp. 211–213. DOI: 10.1109/ICCD.1998.727050.

[88] J. Palascak. "FFT core implementation (in Czech)". MA thesis. FEL CTU in Prague, 2010.

[89] M. Vlček. *Classical Orthogonal Polynomials*. Výzkumná zpráva. 2011.

List of Author's Publications

- The author has the H-index of two at the time of the thesis completion, according to Web of Science.

Related to the Dissertation Thesis

Journals with Impact Factor

[A1] KUBÁK, J., P. SOVKA and M. VLČEK. *Evaluation of Computing Symmetrical Zolotarev Polynomials of the First Kind*. Radioengineering. 2017, 26(3), 903-913. ISSN 1210-2512. DOI 10.13164/re.2017.0903.

[A2] KUBÁK, J., J. ŠŤASTNÝ and P. SOVKA. *An Embedded Implementation of Discrete Zolotarev Transform Using Hardware-Software Codesign*. Radioengineering. Revision status: CONDITIONALLY ACCEPTED. Should be issued in 2021.

- The publication [A1] was cited twice at the time of this thesis completion. First time in an article in journal with impact factor and second time in a dissertation thesis, according to Web of Science.

Reviewed Journals

[A3] KUBÁK, J. *Damped harmonic signals analysis using ADZT. Elektrorevue*. 2021, ISSN 1213-1539. Available at: http://www.elektrorevue.cz/cz/clanky/zpracovani-signalu/0/damped-harmonic-signals-analysis-using-adzt/

Other

[A4] KUBÁK, J. "Realizace výpočtu ZT využívající zjednodušených Zolotarevových polynomů na FPGA." In: *ČMEJLA, R. Č., J. R. RUSZ a J. S. SEDLÁK, eds. IV. Letní doktorandské dny 2014. Letní doktorandské dny 2014*, Praha, 2014-05-29/2014-05-30. Praha: ČVUT FEL, Katedra teorie obvodů, 2014. s. 5-8. ISBN 978-80-01-05506-9.

[A5] KUBÁK, J. and P. SOVKA. *Studie chování aproximované diskrétní Zolotarevovy transformace pro analýzu tlumených harmonických signálů*. [Research report] 2020.

[A6] KUBÁK, J. *Novel time selective transform utilizing symmetrical Zolotarev polynomials*. [Research report] 2020.

Not Related to the Dissertation Thesis

[A7] J. Millar, A. Ahmadi, J. Kubak. "Radar Track Initialization." U.S. Patent 20200124716, issued April 23, 2020. [Online]. Available at: `https://patents.justia.com/patent/20200124716`

[A8] M. Mandlik, C. Sturm, U. Lübbert, T. Vajdiak and J. Kubak, "Multiband automotive radar sensor with agile bandwidth," 2017 IEEE-APS Topical Conference on Antennas and Propagation in Wireless Communications (APWC), Verona, 2017, pp. 163-165, doi: 10.1109/APWC.2017.8062269. Available at: `https://ieeexplore.ieee.org/document/8062269`

[A9] KUBÁK, J., J. ŠŤASTNÝ and P. KUJAN. "Programmable PWM modulator optimized for high speed for OPWM test platform." In: *19th International Conference on Applied Electronics 2014*. Pilsen, 2014-10-09/2014-10-10. Pilsen: University of West Bohemia, 2015. s. 157-160. ISSN 1803-7232. ISBN 978-80-261-0276-2. Available at: `https://ieeexplore.ieee.org/document/7011690`

[A10] KUBÁK, J. "Řízení testovací platformy optimální pulzně šířkové modulace". In: *23rd Annual Conference Proceedings of Technical Computing Prague 2015*. Technical Computing Prague 2015, Praha, 2015-11-04. Praha: VŠCHT Praha, 2015. ISSN 2336-1662. ISBN 978-80-7080-936-5. Available at: `https://www2.humusoft.cz/www/papers/tcp2015/036_kubak.pdf`

- The publication [A8] was cited four times at the time of this thesis completion, according to Web of Science.